Dipartimento di Fisica G. Occhialini

Dottorato di ricerca in Fisica e Astronomia
Ciclo XXX
Curriculum: Fisica della materia condensata,
Fisica dei plasmi e biofisica

MICROFLUIDIC FLOW MAPPING WITH SPIM-ICS

Nicolò Giovanni Ceffa
702101

Tutor: Prof. Giuseppe Chirico

Coordinatore: Prof. Marta Calvi
Anno accademico: 2016/2017

Contents

Chapter 1

Abstract

Everything should be as simple as it can be but not simpler.

Albert Einstein

Systems complexity may be partitioned, but it's a conserved quantity: sometimes it arises because of a poor understanding of a subject, and then, luckily, thanks to a theoretical breakthrough or a bright original idea, it can be reduced, and this is an advancing step towards a true understanding. But supposing that we decide to employ a robust and trustworthy theoretical backbone, which we *trust* completely, then we face the study of a physical system working on measurement devices and on a clever experimental design, together with a smart data analysis procedure, in order to unveil the charac-

teristics that we care about. A choice of the right apparatus, investing great effort in its precise development or in advanced data analysis techniques, can move complexity from the system itself to other parts of the experimental procedure: it's like devoting time and effort to understand the right mathematical framework when working out a problem or, in general, taking care of practising with the right tool for the job, even if it seems very difficult to handle at first. It all pays off.

This apparently vague approach is actually extremely important, remembering that we face the ubiquitous presence of what I would define as a *boundary trade-off*: a line which defines the boundaries of our world resolution. The most famous example resides in the fundamental laws of quantum mechanics, e.g. $\Delta x \Delta p \geq \frac{\hbar}{2}$, which states that it's possible to push further on position resolution only giving up some knowledge about momentum.

This idea is readily translated into the study of microscopic biological samples, in particular the ones that I've been studying: it's not a unbreakable, fundamental law, but should be better approached as a challenge, a barrier to be broken. The situation is very easy to understand: if we want to study phenomena that occur at cellular level (or beyond), without killing or damaging a biological sample, then light microscopy is the way to go, and the most useful, readily understandable thing

that we can extract from a biological object is an image. Obtaining high resolution images requires effort, high precision instrumentation and, as anyone would expect, time: the better the image, the slower the acquisition process. Fighting against this trade-off is a constant challenge, especially in the field of light microscopy, and in the last years extremely clever ideas and concepts have been demonstrated in order to achieve very high resolution, but often at the expense of time acquisition or sample heavy manipulation.[1] The solution I followed in my work is to employ Light Sheet Fluorescence Microscopy (LSFM)[2] technique (also known as Selective-Plane Illumination Microscopy, SPIM) and a fast-acquisition, high efficiency camera, in order to achieve the minimum spatio-temporal resolution required (microns in space, 4ms in time). Acting on illumination profile, it is in fact possible to engineer a sheet of light to select just a thin (μm size) slice of the sample, so that fluorescence signals coming from just that plane can be measured in a 90° collection geometry: I just moved a little bit of complexity on the excitation/collection apparatus. The CCD camera employed is in fact an EMCCD (see Chapter 2.3) fabricated with a very advanced technology, capable of extremely high efficiency detection (quantum efficiency up to 95%), thus allowing very fast acquisition speeds. The last step was to fabricate samples and sample holder specifically

designed to work with SPIM geometry, to achieve high transparency. Much work has been devoted to the study and manipulation of cross-correlation based algorithms, employed to retrieve flow parameters: this technique, as explained in Chapter 2, is extremely powerful. At this step it's sufficient to say that it is based on *noise* analysis, thus capable of excellent performances even in the most intricate biological situation I tried to investigate. My goal was to perform space and time mapping of blood flow in biological samples (Zebrafish embryos), being able to collect wide images (hundreds of microns), but still resolving them at a μm level; moreover hemodynamics is a fast process, that requires very high frequency sampling (tens to hundreds of Hz) in order to be resolved. The general biological motivation is that the progression of a wide number of diseases is affected directly by the blood circulation (an important example is cancer and its metastases[3]), so that I want to devise an test methods to quantitatively map blood flow in different conditions, both for diagnosis and study of pathologies evolution (e.g. the inflammatory response results in a strengthened immune presence in certain regions, also revealed by increased blood flow).

The description of theoretical and practical aspects of my setup is the core of Chapter 2: at first, I will describe Single

Plane Illumination Microscopy, focusing on a Physical Optics description of illumination and detection profiles. Then I will describe the practical implementation of two microscopes, one for in-vitro and one for in-vivo testing, showing an experimental evaluation of useful parameter derived in the previous section. The second part of the chapter is dedicated to the analysis of Cross-Correlation methods, providing both a solid presentation of all the techniques employed for image analysis, and also serving as an introduction for chapter 6, where an extension of these methods will be presented.

Finally I will cover basic fluid dynamics to introduce a simple *lumped circuit* model (useful, at first approximation, to describe microfluidics networks) deriving the fundamental equation (Poiseuille flow in square channels) employed to describe in-vitro flows.

Chapter 3 will describe material and methods, in particular it will deal with PDMS (Polydimethylsiloxane) based microstructures, liposomes fabrication, and Zebrafish embryos description. It is intended as a comprehensive overview of every system or sample employed, each one described form a perspective that tries to highlight the characteristics that are most important for my studies.

In Chapter 4 I will summarize the results of the study of both in-vitro and in-vivo time-varying flows. here I show a a first

powerful application of temporal cross-correlation techniques coupled with large field of view images, which allows high resolution (both in time and space) mapping of flows.
In Chapter 5 I will present related investigations, based on Image spatio-temporal correlations, in which I focused on in-vivo hemodynamics, in particular mapping blood flow in branched vessels in zebrafish embryos.
Chapter 6 focuses on the most recent part of my work, that is to explore a way to break the "plane restriction" that seems to be intrinsically present when employing SPIM based microscopy. I will show that correlative methods can be extended allowing to retrieve 3D flow information, without any change in the hardware, as happens, for example, in optical tomography or micro-PIV. These studies are te subject of an article, under revision.

Finally Chapter 7 is dedicated to conclusions and future outlook.

Chapter 2

Theorethical background

It doesn't matter how beautiful your theory is, it doesn't matter how smart you are. If it doesn't agree with experiment, it's wrong.

Feynman

Under the name **I**mage **C**orrelation **S**pectroscopy[4] resides a number of techniques that have in common the fact of taking a raw video of the data (3D matrix of data entries) as input to extract quantitative informations about sample dynamics, exploiting the properties of correlation functions. The accessible

informations are closely related to the spatial and temporal resolutions of the acquisition system. In this thesis I am interested in spatiotemporal scales of the order of *hundreds of ms* and of *tens of microns*, respectively. I chose to employ a fast recording EMCCD camera (Cascade II, Photometrics) together with a **S**elective **P**lane **I**llumination **M**icroscopy setup (SPIM from now on), that perfectly matched my needs, being capable of providing, in the best configuration, a resolution of $\{4\ ms$ and $1\ \frac{\mu m}{pixel}\}$. SPIM (also referred to Light Sheet Fluorescence Microscopy, LSFM, when coupled with fluorescence detection) will be described extensively in this chapter. Here I will just mention two features that made it the best choice for flow mapping studies. It allows the recording of large field of view (FOV) images (limited only by objective choice and camera chip) without any temporal delay (there is no scanning or sample movement involved). Moreover it possesses intrinsic optical sectioning, allowing to select a thin slice of sample (few μm thick, depending on the actual apparatus employed, see following discussion for details), reducing out-of-focus artefacts and photodamage. In this way the recorded data contain, as it is easy to see, a huge amount of information, and are perfect to be analysed with correlative methods, that are capable of highlight transport phenomena even at large time and spatial scales (theoretically every single pixel of the

FOV can be useful), at the highest resolutions available.
In this chapter I'll start presenting a detailed theoretical description of LSFM, focusing on the analysis of excitation and detection profiles, to understand, within the framework of Physical Optics, the behaviour of optical fields at relevant planes inside the apparatus; then I will briefly describe the practical implementation of two setups, one specifically designed for in-vitro measurements, the other for in-vivo experiments, built around a custom made immersion chamber.[5] I will then present an overview of fluorescence based cross-correlation methods,[6] focusing on the two versions employed here (temporal and spatio-temporal image correlations); finally, I will describe microfluidic models that I have adopted to represent both in-vivo and in-vitro microfluidic systems.

2.1 SPIM

Selective **P**lane **I**llumination **M**icroscopy can be thought as an alternative to confocal microscopy,[7] since it is capable of obtaining optical sectioning over all the available field of view, without any mechanical movement or laser scanning process. Besides, it helps reducing photodamage,[8] since the in-focus plane is the only one actually illuminated by excitation light:

this is particularly helpful when dealing with live samples, when phototoxicity may be an issue. I aim here to draw a very intuitive scheme of the implementation of the SPIM apparatus (the first is an almost exact 3D reconstruction of the employed setup, while the second shows the optical path in a more rigorous way), that will serve as a reference during my theoretical analysis:

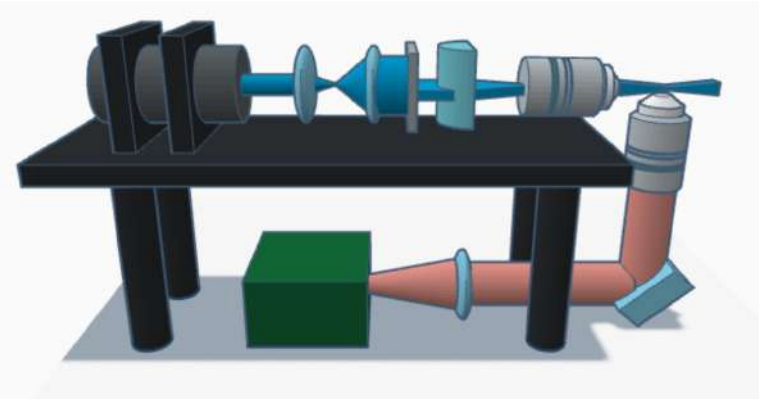

Figure 2.1: 3D scheme of SPIM setup.

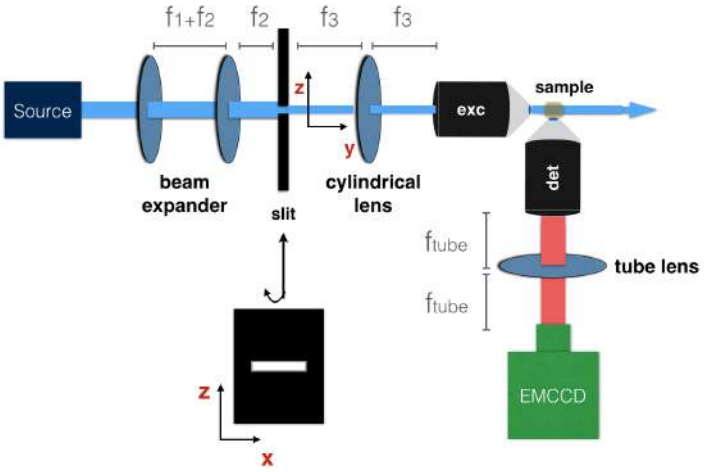

Figure 2.2: 2D schematic of the setup.

A laser source excitation profile is magnified to uniformly illuminate a rectangular slit: then a cylindrical lens coupled with the excitation objective generates a sheet-like profile, optically sectioning the sample. The detection configuration is a classical objective - tube lens couple (i.e. as in wide field microscopy), in a 90° geometry with respect to excitation: it creates a magnified image of the illuminated sample slice on a pixelated detector.

2.2 Physical Optics description

The real core of SPIM resides in the excitation geometry, so let's start from the following schematic representing 2D projections of the excitation optical path:

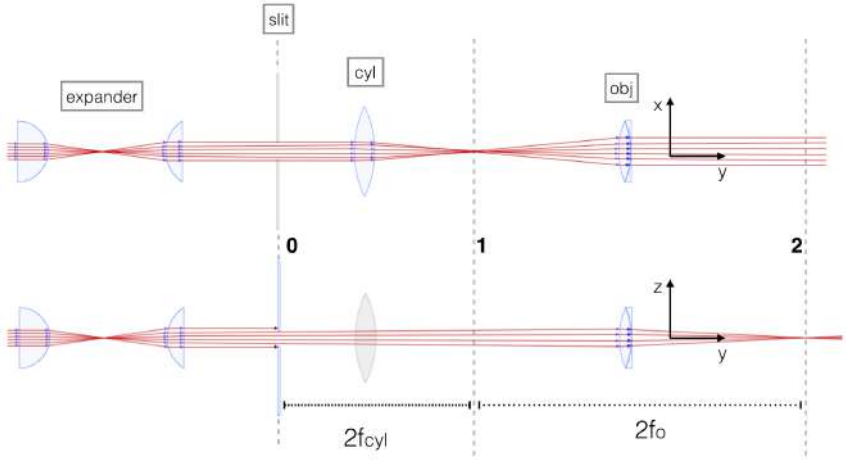

Figure 2.3: Ray-tracing the excitation path. Top: (x,y) section. Bottom: (z,y) section. Optical path: $\hat{y}$

During all the following description I will maintain the same frame of reference: excitation beam propagation is in the $\hat{y}$ direction, and consequently the planes that I will de-

scribe are $\hat{x}, \hat{z}$ planes. This choice allows the usual notation in detection, where (being all rotated 90°) $\hat{z}$ will be the optical path axis, with the usual $\hat{x}, \hat{y}$ transverse planes.

Excitation laser profile is expanded by two lenses in a telescopic configuration (tag "expander"), in order to match the cylindrical lens pupil: to understand the light field distribution behaviour, this beam expander can be neglected, since geometrical optics is perfectly enough to describe it's role.
The core part consists in a rectangular *slit*, followed by a *cyl*indrical lens: the slit is just a rectangular binary stop that I will model with the function

$$rect\left(\frac{z}{a}\right) rect\left(\frac{x}{b}\right) = \begin{cases} 1 \; if \; |z| \leq \frac{a}{2} \; and \; |x| \leq \frac{b}{2} \\ 0 \text{ otherwise} \end{cases} \tag{2.1}$$

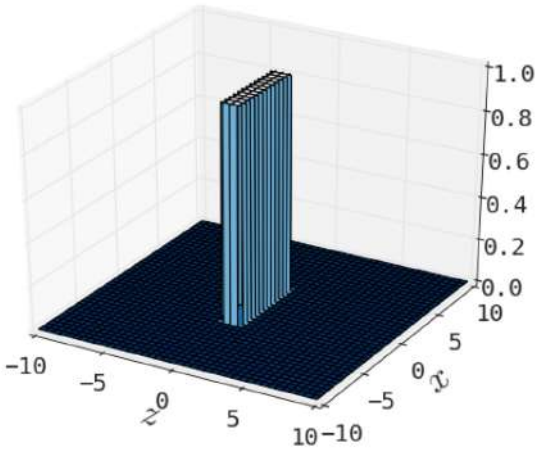

Figure 2.4: *rect* function example

This equation is separable in the {z, x} coordinates, and this is a great advantage since the cylindrical lens behaves in a fundamentally different way along $\hat{z}$ or $\hat{x}$ directions: it acts as a classical lens along the $\hat{x}$ direction, with f_{cyl} focal length ($50mm$ in this case) while it leaves unaffected the beam on the $\hat{z}$ direction. This is apparent looking at figure 2.3: the top row represents the $\{\hat{x}, \hat{y}\}$ projection, where the lager dimension of the slit is not acting as an actual stop, and where the cylindrical lens is focusing the beam in the back aperture of the

excitation objective (slit plane **0** is conjugated with plane **1**); the bottom shows the $\{\hat{z}, \hat{y}\}$ projection, where the slit is the limiting device and the cylindrical lens is not doing any actual work, leaving the unaltered slit profile reach the objective lens back aperture.

To evaluate the complete excitation beam profile I will describe separately the $\hat{z}$ and $\hat{x}$ directions, propagating the field distributions towards the objective focus. Then following McCutchen[9] and, more closely, Mertz,[7] I will investigate the complete 3D excitation profile, applying a frequency domain defocus.

2.2.1 $\hat{z}$ profile

Figure 2.5 serves as schematic representation to show the propagation geometry adopted to describe the field along the z direction:

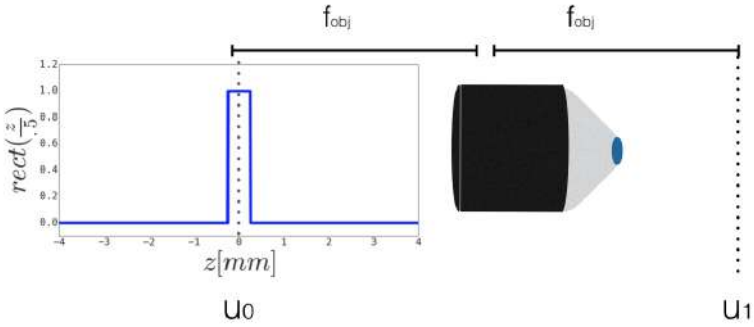

Figure 2.5: Profile schematics along the $\hat{z}$ direction.

As said before, the cylindrical lens can be neglected, and since the propagating beam remains collimated, we are left with an effective 2-f system. Employing the notation explained in the Appendix, it's readily found that the profile at the objective focal plane is:

$$u_1(z) = \frac{a\, e^{2i\lambda f_o}}{(i\lambda f_o)^{\frac{3}{2}}}\, U_0\left(a\,\xi\right)|_{\xi=\frac{z}{\lambda f_o}} \tag{2.2}$$

Where U_0 is the Fourier Transform of the incoming field distribution u_0 at the objective front focal plane:

$$U_0(z) = a\, sinc\left(\frac{a}{\lambda f_o} z\right) \tag{2.3}$$

Since fluorescence is an incoherent phenomenon in which only the intensity of the field plays an actual role, I will use the following normalized model, neglecting the first phase terms:

$$|u_1(z)|^2 \propto \left| U_0 \left(\frac{a\, z}{\lambda f_o} \right) \right|^2 = sinc^2 \left(\frac{a}{\lambda f_0} z \right) \tag{2.4}$$

This equation shows with great clarity that the slit variable width (a) is the key parameter that controls the thickness of the excitation light sheet (excluding of course the change in any optical component like laser source or objective lens). To get an handle of things, let's plug in eq. 2.4 typical values: for $a \simeq 1.2\,mm$, $\lambda = 488\,nm$ and $f_o = 8\,mm$ then the *sinc* function has a shape:

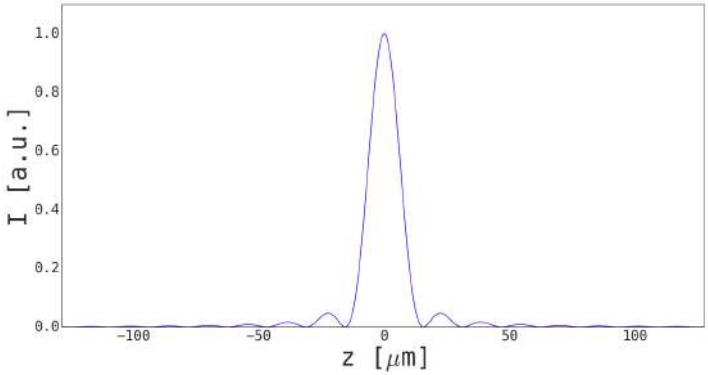

Figure 2.6: In-focus ideal excitation profile

with the first zero happening at $z \simeq 10\mu m$ (see section 2.3 for an experimental measurements). Experimentally all the precautions have been taken to obtain optically transparent samples and microfluidic channels (see Chapter 4) so that the excitation profile is minimally perturbed traversing the sample. A possible improvement could be employing an adaptive optics system to correct for artefacts, reaching higher axial resolution[10] or to use double counter-propagating excitation beams.

2.2.2 $\hat{x}$ profile

Again, let's look at an illustrative schematic:

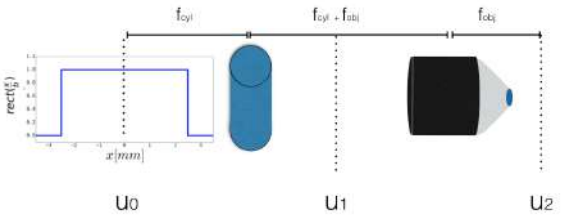

Figure 2.7: $\hat{x}$ excitation

In this case the cylindrical lens, conjugated with the objective back aperture, bends the incoming beam to accomplish

uniform illumination over the detection field of view.
Let's look closely to the optical fields at the highlighted planes u_i:

$$\begin{cases} u_0(x) = rect\left(\frac{x}{b}\right) \\ u_1(x) = \frac{b\, e^{2kif_{cyl}}}{(\lambda f_{cyl})^{\frac{3}{2}}}\, U_0(b\,\xi)|_{\xi=\frac{x}{\lambda f_{cyl}}} \\ u_2(x) = \frac{e^{2ikf_o}}{(\lambda f_o)^{\frac{3}{2}}}\, U_1(\xi)|_{\xi=\frac{x}{\lambda f_o}} \end{cases} \tag{2.5}$$

As done in the previous section, carrying out calculations and finally simplifying with a normalized model, neglecting the first phase terms:

$$u_2(x) = \frac{e^{2ik(f_{cyl}+f_o)}}{\lambda^4 f_o^{\frac{3}{2}} f_{cyl}^{\frac{1}{2}}}\, rect\left(\frac{f_{cyl}}{bf_o}x\right) \tag{2.6}$$

$$|u_2(x)|^2 \propto rect^2\left(\frac{f_{cyl}}{bf_o}x\right) \tag{2.7}$$

The last formula clearly shows how the choice of cylindrical lens and objective focal lengths, together with the slit larger dimension, limits the excitation beam extension in the $\{\hat{x}, \hat{y}\}$ plane (i.e. the SPIM plane). Inserting the values that describe the SPIM arrangement employed for in-vitro measurements ($f_{cyl} = 50\,mm$, $b \simeq 8\,mm$, and $f_0 = 8\,mm$) eq. 2.7 gives a *rect* function with total width of $1.28\,mm$: this doubles

the maximum FOV available ($\sim 500 \times 500 \mu m$), fulfilling the request of uniform illumination in the focal plane.

2.2.3 3-D extended excitation

Once obtained the in-focus excitation profiles, it is possible to introduce a small defocus to investigate the field distribution along the optical axis.[7,11] This defocus is nothing more than a free-space Fresnel propagator (see Appendix for details), and it is best carried out in the spatial-frequency domain. Starting from the excitation profile just obtained ($u(x,z)$) the fist step consists in evaluating its frequency spectrum:

$$U_i(\xi,\zeta) = FT\{u(x,z)\} \tag{2.8}$$

In this way, convolution with the free space Fresnel propagator becomes a multiplication:

$$U(\xi,\zeta;y) = U(\xi,\zeta)\, e^{iky}\, q^*(\xi,\zeta;\lambda y) \tag{2.9}$$

And the distribution around the objective focal point can then be expressed with a 2D inverse transform:

$$u(x,y;z) = IFT\{U(\xi,\zeta;y)\}(x,z;y) \tag{2.10}$$

I wrote a Python code to simulate the extended excitation profile. Here I present the most important result (based on the

parameter employed in the previous paragraphs) that I think are helpful to visualize the formulas.

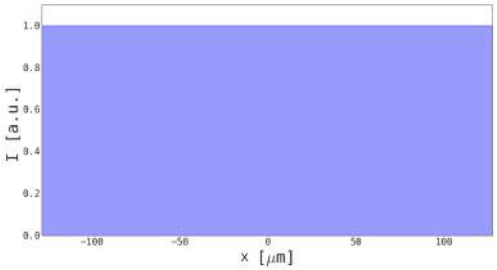

Figure 2.8: $\hat{x}$ in focus excitation

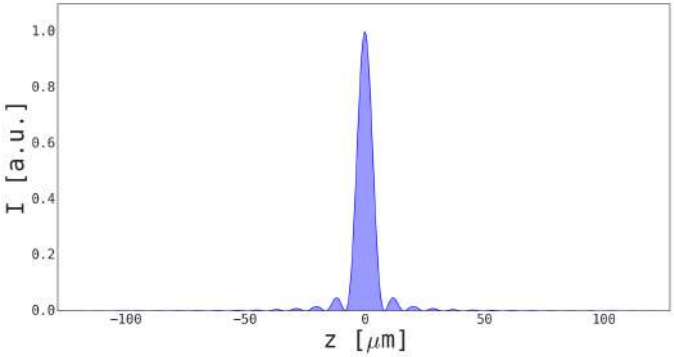

Figure 2.9: $\hat{z}$ in focus excitation

Figure 2.8 and 2.9 represent the field distribution in the objective focal plane: as expected (in order to obtain planar illumination) we've got an uniform profile along $\hat{x}$, while there is a very peaked function along $\hat{z}$, that defines the thickness of the excited sample slice. Moving then along the propagation axis, we can inspect how the applied defocus changes the excitation profile by plotting $\{\hat{x}, \hat{z}\}$ slices at different depths (figure 2.8) and finally extended $\{\hat{y}, \hat{x}\}$ and $\{\hat{y}, \hat{z}\}$ profiles.

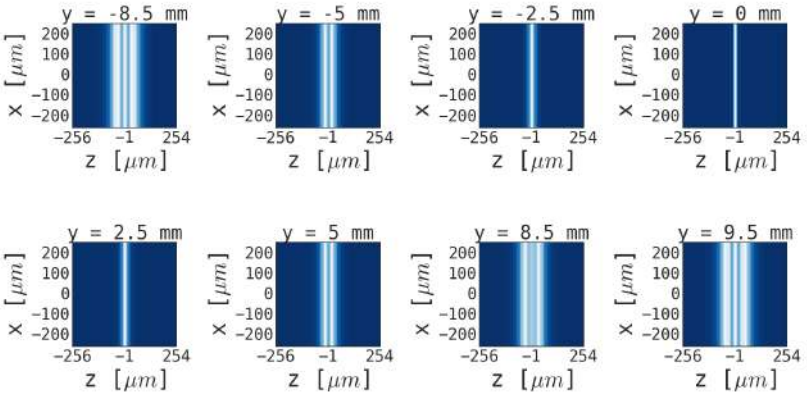

Figure 2.10: 3D excitation profile - $\{\hat{x}, \hat{z}\}$ planes

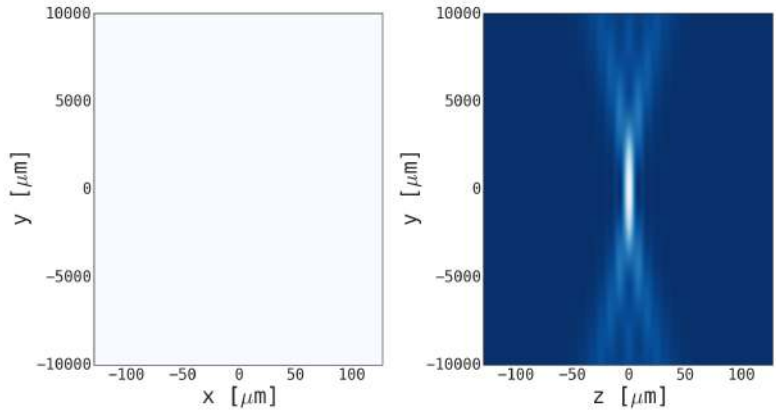

Figure 2.11: 3D excitation profile - $\{\hat{y}, \hat{x}\}$ and $\{\hat{y}, \hat{z}\}$ planes

2.2.4 Detection PSF

The collection geometry is a classical objective-tube lens couple: it's best characterized with the detection Point Spread Function (PSF), which will critically depend on the objective numerical aperture.

PSF can be also called *impulse response function*, and this name probably better reveals the principal characteristic of this classical imaging arrangement: the apparatus is a *linear shift-invariant system*, that creates a magnified image of a sample slice, transferring a portion of its spectrum. This low-

pass filtering is due to the finite extent of the objective pupil, that defines a coherent transfer function (CTF): it acts as a cookie-cutter (always being in paraxial approximation) on a portion of the object spectrum.[9]

The pupil function in this case can be modelled as a *circ* function, defined as:

$$circ\left(\frac{r}{D}\right) = \begin{cases} 1 & if \quad r < \frac{D}{2} \\ \frac{1}{2} & if \quad r = \frac{D}{2} \\ 0 & \text{otherwise} \end{cases} \tag{2.11}$$

where D indicates the aperture diameter.

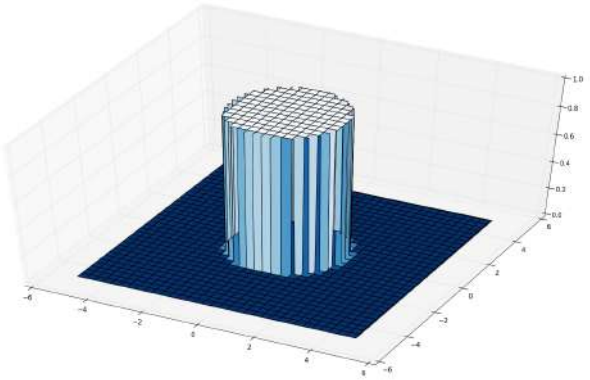

Figure 2.12: *circ* function

Following Tyo,[12] let's find out the expressions for Coherent

Transfer Function, then, after an Inverse Hankel Transform,[13] Coherent Spread Function (CSF): this is equivalent of describing the filtering operation from frequency to spatial domain. Finally, since fluorescence is an incoherent phenomenon, the square modulus of CTF gives the PSF: after all, its convolution with the object describes the image formation.

$$CTF(\rho) = circ\left(\frac{\lambda\,\rho}{\mathrm{NA}}\right) \tag{2.12}$$

$$CSF(r) = \frac{\mathrm{NA}^2}{\lambda^2}\; somb\left(\frac{\mathrm{NA}}{\lambda}r\right) \tag{2.13}$$

$$PSF(r) = \left|\frac{\mathrm{NA}}{\lambda}\right|^4 \left|somb\left(\frac{\mathrm{NA}}{\lambda}r\right)\right|^2 \tag{2.14}$$

Here $\mathrm{NA} = nsin(\theta)$ indicated the objective Numerical Aperture. In this particular case it's possible to analytically evaluate in a fairy simple way an expression also for the PSF axial profile,[7,14] following steps similar to those discussed previously about the excitation profile. Starting from the Coherent Transfer Function, let's apply a defocus z in the axial direction:

$$CTF(\rho; z) = CTF(\rho) \cdot e^{ikz}\, q^*\left(\rho; \lambda z\right) \tag{2.15}$$

Then perform an Hankel Transform to evaluate the extended Coherent Transfer Function:

$$CSF(r;z) = \int_{-\infty}^{+\infty} CTF(\rho)\, e^{ikz}\, q^*\left(\rho;\lambda z\right) J_0(2\pi r\rho)\, \rho\, d\rho \tag{2.16}$$

where J_0 is the Bessel function, zero order, first kind. Then, restricting the discussion to retrieve the profile along the optical axis:

$$\begin{aligned} CSF(0;z) &= \int_{-\infty}^{+\infty} CTF(\rho)\, e^{ikz}\, q^*\left(\rho;\lambda z\right)\, \rho\, d\rho \\ &= e^{ikz} \int_0^{\frac{NA}{2\lambda}} e^{-\pi i\lambda z\rho^2} \rho d\rho \\ &= \frac{e^{ikz}}{2\pi i\lambda z}\left(1 - e^{-\pi i z\frac{NA^2}{2\lambda}}\right) \end{aligned} \tag{2.17}$$

And finally, taking the square modulus:

$$PSF(0;z) = \left(\frac{4\lambda^2}{\sqrt{\pi}NA^2}\right)^2 sinc^2\left(\frac{\pi z NA^2}{4\lambda}\right) \tag{2.18}$$

It's then apparent that being able to control both wavelength and Numerical Aperture would allow to manipulate the desired detection resolution. In real applications it's usually the excitation profile (sheet thickness) that sets the boundaries of the actual sample slice that can be imaged, but it will be clear in Chapter 6 how it is anyway possible to obtain information about 3D flow fields (trackers leaving/entering the exci-

tation plane) studying the evolution of spatio-temporal cross-correlation functions, which will be introduced in section 2.4.

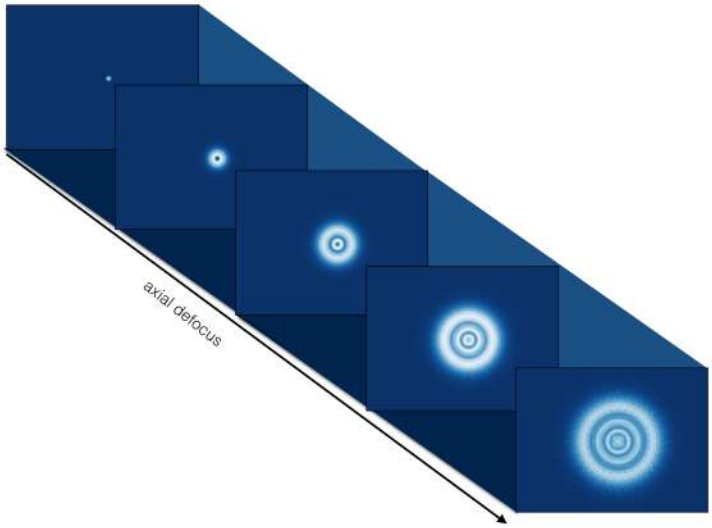

Figure 2.13: Simulation of 3-D detection PSF - 100μm per step. All Python codes are available, see Appendix

2.3 Setup realization of SPIM

I have implemented two SPIM setups: the first dedicated to in-vitro measurements, the second for in-vivo studies.

2.3.1 In-vitro setup

in figure 2.14 I show the actual setup that I assembled for in-vitro measurements, as already depicted in figure 2.2:

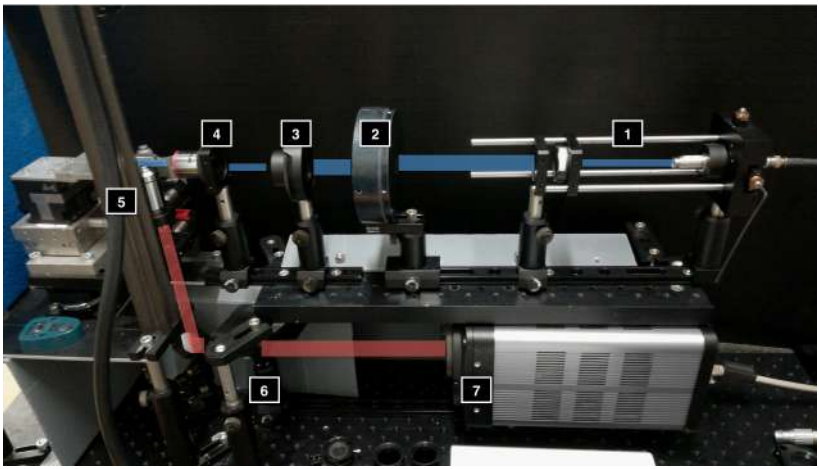

Figure 2.14: SPIM setup for in-vitro measurements.

Laser source is an argon-krypton (Melles Griot), from which both a 488 nm and 514 nm excitation wavelengths can be selected. Following the numbers in the figure, let's review the optical path components:

1. beam-expander(1:4): two lenses (focal lengths of 10 mm and 40 mm respectively) in a telescopic configuration, in

order to expand the incoming laser beam;

2. variable rectangular slit: the aperture stop described by eq. 2.1: in this configuration, it creates a thin horizontal aperture, in order to obtain a uniform horizontal sheet of light on the sample;

3. cylindrical lens, positioned at a distance of $50 mm$ (which corresponds to its focal length) both from the objective and the slit;

4. excitation objective: Olympus, 4X, 0.1 NA;

5. detection objective: Olympus, 20X, water immersion, 0.95 NA;

6. tube lens, focal length $150\, mm$;

7. EMCCD detector (Cascade II Photometrics).

Pixelated detector

The detector is extremely important, because it heavily impacts on both spatial and temporal resolutions. While high pixel number allows a large FOV, pixel size is directly related to spatial resolution, but it's useful (in particular when selecting an appropriate detector) to think about the whole setup: since the system PSF must work together with pixels dimension, it's no use to simply think about decreasing as much as possible pixels area.[15] The reason resides in the Nyquist Theorem, that can be stated as: *a continuous function can be completely represented by a set of equally spaced samples, if the samples occur at more than twice the frequency of the highest frequency component of the function.* Thus, comparing Abbe limit with pixel size e, and fulfilling Nyquist requirement, then:

$$e < 0.3\frac{\lambda}{NA}M \tag{2.19}$$

where M is the magnification.

In this case the camera employed is an EMCCD (Cascade II Photometrics), with an active area of 512x512 pixels (16 μm side), so that, in fact, it's only the pixels size that sets the highest spatial resolution theoretically achievable. This small detail will gain importance in Chapter 6: there I will explain how to deal with this restriction, in particular when deriving

an expression for the theoretical spatio-temporal correlation model.
Besides this slight loss of spatial resolution (anyway more than sufficient for imaging all the desired features in investigated samples) the most important characteristic of the detector resides in its sampling speed and in its great sensitivity, coupled with an efficient *signal-to-noise* $\left(\frac{S}{N}\right)$ ratio.

Figure 2.15: Cascade II - Photometrics

EMCCD stays for Electron Multiplying Charge Couple Device and it is actually an evolution of CCD camera, basically with the same detection technology: a semiconductor substrate is separated by a thin layer of isolating material (usually SiO) from an array of conductive plates, which create a series of potential wells: exposure to light generates (via photoelec-

tric effect) charges stored in this wells, and then a relative scaling of potentials within a clock cycle allows to move the electrons towards the bottom pixels line.

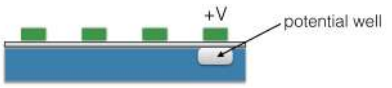

Figure 2.16: Schematic of CCD pixels

The last line is sequentially emptied and read by the ADC (Analog to Digital Converter), that sends an electric signal to a computer, composing an image. There are two main drawbacks when employing CCDs: the first one is noise, and the second is dead time between acquisitions.
The primary source of uncertainty is thermal noise, that can be reduced with various cooling systems, from air cooling (trying to maintain a device at T_{amb}) to the employment of Peltier cells (reaching $-70°C$).
For what concerns dead time, there are currently two kinds of solutions available, both based on employing only half the CCD chip to collect an image, while the other half is reserved only for data transfer: the first arrangement considers the chip composed by many couples of lines, one for registering and one

for data transfer (*line transfer architecture*), while the other one divides the whole chip in two separate regions, one receptive and one blind (*frame transfer*).
EMCCD employs both *frame transfer* geometry and Peltier cooling cells, being, just with these two characteristics, a great device, capable of reaching a maximum acquisition speed of $\frac{4\,ms}{image}$ when employing a 20 pixels line subregion. The other great improvement resides in the reduction of the second major source of noise, that happens in the ADC conversion, the readout noise. In the EMCCD configuration, electrons don't have to travel towards the bottom line of the chip for digital conversion, but they move horizontally towards an additional line, passing, for every step, from low voltage to an extremely high voltage. In this way, by impact ionization, a number of electron-hole couple is created, proportional to the number of electrons present in a well (from here the name electron multyplying). The result is an increased number of electrons, before the digital conversion, while readout noise is unaltered, giving a huge $\frac{S}{N}$ increase.

sCMOS cameras

A valid alternative to EMCCD cameras is represented by devices fabricated with a completely different architecture, based

on complementary metal-oxide semiconductors (CMOS). CMOS detectors consist of arrays of integrated transistor devices, each acting as a photodetector coupled with an amplifier. Usually the transistor gate voltage is regulated by a photodiode: at the beginning of each exposure the gate voltage is set to a baseline value and decreased when light, impinging on the photodiode, creates a leak current. The resistance across the transistor is then evaluated, obtaining a measure of light intensity.
Modern scientific CMOS (sCMOS) cameras can achieve higher resolution and framerate than EMCCD cameras, but at the present time still sensitivity performances favour EMCCD devices. As en example, one of the best sCMOS on the market (Hamamatsu ORCA-Flash 4.0 V3) has 82% quantum efficiency (peak @560 nm) with an effective readout noise of 1.6 e^- rms, capable of achieving 100 $\frac{frames}{sec}$ at full 2048x2048 resolution, while one of the best EMCCD detectors (Photometrics Evolve 512 Delta) has 96% quantum efficiency (peak @550 nm), with effective readout noise $< 1e^-$ rms, and can achieve 67 $\frac{framse}{sec}$ at full 512x512 resolution.

Calibration: sheet thickness measurement

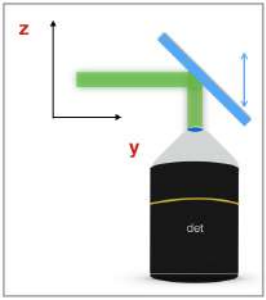

Figure 2.17: Measurement of sheet thickness for air SPIM setup and fitting example

A first system calibration step consists in the evaluation of sheet thickness, which sets the practical sheet thickness. Calibration data were collected by means of a mirror positioned instead of the sample, and mounted at 45° with respect to the excitation propagation direction $\hat{y}$, so that it was possible to register excitation profiles along the full field of view.

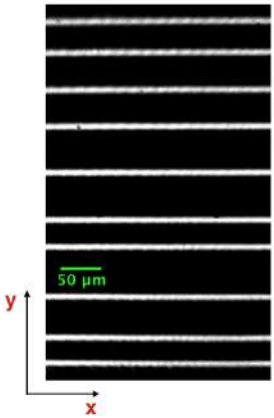

Figure 2.18: Maximum projection of light sheet thickness collection.

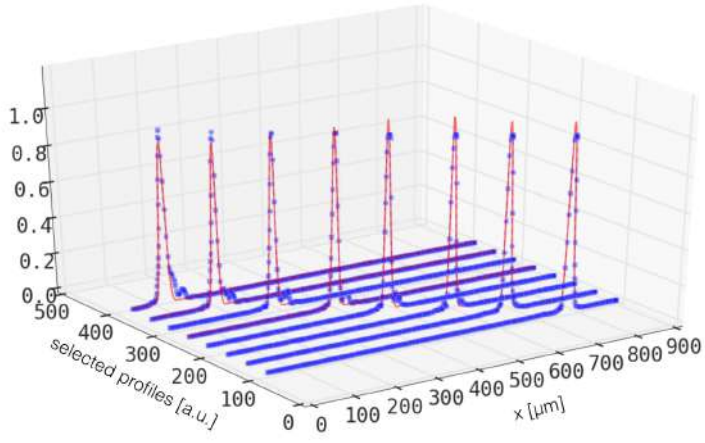

Figure 2.19: Fitting calibration data, with normalized intensities.

I wrote a Python program for fitting multiple peaks with a Gaussian model, applied in this case to retrieve a value for FWHM,[16] resulting: $11.2 \pm 1.5\,\mu m$. This value is in agreement with the previously reported theoretical estimation of $10\,\mu m$.

2.3.2 In-vivo setup

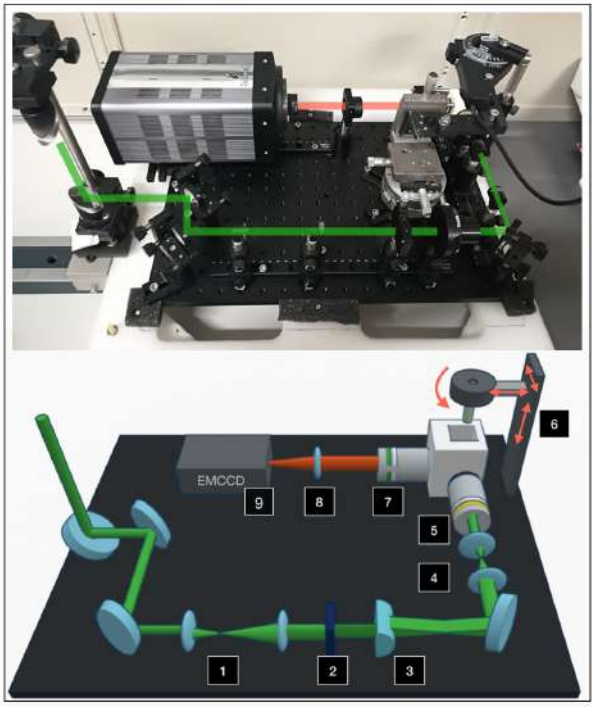

Figure 2.20: In-vivo SPIM setup

In this case the source is an Argon laser: as for the previous setup, both 488 nm and 514 nm excitation wavelengths can be selected. Following the numbers in figure 2.20:

1. beam expander (1:2): two lenses (focal lengths of 25 mm and 50 mm respectively) in a telescopic configuration, in order to expand the incoming laser beam;

2. variable rectangular slit, again as described by eq. 2.1: in this configuration, it creates a thin *vertical* aperture, in order to obtain a uniform *vertical* sheet of light on the sample;

3. cylindrical lens, positioned at a distance of 50mm (which corresponds to its focal length) from the slit, and conjugated with the following lens;

4. beam reducer (2:1): two lenses (focal lengths of 50 mm and 25mm respectively) in a telescopic configuration, the exact opposite of the previous one, in order to reduce the incoming laser beam, to fill the objective back aperture;

5. excitation objective: Olympus, water dipping, 10X, 0.3 NA;

6. sample stage;

7. detection objective: Olympus, water dipping, 20X, 0.5 NA;

8. tube lens, focal length 150 mm;

9. EMCCD detector (Cascade II Photometrics).

Immersion chamber

In order to study live zebrafish embryos in the best environment, while conserving an optimal index matching, an immersion chamber was designed[5] and 3D printed (PLA): plastic o-rings assured the perfect fitting of both excitation and detection objectives, while the (rotating) sample holder allows full manipulation and free *slice selection*.

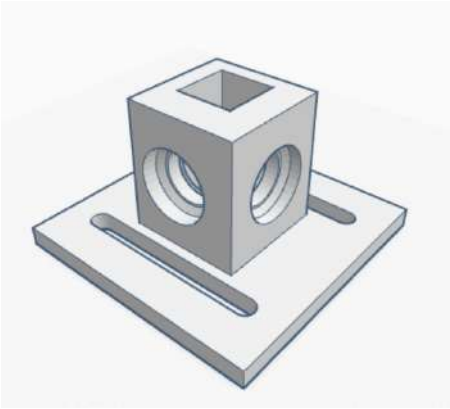

Figure 2.21: Immersion Chamber, CAD schematic

Calibration: sheet thickness measurement

As done in the previous section, it's possible to measure the light sheet thickness with a tilted mirror instead of the actual sample. Following exactly the same procedure, over all the available field of view, an then fitting with a Gaussian model, the retrieved value resulted in $FWHM = 17.8 \pm 1.4 \mu m$. This value is clearly larger than the one reached in the first described setup, but this is purposely done for experimental reasons: it is in fact found that, in order to obtain a more uniform sectioning in biological samples (where in particular index matching is a challenge and a primary source of aberrations), we must face a trade-off between sheet thickness (creating a wider slit aperture) and illumination uniformity. A great solution, already proposed by Dean Wilding et al.,[10] consists in the employment of a spatial light modulator (instead of a passive slit), which would allow to use adaptive optics algorithms to achieve active beam manipulation and an overall improved excitation efficiency.

2.4 Image Correlation Spectroscopy - ICS

Image Correlation Spectroscopy revolves around the study of the evolution of similarities residing in signals coming from a 3D image stacks and linking them to quantifiable physical processes, such as diffusion, directional flow, chemical reactions, or tracers' photo-dynamics. I think that the most interesting fact, in this case, is that this technique is applied to study fluctuations in fluorescence intensities, that is to analyse something that, when commonly seen from an imaging point of view, is usually discarded as *noise*, and, at the very least, is considered a problem to be solved. Actually it has been extensively demonstrated that intensity fluctuations carry all the information needed to precisely characterize drift motions, that is our goal. It substantially helps the investigation of moving objects, since, by working on fluctuations, it naturally gets rid of the impact of any still, undesired background. In order to understand the two principal implementation of this method that I have been employing in my work, I want here to review the basics: it was all born from the work of Magde et al.[6] in 1972, with the developed Fluorescence Correlation Spectroscopy.

2.4.1 Standard FCS theory

The idea is to record a temporal series of fluorescence intensity fluctuations inside a tiny (μL) focal volume and use it an input inside the correlation machinery: it is in this case called "autocorrelation" since only one signal is employed. The term *cross-correlation* is reserved instead to analysing similarities between two spatially separated signals.
The paradigm of correlation function is:

$$G(\tau) = \frac{\langle \delta I(t)\, \delta I(t+\tau) \rangle_t}{\langle I \rangle^2} \tag{2.20}$$

where $\delta I(t) = I(t) - \langle I(t) \rangle_t$ is the temporal fluctuation of fluorescence intensity. Intuitively, any perturbation, any evolution from a perfect spatio-temporal infinitely uniform state, will cause a loss of self-similarity in $I(t)$, i.e., as it will be shown shortly, $G(\tau)$ is bound to decay with growing lag-time τ.
In order to get a precise insight into the physical/chemical processes involved in the evolution of the studied system, model fit functions can be obtained.[17–19] In this work, I am mainly interested in variations in fluorophore concentration, generated by Brownian or drift motions. In this case, it's possible to rewrite eq. 2.20 as:

$$G(\tau) = \frac{\int |W(\vec{q})|^2 \hat{P}(\vec{q},\tau) d\vec{q}}{|W(0)|^2 \langle C \rangle} \tag{2.21}$$

where

- $W(\vec{q})$ is the Fourier Transform of the Molecular Detection Efficiency function (MDE);
- $\hat{P}(\vec{q},\tau)$ is the Fourier Transform of the concentration correlation function $P(\vec{r},t)$;
- $\langle C \rangle$ is the average fluorophore concentration.

For the time-scales accessible to the SPIM setups, where reside the interesting dynamics that I want to investigate, the primary sources of time-evolution are Brownian diffusion and deterministic drift. We can therefore refer to Fick's law that gives a differential equation for the probability function $P(\vec{r},$ that is the probability to find a particle in $\vec{r}$ at t when it was in $\vec{r} = 0$ at time $t = 0$:[20]

$$\frac{d}{dt} P(\vec{r},t) = D\,\nabla^2 P(\vec{r},t) - \vec{v}_{drift} \nabla \cdot P(\vec{r},t) \tag{2.22}$$

with $D = \frac{kT}{6\pi\eta R}$ diffusion coefficient and v_{drift} = drift speed. It's best to solve this equation with a spatial Fourier Transform:

$$\frac{d}{dt}\hat{P}(\vec{q},t) = Dq^2\hat{P}(\vec{q},t) - i\vec{q}\,\vec{v}_{drift}\hat{P}(\vec{q},t) \tag{2.23}$$

$$\hat{P}(\vec{q},t) = \langle C\rangle\, e^{-Dq^2t - i\vec{q}\,\vec{v}_{drift}t} \tag{2.24}$$

Finally, for this theoretical treatment, we can approximate the MDE as 3D Gaussian,[19] so that:

$$W(\vec{r}) = I_0\, e^{-2\frac{x^2+y^2}{\omega_0^2}}\, e^{-2\left(\frac{z}{z_0}\right)^2} \tag{2.25}$$

ω_0 being the beam waist and z_0 Rayleigh range. Then from equation 2.20 we obtain the complete expression:

$$\begin{cases} G(\tau) = \; G(0)\, G_{diff}(\tau)\, G_{drift}(\tau) \\ G(0) = \; \frac{\gamma}{\langle N\rangle}\,,\; \gamma = 0.35 \text{ for 3D gaussian MDE} \\ G_{diff}(\tau) = \frac{1}{1+\frac{\tau}{\tau_D}} \frac{1}{\sqrt{1+\frac{\tau}{\tau_D}\left(\frac{\lambda}{\pi\omega_0}\right)^2}} \\ G_{drift}(\tau) = \exp\left[-\left(\frac{\tau}{\tau_{drift}}\right)^2 \frac{1}{1+\frac{\tau}{\tau_D}}\right] \end{cases} \tag{2.26}$$

where:

- $\langle N\rangle$ is the average number of fluorescent particles inside the investigation volume, and it can be also expressed as $V_{exc}\,C$. C is the number concentration, while (for the 3D Gaussian) $V_{exc} = \frac{\left(\int W(\vec{r})d^3\vec{r}\right)^2}{\int W^2(\vec{r})d^3\vec{r}} = \pi\omega_0^2 z_0 \simeq 10 - 100fL$;

- $\tau_D = \frac{\omega_0^2}{4D}$ is the decay time of the diffusion component;
- $\tau_{drift} = \frac{\omega_0}{v_{drift}}$ decay time of the drift component.

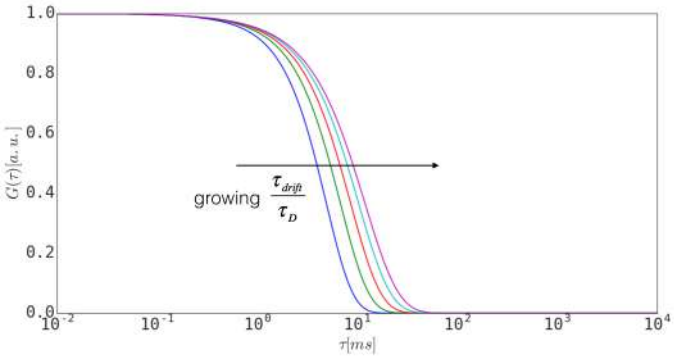

Figure 2.22: Simulation of $G(\tau)$ for growing values of τ_{drift}, ranging from 5 to 12 ms.

Three main observations may be highlighted here:

1. $G(\tau)$ intensity strongly depends on concentration, so that, in order to have a high fluctuation signal $G(0)$, easily recorded by a CCD or CMOS camera (that is, higher than the dark noise) we need to work in a concentration range of 10-100 nanomolar: in fact for excitation volumes of the order of 100 fL we obtain $\langle N \rangle \simeq 6 - 60$;

2. at first glance $G(0)$ seems to reach infinity for an extremely low particle number. Actually evaluating 2.20 for zero lag-time gives:

$$G(0) = \frac{\langle \delta I(0)^2 \rangle}{\langle I(0) \rangle^2}$$

Expressing intensity signal as a sum of fluorescence F and background B, under the hypothesis of fluorescence being proportional to particle number ($\langle F \rangle^2 = \alpha \langle N \rangle^2$), it's clearly found that:

$$G(0) = \frac{\langle \delta(F+B)^2 \rangle}{\langle F+B \rangle^2} = \frac{\alpha \langle N \rangle^2}{\alpha \langle N \rangle^2 + \langle B \rangle^2} \frac{\gamma}{\langle N \rangle}$$

In this way it's apparent how the signal will never reach infinity:

$$\langle N \rangle \to \infty \;\Rightarrow\; G(0) \simeq \frac{\gamma}{\langle N \rangle}$$
$$\langle N \rangle \to 0 \;\Rightarrow\; G(0) \simeq \frac{\alpha}{\langle B^2 \rangle} \gamma \langle N \rangle$$

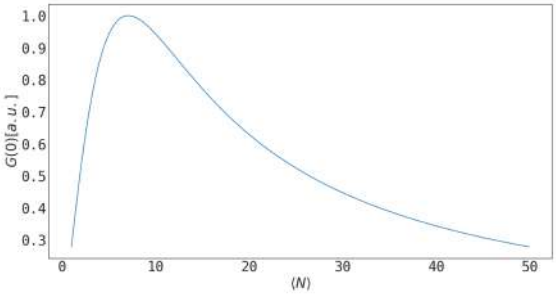

Figure 2.23: Simulation of zero lag-time correlation for different values of fluorescent molecules concentration.

3. it's apparent from figure 2.22 that, despite from a single fit should be theoretically possible to retrieve both τ_D and τ_{drift}, this is very difficult, since the shape of G changes only slightly with the presence of $\vec{v}_{drift}$, and often, if only Brownian diffusion is supposed, information about any drift velocity is lost. To overcome this major difficulty, and also to take advantage of the large FOV of the images collected with SPIM, I employed (in particular for the work presented in Chapter 4) an evolution of this method, called spatially resolved FCS (sFCS).

2.4.2 sFCS

This is a spatially resolved variant of FCS, in which two volumes, separated by a distance $\vec{S}$ along the flow direction, are selected inside the sample and cross-correlated. The result is a peak function that allows a clear separation between the impacts of τ_D and τ_{drift}, that is between diffusion and drift: the first one is primarily responsible for the overall decay of the function and for the broadening of the Gaussian peak (as it will be soon described), while the second one will cause a displacement of the peak along the lag-time axis. Following the derivation of the last paragraph, the cross-correlation function is:

$$G_{1,2}(\tau) = \frac{\langle I_1(t)\, I_2(t+\tau)\rangle}{\langle I_1\rangle \langle I_2\rangle} \tag{2.27}$$

To dive inside the physical parameters that describe the equation, it's possible to follow again equation 2.20, taking care of adding a spatial phase term, since the two signals are spatially separated:

$$G(\tau) = \frac{\int |W(\vec{q})|^2 e^{-i\vec{q}\vec{S}} R(\vec{q},\tau) d\vec{q}}{|W(0)|^2 \langle C\rangle} \tag{2.28}$$

This basically gives the same function as in (2.25), but, as anticipated, with a Gaussian drift term, peaking at the average

flight time required by fluorescent particles to travel $\vec{S}$:

$$\begin{cases} G_{1,2}(\tau) = \; G(0)\, G_{diff}(\tau)\, G_{drift}(\tau) \\ G(0) = \; \frac{0.35}{\langle N \rangle} \\ G_{diff}(\tau) = \frac{1}{1+\frac{\tau}{\tau_D}} \frac{1}{\sqrt{1+\frac{\tau}{\tau_D}\left(\frac{\lambda}{\pi\omega_0}\right)^2}} \\ G_{drift}(\tau) = \exp\left[-\left(\frac{\vec{S}-\vec{v}\,\tau}{\omega_0}\right)^2 \frac{1}{1+\frac{\tau}{\tau_D}}\right] \end{cases} \tag{2.29}$$

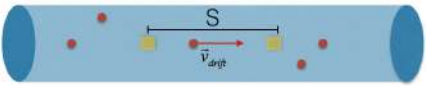

Figure 2.24: In a microchannel filled with fluorescent trackers (red particles) two investigation ROIs are chosen (usually squares of side 1 to 5 pixels) from which $I_1(\tau)$ and $I_2(\tau)$ are analysed.

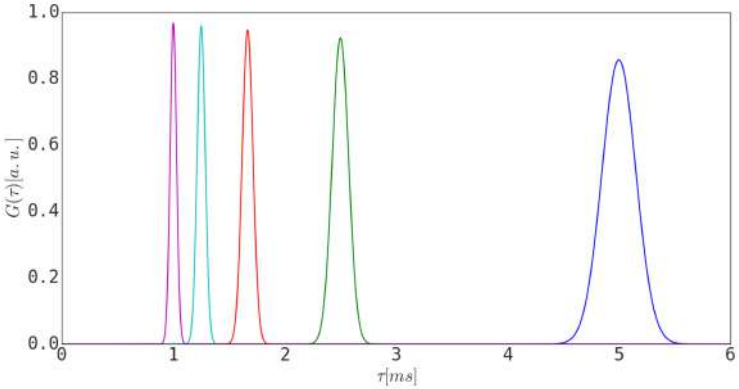

Figure 2.25: Simulation of $G_{1,2}(\tau)$ for growing values of $\vec{v}_{drift}$, ranging from 10 to 50 $\frac{\mu m}{s}$. Other parameters are: $\tau_D = 30ms$, wavelength = 500 nm, $\omega_0 = 2\mu m$

Equation 2.29 can be greatly simplified, in particular for the microfluidic structures and regimes that I employed. In fact, a rapid calculation shows that the diffusion time constant (supposing T = room temperature and fluorescent particles mean radius $R = 1\mu m$) is of the order $30ms$; when analysing both in-vitro or in-vivo flows, usually we deal with velocities that are around hundreds of $\frac{\mu m}{s}$, on distances of tens of microns. This means that, as explained also in Chapter 4, the Gaussian peak is estimated at lag-times that allow the simplification:

$$\frac{1}{1+\frac{\tau}{\tau_D}} \simeq 1 \tag{2.30}$$

So that, at first approximation:

$$\begin{cases} G'_{1,2}(\tau) = \ G(0)\ G'_{drift}(\tau) \\ G(0) = \ \frac{0.35}{\langle N \rangle} \\ G'_{drift}(\tau) = \exp\left[- \left(\frac{|\vec{S} - \vec{v}\,\tau|}{\omega_0} \right)^2 \right] \end{cases} \tag{2.31}$$

This equation is extremely clear about the core information that I want to retrieve: the peak lag-time will immediately inform about the speed in the studied subregion of the sample. A possible drawback is that the definition of the investigation volumes (V_1 *and* V_2), from which fluorescence signals are acquired, already supposes a prior (at least vague) knowledge about the flow direction. Usually this is not a huge problem, since a rapid inspection of the acquired image stacks is enough to understand where I can correctly perform the analysis, according to 2.31, doing it efficiently off-line. Moreover in order to overcome this possible limitation (avoiding a somehow subjective and time consuming volumes selection) Chapter 5 will deal especially with a new evolution of the correlation techniques proposed, that is Spatio-Temporal Cross-Correlation Spectroscopy (STICS).

2.4.3 STICS

This is a powerful technique that, although requiring wide field images acquired at high speed (so being demanding in terms of hardware and computer power), allows a complete mapping of flow and diffusion phenomena in space (at first instance in 2D, but see chapter 6 for a 3D evaluation). STICS can be directly seen as a generalization of sFCS, as it can be appreciated by inspecting the definitio of the generalized spatio-temporal correlation function:

$$G(\xi,\eta,\tau) = \left\langle \frac{\langle \delta I(x,y,t)\rangle_{x,y} \langle \delta I(x+\xi,y+\eta,t+\tau)\rangle_{x,y}}{\langle I(x,y,t)\rangle_{x,y} \langle I(x,y,t+\tau)\rangle_{x,y}} \right\rangle_{t} \tag{2.32}$$

Following the same procedure described in the previous section (I will get into a more detailed description in Chapter 6), the 2D fit function that explicitly reveals the physical parameters of interest is:[18]

$$G(\xi,\eta,\tau) = \frac{1}{\langle C\rangle \pi\omega_0^2} \frac{1}{1+\frac{4D}{\omega_0^2}} \exp\left[-\frac{1}{\omega_0^2} \frac{|\xi - v_x\tau|^2 + |\eta - v_y\tau|^2}{1+\frac{4D}{\omega_0^2}} \right] \tag{2.33}$$

ξ, η are the spatial-shifts, that is components of a rigid displacement vector applied between image couples before su-

perimposing (multiplying) them and integrating, and $\{v_x, v_y\}$ being components of the velocity field associated with a flow. In case of multiple flows, as extensively described in Chapter 5, multiple exponential contributions are expected, each one depending on a specific $\vec{v}_{flow,\,i}$.

In the most emblematic case, the investigated sample may presents unknown (both in magnitude and direction) flows (and eventually diffusion): under the assumption that both spatial and temporal resolutions are high enough to sample significant phenomena, a fast video recording with a SPIM setup gives the perfect data sets to be analysed by STICS. All the analysis can be performed off-line, following a well established algorithm, that I have extensively tuned and improved as described in Chapter 5:

1. ROI selection: subregions inside the sample are selected and sequentially analysed. The aim is both to decrease computational costs and to obtain a clearer, finer spatial mapping, since in every region less velocity components are expected, underlying simpler geometries.

2. Calculatoin of the temporal and spatial fluctuations calculation: in order to subtract immobile fraction, highlighting signals coming from moving fluorescent objects, and also to account for slow possible excitation inten-

sity variations, fluctuations are computed, respectively in space and time, following $\delta I(x,y,t) = [I(x,y,t) - \langle I(x,y,t)\rangle_t] - \langle I(x,y,t)\rangle_{x,y}$

3. Selection of the range of the lag-times: given a ROI maximum extension $\{M \times N\}$, a lag-time τ choice will determine the velocity range that can be detected: there is an ideal theoretical limit on the maximum speed detectable by a spatial correlation, that is $v_{max} = \frac{\sqrt{M^2+N^2}d_p}{2\tau}$ (with d_p pixel size). Moreover, as discussed in Chapter 5, usually a more conservative approach is kept, in order to preserve high $\frac{S}{N}$.

4. Spatial cross-correlations are performed (in frequency domain, to obtain fast computational speed) between ROI couples spaced τ in time, then an average of the results gives the 2D flow map (see figures 2.26 2.27)

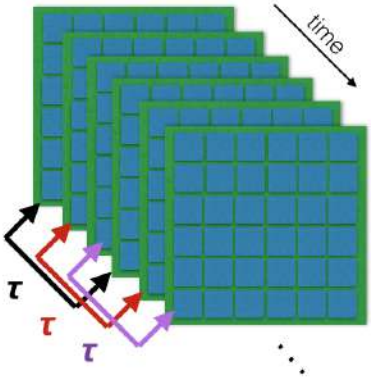

Figure 2.26: Schematic representation of ROI coupling and correlation: one a lag-time τ has been chosen, it is rigidly translated selection successive couples of regions, spanning all the temporal window available. Spatial-correlation is performed between these couples, finally averaging results.

For this work, employing low level libraries (e.g. numpy, C based) and optimized vectorial operations was sufficient to allow me to obtain high computational speeds (few tens of seconds per map (50x50 pixels) in the slowest case). Of course a future improvement would be to shift towards parallel GPU programming, harvesting the power of modern graphics cards (e.g. with OpenGl or CUDA libraries).

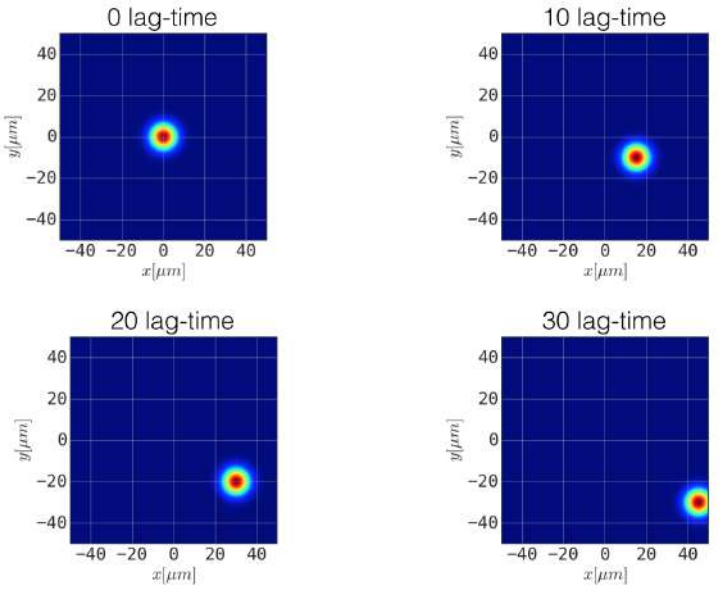

Figure 2.27: Simulations of STICS maps: the bright peak informs about a single velocity steady flow, and it travels in space as lag-time increases: this is the spatial shifts that has to be applied between each image couple in order to retrieve the maximum similarity, after τ lag times.

Practical considerations Cross-correlation analysis is capable of bringing into evidence similarities between signals at varying reciprocal offsets. The 1D cross-correlation function

general mathematical model is:[13]

$$\gamma_{f,g}(x) = \int_{-\infty}^{\infty} f(\alpha)\, g^*(\alpha - x) d\alpha = \int_{-\infty}^{\infty} g^*(\beta)\, f(\beta + x) d\beta$$

The fastest computational performances are reached exploiting the extremely efficient Fast Fourier Transform algorithm: in fact, the convolution theorem shows that correlation and convolution are closely related:

$$\gamma_{f,g}(x) = f(x) \otimes g^*(-x) = F(\xi) \cdot G^*(\xi) \tag{2.34}$$

where F and G are Fourier Transforms of f and g, respectively.

The last equality (holding for real-valued functions) shows that convolution becomes a simple product in frequency space: this procedure is extremely fast, and applies also to 2D signals in STICS analysis. Furthermore exploiting ROI selection, it can always be chosen a rectangular subregion of $N^2 \times M^2$ pixels, heavily improving computational efficiency of FFT algorithm.[21]

2.5 Microfluidics

The last theoretical topic that I will briefly introduce here is the well known description of microscale fluid mechanics: experimental work will be focused on studying time-dependent flows inside microchannels, which satisfies the Navies-Stokes equation and can be also treated in analogy with a lumped-circuit analysis.

Governing equations

Throughout all the discussion, the *continuous hypothesis* will hold, that is I will follow Bruus[22] definition of fluid: its macroscopic properties are the same as if the fluid were perfectly continuous in structure instead of, as in reality, consisting of molecules. In fact, although fluids are quantized on the length scale of inter-molecular distances (of the order $0.3nm$ for liquids), here they appear continuous since we are dealing with macroscopic length scales of the order 100 μm or more. In the most general form, the equations of fluid motion stem from considering a general volumetric property of interest and keeping track of how it changes over time across a fluid volume element. If Q is a general volumetric property of the fluid, then:

$$\frac{d}{dt}\int_\sigma Q\,d\sigma = -\int_S Q\,\vec{v}\cdot\hat{n}\,ds + \\ + \text{any mechanism to produce/destroy Q} \tag{2.35}$$

where:

- $\frac{d}{dt}\int_\sigma Q\,d\sigma$ is the time variation of Q inside a volume element $d\sigma$;
- $\int_S Q\,\vec{v}\cdot\hat{n}\,ds$ represents its efflux (outflow).

There are three major applications of this production/conservation model, connected to mass, momentum, and energy conservation.

Mass conservation With $Q = \rho$ and under the hypothesis that mass can't be produced or destroyed inside the volume element:

$$\frac{d}{dt}\int_\sigma \rho\,d\sigma = -\int_S \rho\,\vec{v}\cdot\hat{n}\,ds \tag{2.36}$$

Momentum conservation When $\vec{Q} = \rho\vec{v}$ = linear momentum:

$$\frac{d}{dt}\int_\sigma \rho\vec{v}\,d\sigma = -\int_S \rho\vec{v}\,\vec{v}\cdot\hat{n}\,ds + \int_\sigma \vec{f}\,d\sigma + \int_S \vec{T}\,ds \tag{2.37}$$

In this case two kinds of forces are modelled:

- $\vec{f}(\vec{x})$ = body force per unit volume, that is in general an action across a distance;
- $\vec{T}(\vec{x})$ = traction force per unit area.

In particular, $\vec{T}$ is directly related to the stress tensor, defined as a linear transformation that associates the normal to a surface element ds to the traction force on that element: $\vec{T} = \vec{\tau} \cdot \hat{n}$. Being able to ignore the body force, we get the compact expression:

$$\frac{d}{dt} \int_{\sigma} \rho \vec{v} \, d\sigma = - \int_{S} (\rho \vec{v} \, \vec{v} - \tau) \cdot \hat{n} \, ds \tag{2.38}$$

Energy conservation Considering $Q = \rho E_t$ with E_t = specific total energy = $e + \frac{1}{2}\vec{v}\vec{v}$, being e the internal energy, then:

$$\frac{d}{dt} \int_{\sigma} \rho E_t \, d\sigma = - \int_{S} \rho E_t \vec{v} \cdot \hat{n} \, ds + \int_{\sigma} \vec{f} \cdot \vec{v} d\sigma + \int_{S} \vec{T} \cdot \vec{v} ds - \int_{S} \vec{q} \hat{n} ds \tag{2.39}$$

Again, ignoring body forces and expanding $\vec{T}$:

$$\frac{d}{dt} \int_{\sigma} \rho E_t \, d\sigma = - \int_{S} \rho E_t \, \vec{v} \cdot \hat{n} \, ds + \int_{S} \vec{\tau} \cdot \vec{v} \cdot \hat{n} \, ds - \int_{S} \vec{q} \, \hat{n} \, ds \tag{2.40}$$

As a last step, all the balance equations can be written in an extremely compact way:

$$\frac{d}{dt} \int_{\sigma} Q \, d\sigma = - \int_{S} \vec{F} \cdot \hat{n} \, ds 1 \tag{2.41}$$

$$Q = \begin{bmatrix} \rho \\ \rho\vec{v} \\ \rho E_t \end{bmatrix}, \quad \vec{F} = \begin{bmatrix} \rho\vec{v} \\ \rho\,\vec{v}\,\vec{v} - \vec{\tau} \\ (\rho E_t)\vec{v} - \vec{\tau}\cdot\vec{v} + \vec{q} \end{bmatrix} \tag{2.42}$$

These equations express the fundamental relations from which any microfluidic theory develops. The only thing left to derive Navier-Stokes is to express the second equality in differential form, and to further dive into the expression of the stress tensor τ. First of all, applying Gauss theorem to (2.37), we get to:

$$\rho\frac{d}{dt}\vec{v} + \rho\vec{v}\cdot\nabla\vec{v} = \nabla\cdot\vec{\tau} \tag{2.43}$$

Then considering a Newtonian fluid, τ assumes the expression:

$$\tau_{ij} = -p\delta_{ij} + \sigma'_{ij} \tag{2.44}$$

with p being the pressure and σ'_{ij} being the *viscous stress tensor*: it expresses the ith component of the friction force per unit area acting on a surface element oriented with the surface normal parallel to the jth unit vector e_j. Its general expression results to be:

$$\sigma'_{ij} = \eta \left(\partial_j v_i + \partial_i v_j - \frac{2}{3} \delta_{ij} \partial_k v_k \right) + \zeta \delta_{ij} \partial_k v_k \tag{2.45}$$

where the coefficients η and ζ are denoted the viscosity and second viscosity, respectively. In case of incompressible fluid, $\partial_k v_k = 0$, so that it greatly simplifies into:

$$\sigma'_{ij} = \eta \left(\partial_j v_i + \partial_i v_j \right) \tag{2.46}$$

Considering a uniform viscosity, the divergence of the stress tensor becomes:

$$\partial_j \tau_{ij} = -\partial_i p + \eta \partial_j \partial_j v_i \tag{2.47}$$

Finally resulting in the usual Navier-Stokes equation:

$$\rho \frac{d}{dt} \vec{v} + \rho \vec{v} \cdot \nabla \vec{v} = -\nabla p + \nabla \cdot \eta \nabla \vec{v} \tag{2.48}$$

Furthermore, if we have uniform viscosity:

$$\rho \frac{d}{dt} \vec{v} + \rho \vec{v} \cdot \nabla \vec{v} = -\nabla p + \eta \nabla^2 \vec{v} \tag{2.49}$$

This form of the Navier-Stokes equation is a core building block for every description of flows in all in-vitro systems employed in this work. A rapid calculation of Reynolds number and the application to particular microchannel geometry employed in this work, will help further simplifying the notation, as I will show in the following.

Notational observation The equations displayed here can be cast in any coordinate system, and they should, in order to solve a specific problem. There may be an element of ambiguity in dot products like $(\vec{\tau}\cdot\vec{v}\cdot\hat{n})$ in equation 2.40, but this is not a problem when those are resolved in terms of component,[23] e.g.

$$\vec{T}\cdot\vec{V} = T_i\varepsilon^i\cdot\varepsilon_l V^l = \tau_{ij}\varepsilon^i(\varepsilon^j\varepsilon^k)n_k\cdot\varepsilon_l V^l = \tau_{ij}n^j V^i \qquad (2.50)$$

2.5.1 Reynolds number

The proper way to see if the non-linear term $(\vec{v}\cdot\nabla\vec{v})$ in Navier–Stokes can be neglected is to make the equation dimensionless. This can be accomplished by expressing all physical quantities in units of the characteristic scales e.g.

$$\vec{v} = V_0\vec{u}$$

in this way it seems natural to rewrite Navier-Stokes introducing the dimensionless Reynolds number:

$$Re\,[\partial_t\vec{u} + (\vec{u}\cdot\nabla)\vec{u}] = -\nabla p + \nabla^2\vec{u} \qquad (2.51)$$

$$Re \equiv \frac{\rho\, V_0\, L_0}{\eta} \qquad (2.52)$$

Clearly from Eq. (2.50) it's apparent that for $Re << 1$ the viscous term $\nabla^2\vec{v}$ dominates, while when $Re >> 1$ the inertia

term $(v \cdot \nabla)\vec{v}$ dominates. The systems that I have studied in all my thesis possess very low Reynolds numbers. Let's, for example, consider a typical situation where a fluid is flowing with velocities of hundreds of $\frac{\mu m}{s}$ in a square channel:

$\rho_{H_2O}\,[\frac{g}{cm^3}]$	$\eta_{H_2O}\,[mPa \cdot s]$	$V_0\,[\frac{\mu m}{s}]$	$L_0\,[\mu m]$
1	0.89	10^2	10^2

$$Re \simeq 10^{-3}$$

This shows that there is no need to worry about turbulences inside our systems, and that it is justified to use the assumption of Poiseuille flow, that I shall apply in order to understand the shape of velocity profiles inside planes normal to flow direction.

2.5.2 Poiseuille flow in rectangular channels

Usually I've employed a rectangular geometry for channels design: it's easier to obtain both during design and fabrication process, but another important reason, remembering SPIM geometry, consists in the fact that plane walls, perpendicular to optical axes, reduce aberrations and artefacts in the imaging process. I find it's worth to dive a little deeper to get a more

precise description of the distribution of the velocity field that will be in particular measured in Chapter 4.
The system under investigation will be a pressure-driven, steady-state flow, at low Reynolds number, also known as Poiseuille flow. Surprisingly enough, there is no analytical solution known with this geometry, in spite of its high symmetry. Assuming width larger than height ($w > h$), Navier-Stokes (in the low Reynolds number case) and no-slip boundary conditions, in a Cartesian reference frame, are:

$$[\partial_y^2 + \partial_z^2] v_x(y,z) = \frac{-\Delta p}{\eta L}, \; for \; -\frac{w}{2} < y < \frac{w}{2}, \; 0 < z < h \tag{2.53}$$

$$v_x(y,z) = 0, \quad for \; y = \pm\frac{w}{2} \; or \; z = 0, \; h \tag{2.54}$$

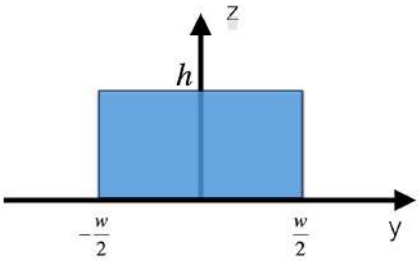

Figure 2.28: Square channel geometry

First step to solve the equation is to expand in Fourier

Series both left and right hand sides, along the (shorter) z direction; to fulfil the boundary conditions, only terms proportional to $sin\left(n\pi\frac{z}{h}\right)$ are employed:

$$[\partial_y^2 + \partial_z^2]v_x(y,z) = \sum_{n=1}^{\infty}\left[f_n''(y) - \frac{n^2\pi^2}{h^2}f_n\right] sin\left(n\pi\frac{z}{h}\right) \quad (2.55)$$

$$\frac{-\Delta p}{\eta L} = \frac{-\Delta p}{\eta L}\frac{4}{\pi}\left[\sum_{n,\,odd}^{\infty}\frac{1}{n}sin\left(n\pi\frac{z}{h}\right)\right] \quad (2.56)$$

For all values of n, the *n-th* coefficient in the pressure term Eq. (2.54) must equal the nth coefficient in the velocity term Eq. (2.55):

$$f_n(y) = 0\,, \quad \text{for } n \text{ even} \quad (2.57)$$

$$f_n''(y) - \frac{n^2\pi^2}{h^2}f_n = \frac{-\Delta p}{\eta L}\frac{4}{\pi}\frac{1}{n}\,, \text{ for } n \text{ odd} \quad (2.58)$$

The solution of the second order differential equation, that also satisfies the boundary conditions, is then easily found:

$$f_n(y) = \frac{4h^2}{\pi^3}\frac{\Delta p}{\eta L}\frac{1}{n^3}\left[1 - \frac{cosh\left(n\pi\frac{y}{h}\right)}{cosh\left(n\pi\frac{w}{2h}\right)}\right] \quad (2.59)$$

Finally giving the velocity profile:

$$v_x(y,z) = \frac{4h^2}{\pi^3}\frac{\Delta p}{\eta L}\sum_{n,odd}^{\infty}\frac{1}{n^3}\left[1 - \frac{cosh\left(n\pi\frac{y}{h}\right)}{cosh\left(n\pi\frac{w}{2h}\right)}\right] sin\left(n\pi\frac{z}{h}\right) \tag{2.60}$$

This result allows a useful visualization of the velocity field inside any rectangular channel employed in this work, and can serve as an additional way to verify the correct analysis of correlation methods.

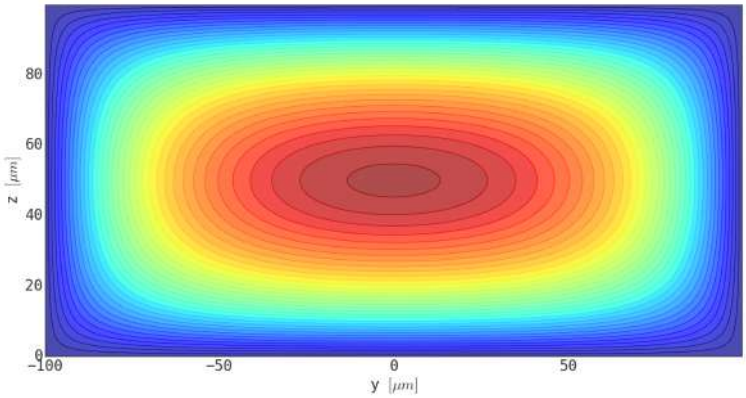

Figure 2.29: Simulation (Python code) of the velocity in a rectangular channel, aspect-ratio = $\frac{1}{2}$. The section shows level curves for the velocity, higher in the centre and decreasing in a $\hat{x}$ and $\hat{y}$ symmetric way towards the boundaries.

2.5.3 Lumped circuit analogy

A very interesting parallelism occurs between current electric circuits and flow in microchannels: elements like resistances, capacitances, or sources find their counterparts in microfluidics and the same laws (e.g Ohm's law) can be employed to model simple networks. The following table summarizes the main useful quantities, with their electronic counterparts:

Electronics	**Microfluidics**
resistance R	hydraulic resistance $R_{hyd} = \frac{\eta L}{A^2}$
capacitance C	compliance $C_{hyd} = -\frac{dV}{dp}$
voltage source ΔV	pressure source Δp
Ohm's law $\Delta V = R\,I$	$\Delta p = R_{hyd}\,Q$

These analogies can help describing, at first approximation, many in-vitro arrangements: for example, let's consider the microfluidic setup employed during the measurements described later in Chapter 4.

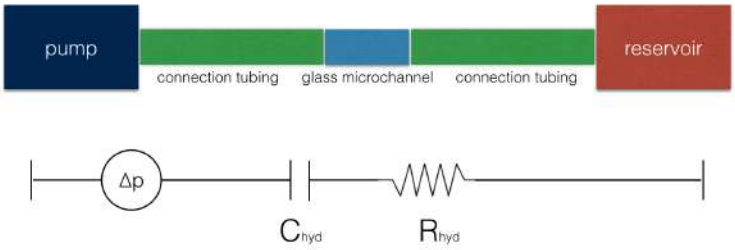

Figure 2.30: Circuital flow scheme

Flow is studied inside the glass microchannel ($800\mu m$ section) and the connections with pump and reservoir are made with Teflon and plastic tubing, which, being elastic, contribute with their compliance to create an equivalent RC circuit. The overall effect can be clearly seen in Figure 2-C of Chapter 4 (reported here for convenience).

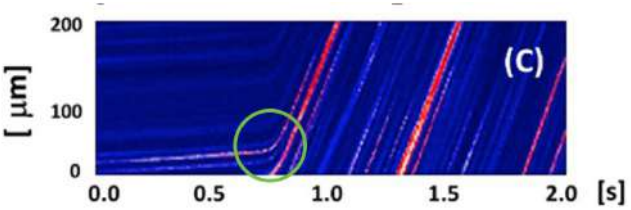

Figure 2.31: Multiple regimes and low-pass filter

This is a synthetic $\{y - t\}$ image, obtained by reporting the same line ($200\mu m$) measured along the flow ($\hat{y}$ direction) as a function of time. This offers a simple way to qualitatively analyse multiple flow components along the same direction with speeds varying over time.

Particles trajectories inside the glass microchannel are shown with bright red lines. The pump produces a square pressure function between 2 regimes, i.e. theoretical abrupt transitions between different trajectories: the experimental smooth transition highlighted with a green circle is then perfectly consistent with the presence of hydraulic compliance and the overall low-pass hydrauilic filter in the model. Besides, being a very fast transition (the connection were specifically chosen the most rigid possible), it will not actually affect the correct sampling of multiple flow regimes.

Chapter 3

Methods

It is the weight, not numbers of experiments that is to be regarded.
Isaac Newton

3.1 PDMS microchannels

Nowadays it has become frequent to talk about Lab-on-a-Chip systems, that is, as the name suggests, little (typical maximum extension of centimetres) platforms designed to perform tests and analysis in an extremely compact way: once loaded with a sample, they should perform all their tasks without other external help, nonetheless giving easy access to all desired data (e.g. fluorescence or other signals collected by embedded or

external detectors,[24,25] or retrieval of products of chemical or mechanical manipulations[26,27]). It's just the equivalent of a miniaturized, automated lab, carried on the palm of a hand. For the in-vitro study of variable flow regimes, I fabricated channels of few hundreds micrometers with complex geometries, and I decided to achieve easy reproducibility and low fabrication cost: the perfect solution was to employ PDMS lithography and 3D printing technology.

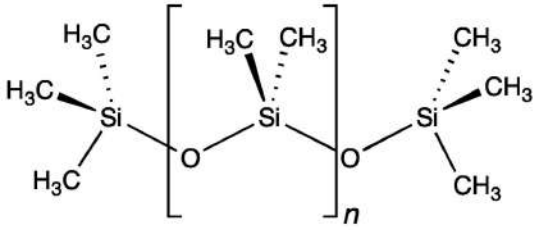

Figure 3.1: PDMS chemical structure

Figure 3.2: Sylgard 184 silicone elastomer consisting of 0.1 L curing agent and 1 L base

PDMS (Polydimethylsiloxane) belongs to a group of polymeric organosilicon compounds, optically clear, inert, non-toxic, and non-flammable:[28] all these properties are perfect when handling solutions of fluorescent beads, that should be imaged with a SPIM microscope. Moreover PDMS is cheap and employing a soft-lithography process based on 3D printed templates results in a fast, low-cost, and high resolution (minimum feature of $20 - 50\mu m$) fabrication procedure.

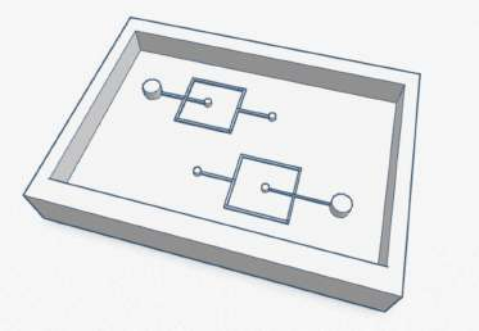

Figure 3.3: 3D printed template example, designed with $Tinkercad^{TM}$

Fabrication process Molding templates are designed with an open-source CAD software www.tinkercad.com: starting with basic geometric structures (cubes, sphere or cylinders as building blocks) I designed all the needed microchannels, with dimensions ranging from $100\mu m$ to $800\mu m$, printed on an average total area of $5\,cm^2$. Templates are printed via stereolithography (SLA), an additive manufacturing technology that converts liquid resins into solid parts, layer by layer, by selectively curing them using a UV laser in a process called photopolymerization.

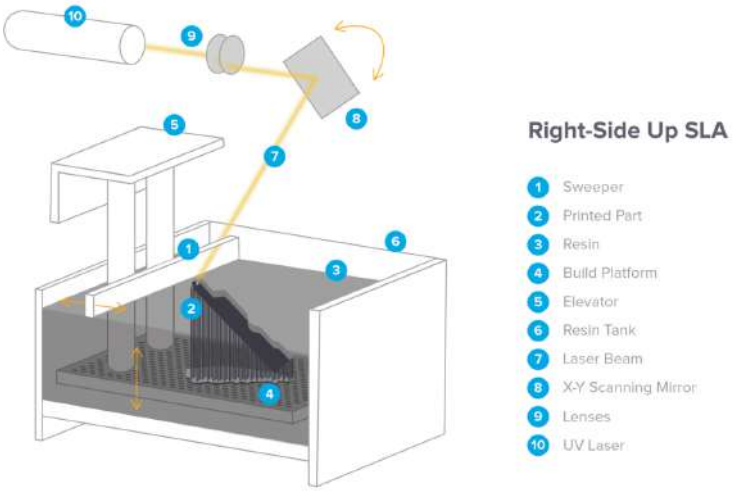

Figure 3.4: Schematic of SLA printer, from *www.formlabs.com*

Printing process has been performed with a Formlab $Form2^{TM}$: it's a laser based printer with a 250mW precision laser guided by custom-built galvanometers, capable of achieving a build volume of $145 \times 145 \times 175\ mm$ with a minimum layer thickness of $25\ \mu m$. Once a template has been produced, it is filled with a 10:1 mixture of PDMS prepolymer and curing agent (figure 3.2), then put in a vacuum chamber for at least 20 minutes (it's a very viscous material and during mixing usually many air bubbles are trapped inside): this allows to obtain a more

resistant chip, as well as one with better optical clarity. In order to further improve transparency on a side of the chip (that is, on the optical window that should be used by SPIM sheet of light excitation to reach the microchannels), I found out that it is better to stick (with silicone grease) a microscopy thin glass on the chosen side of the printed template: in this way it's easy to obtain an extremely smooth surface, avoiding or minimizing unwanted artefacts in the SPIM excitation path.

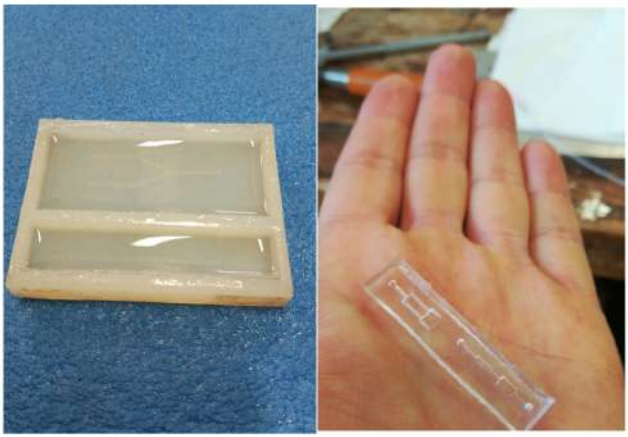

Figure 3.5: Left: 3D printed template filled with (already cured) PDMS. Right: microchannels example.

The next step is heat curing: in order to harden the struc-

ture, the mold is placed in oven for at least 2 hours at 70°C (temperature and time can depend on the actual volume employed). Then peeling off the PDMS structure results in transparent microchannels structure, in which I pierce inlets and outlets to connect flow pumps or reservoirs. The last, maybe most crucial step, is bonding the PDMS with a microscopy glass substrate, in order to obtain a perfect window for imaging. I tried different bonding procedures, and the most effective resulted from employing a thin layer of polydimethylsiloxane prepolymer, spin-coated on a glass slide, transferred onto the embossed area surfaces of the substrate,[29] then put on a new, clean glass slide (figure 3.6), finally heat curing for 30 minutes at 60°C.

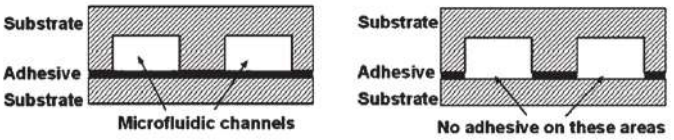

Figure 3.6: PDMS bonding procedure: a thin prepolymer layer is spin-coated on a glass substrate, so that the transfer on PDMS microchannel structures allows adhesion on a new glass slide, leaving open channels.

3.2 Giant Unilamellar Vesicles - GUVs

Giant Unilamellar Vesicles are phospholipids vesicles (artificial liposomes) with average diameters of tens of μm, often employed as a controllable system to study membranes properties or as drug carriers: the development of even larger vesicles to retain cells inside is a promising approach in creating cellular bioreactors that mimic cellular and tissue responses.[30]
I have employed GUVs in particular during the experiments described in Chapter 4, with the main goal of moving towards the analysis of extended physical bodies, beyond the approximation of fluorescent particles as material points.
This approach allows to move one step closer to in-vivo applications (since GUVs are mimicking the behaviour of cells) and also to test correlation methods working with complex structures, opening a future line of study on flow induced mixing in micro-containers.

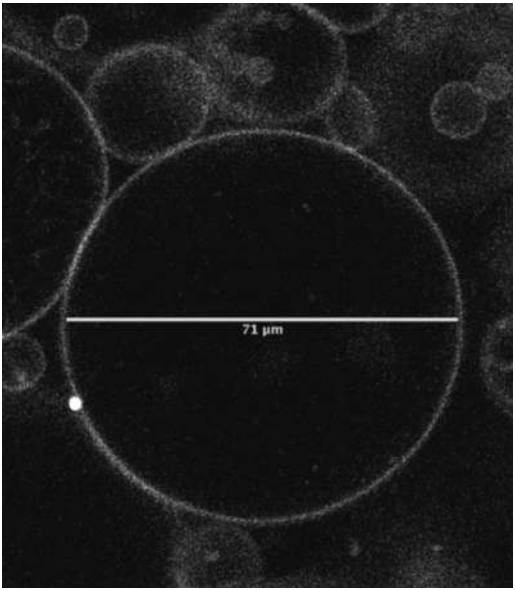

Figure 3.7: An image of GUVs acquired with a confocal microscope (Leica)

Synthesis Guv synthesis has been carried out via electroformation.[31] This process is easy to perform with basic equipment, reliable, and allows production of high concentration solutions of polydisperse lipososmes. The protocol is summarized in the following:

- lipids employed are DOPC (1,2-dioleoyl-sn-glycero-3-phosphocholine) doped with 1 mol % of the fluorescent probe

rhodamine (1,2-dipalmitoyl-sn-glycero-3-phosphoethanolamine-N-lissamine rhodamine B sulfonyl; Avanti Polar Lipids);

- 20 μL of lipid solution ($2\frac{mg}{ml}$ of lipids dissolved in chloroform) is spread on each one of two indium thin oxide (ITO) glass slides;
- slides are dried for 30 minutes under vacuum;
- coated surfaces are spaced by a teflon spacer (2mm): this makes a closed chamber, filled with $200mM$ sucrose solution;
- electric field applied in the chamber in two steps: 15 minutes at $\Delta V = 1.0V$ followed by $3.5 - 4hours at \Delta V = 1.5V$ (10 Hz harmonic signal);
- the vesicles solution is removed from the chamber and diluted in a $200mM$ sucrose solution to reduce vesicles buoyancy.

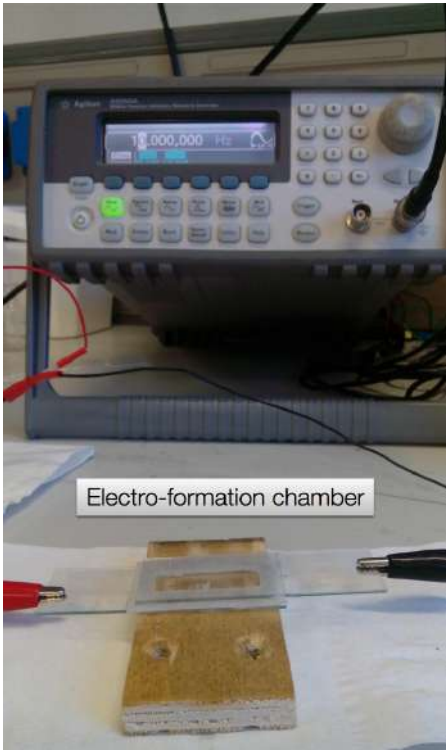

Figure 3.8: GUV synthesis chamber.

3.3 Zebrafish embryos

After in-vitro validation, moving towards a biological sample comes as a natural step: I pursued the the main goal of precisely mapping blood flow in both principal vessels and in peripheral capillaries. The best model organism for this task is the Zebrafish (*Danio Rerio*): it is widely employed in developmental biology[32](e.g. its hearth at 1 day post fertilization (d.p.f.) has similar behaviour to human hearth after 3 weeks gestation), and in the investigation of function and pathologies of the cardiovascular system.[33,34] There is also another very important, practical reason that makes it extremely convenient: an image is worth more than a thousand words in this case, see for example figure 3.9:

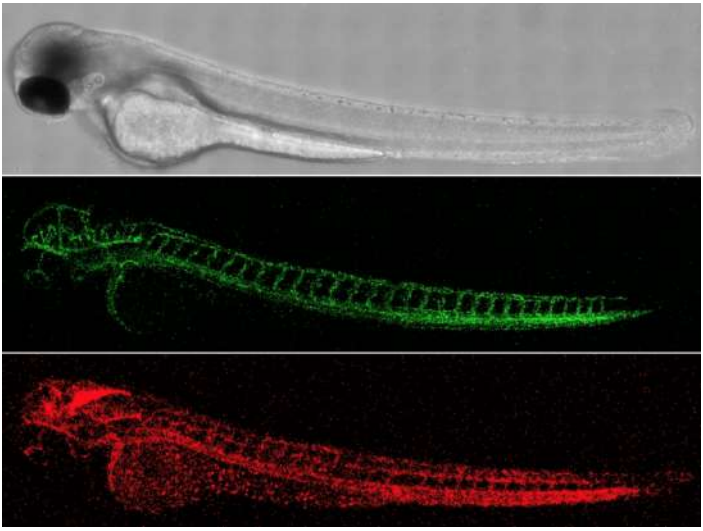

Figure 3.9: Non-confocal transmitted light image (top) and confocal fluorescence images acquired by detecting the signal of Green Fluorescent Protein (GFP) expressed by the endothelial cells (center, $\lambda_{exc} = 488\,nm$) and the signal of DsRed fluorescent protein expressed by red blood cells (bottom, $\lambda_{exc} = 561\,nm$)

The figure shows two fluorescence images of a whole Zebrafish embryo obtained with a confocal microscope, and a bright-field image, obtained with a transmission microscope: the variety of Zebrafish employed is called Casper, because it is a mutant which can't express any pigmentation in the epithelial tissue. Also, it is transgenic in the red blood cells,

which express the fluorophore DsRed ($\lambda_{exc} = 561\ nm$), and in the endothelial cells of blood vessels, which express a GFP ($\lambda_{exc} = 488\ nm$). This means, from a practical point of view, that it's easy both to select what a user desires to image (changing excitation wavelength and detection filters, look at figure 3.10) and to obtain, in every situation, a clearer signal, without worrying about absorbing epithelial structures.

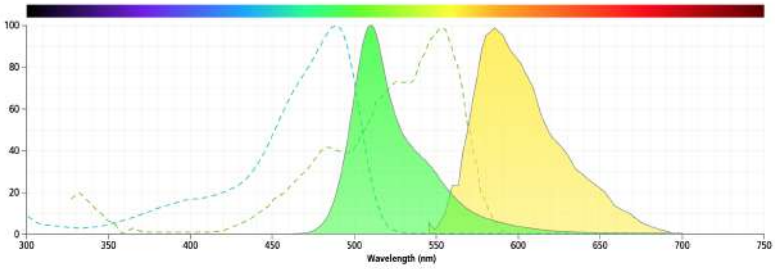

Figure 3.10: Excitation and emission spectra of employed dyes: dashed blue = GFP excitation; dashed green = DsRed excitation; filled green = GFP emission; filled yellow = DsRed emission. (*www.bdbiosciences.com)*

Hemodynamics My main goal has been to map and characterize hemodynamics inside the Zebrafish embryo. There are two basic structures that I have been investigating and that are easily identified in embryos form 3 to 5 d.p.f. (days post

fertilization):

1. main vessels: Dorsal Aorta (DA) and the Posterior Cardinal Vein (PCV), fully formed at two d.p.f., with typical diameter around 20-30 μm: the cardiac contractions promote the blood flow through the arterial vessel, which turns 180° at its caudal end to empty into the cardinal vein, then back to the heart;

2. intersomitic vessels: these are smaller vessels (their diameter reduces to $10\,\mu m$, almost equal in size with the red blood cells (radius of $\pm 4\,\mu m$ and a thickness of $\pm 1 - 2\,\mu m$), developing between 2 and 3 d.p.f., that form throughout the specimen length and interconnect to form the Dorsal Longitudinal Anastomotic Vessels.

Blood flow inside DA is pulsed, with a systolic phase (higher speed, given by hearth contraction) followed by a diastolic phase. Chapter 4 deals precisely with the study of these flows, defining a coherent framework in which quantitative measurement of time varying and pulsed flows (both for in-vitro and in-vivo systems) can be carried out.

Sample handling I employed the SPIM system described in section 2.3 to study Zebrafish embryos: samples are put inside

the observation chamber and with a 3D positioning system it is possible to select the desired region of interest (ROI). In order to keep the samples alive and in good health conditions, I tested two main approaches: :

1. embryos were anaesthetized in 40 $\frac{mg}{l}$ tricaine (Ethyl 3-aminobenzene methansulfonate, Sigma-Aldrich, USA) and then embedded in 1.5% low-melting agarose (Sigma Aldrich, USA), inside a glass capillaary of 800μm internal diameter;

2. samples were inserted in a small FEP (Fluorinated Ethylene Propylene) tubing (internaldiameter 500 μm), and mechanically stopped inside, simply trapping a small air bubble at the tip of the FEP channel (see figure 3.11). I think that this method is way better, both because embryos are not anaesthetized (allowing the study of *less perturbed biological* conditions) and also because FEP tubings are optically more transparent (they offer a better index matching with water) than glass ones.

Figure 3.11: Zebrafish embryo immobilized in FEP tubing - schematics.

Chapter 4

Image Cross-Correlation Analysis of Time Varying Flows

Luck is what happens when preparation meets opportunity.

Seneca

Here I present the first article included in this thesis (pusblished on Analytical Chemistry), focused on the study of time-varying flows: it is primarily thought as an in-vitro study of

model systems simulating hemodynamics. Both flow regimes and sample conditions are extensively explored, in particular:

- different flow regimes (e.g. also investigating alternate flow regimes, where direction of flow was periodically inverted), covering a wide range of velocities (from tens to several hundreds of $\frac{\mu m}{s}$), below and way beyond biological conditions : this serves both as *stress test* and as calibration of the setup and the methods;

- starting from fluorescent particles (rigid micro-spheres of radii from 1 to 5 μm) and moving towards the application to small organisms, the study also explores the impact of more complex tracers, that is GUV (with radii ranging from 5 to 60 μm) possessing internal degrees of freedom and with dimensions comparable with cells;

- finally sFCS is applied to the study of the hemodynamics of the Zebrafish embryos. In particular the systolic and dyastolic phases in the principal artery were successfully characterized.

This work shows that sFCS is a strong and reliable method, especially when combined with Light Sheet microscopy, and capable to tackle properly future extensive in-vivo studies. The employment of extended tracers represents not only a

useful test, but also the start of currently pursued new line of work not included in this thesis, that is the study of the complex mixing motions internally developing in unilamellar vesicles under the action of an external flow.

Image Cross-Correlation Analysis of time varying flows.

Cassia A. Marquezin[1,3], Nicolò G. Ceffa[1], Franco Cotelli[2], Maddalena Collini[1], Laura Sironi[1], Giuseppe Chirico[1,*]

1: Dipartimento di Fisica e Centro di Nanomedicina, Università di Milano-Bicocca, Piazza della Scienza 3, 20126, Milano (I)

2: Dipartimento di Bioscienze, Università di Milano, Via Celoria 26, I-20133, Milano (I)

3: Instituto de Física - Universidade Federal de Goiás - Goiânia - Brasil

Abstract.

In vivo studies of blood circulation pathologies have great medical relevance and need methods for the characterization of time varying flows at high spatial and time resolution in small animal models. We test here the efficacy of the combination of image correlation techniques and Single Plane Illumination Microscopy (SPIM) in characterizing time varying flows in-vitro and in-vivo. As indicated by numerical simulations and by in-vitro experiments on straight capillaries, the complex analytical form of the Cross-correlation function for SPIM detection can be simplified, in conditions of interest for hemodynamics, to a superposition of Gaussian components, easily amenable to the analysis of variable flows. The possibility to select a wide field of view with a good spatial resolution along the collection optical axis and to compute the cross-correlation between regions of interest at varying distance on a single time stack of images, allows to single out periodic flow components from spurious peaks on the Cross-correlation functions and to infer the duration of each flow component. We apply this cross-correlation analysis to the blood flow in Zebrafish embryos at 4 days after fertilization, measuring the average speed and the duration of the systolic and diastolic phases.

*: Corresponding author, Giuseppe.chirico@unimib.it

Keywords: Single plane illumination microscoscopy, image correlation microscopy, fluido-dynamics, microfluidics.

INTRODUCTION.

Space and time mapping of blood flow is essential for biomedical research and for diagnosis of diseases that affect directly the blood circulation system[1] or cause an impaired blood supply to organs. Even in extremely simplified animal models, such as Zebrafish embryos[2] and juvenile transparent fishes,[3,4] the blood circulation presents pulsatile, occasionally irregular, flow with vessel branching that requires high spatial and time resolution to be studied. Blood flow is also severely affected in many tumors and other diseases[5] such as hepatitis B and plays an active role in the immune reaction to viruses. [6] All these examples display time and space complexity and could be studied only by a wide field non-invasive technique with capillary size spatial resolution. Magnetic Resonance Imaging,[7] Optical Coherence Tomography,[8] Doppler Tomography,[9] and Ultrasound Imaging,[1,10] are suitable for whole body studies in small animal models. However they do not offer the high spatial resolution that is instead possible to reach by means of multiphoton optical microscopy.[11,12]

Fluorescence Correlation Spectroscopy (FCS) is a sensitive and non-invasive technique for the study of the molecular and cellular biology dynamics in-vitro and in-vivo.[13,14,15] It has been applied to the measurement of the diffusion coefficient of fluorescent molecules down to pico- and nano-molar concentrations,[16] to the estimate of chemical kinetic constants[17] and to measure flow speeds in micro-channels.[2] The measurement of the Fluorescence Cross-Correlation Functions (CCFs) of the signals from two volumes, also coupled to the use of pixelated detectors (EM-CCD),[2,22] has improved[18-21] the efficacy of FCS for the study of flows. FCS has been also coupled to plane illumination, such as Total Internal Reflection and Single Plane Illumination Microscopy,[22] for the study of complex *stationary* flow fields. Different image correlation techniques[14] allow to study slow (spatiotemporal image correlation spectroscopy)[23,24] or fast molecular dynamics (raster image correlation spectroscopy).[25]

These techniques are however limited in time resolution since correlations should be computed over hundreds of frames due to the low fluctuations arising from the molecular motion.[26] For flowing tracers with high contrast with respect to the background, this requirement can be relaxed as in the recently developed FLow Image Correlation Spectroscopy[6] technique. In this case the flow information is gained from a single raster scanned image and the time resolutions ≅0.5-1 s allows to follow nonstationary flow regimes.

Our aim is to develop a method for the high throughput screening of time dependent flows in vessels over a wide Field Of View (FOV) for applications in-vitro and in-vivo. In order to reach this goal we need a wide field illumination mode coupled to a parallel detection of the signals and to fast data analysis methods to extract the flow speeds. We employ therefore a parallel imaging approach based on the coupling of FCS cross-correlation methods to Selective Plane Illumination Microscopy (SPIM)[27] that allows us to fully characterize the flow regimes off-line by correlative analysis on extended time stacks (120 - 180 sec per stack) with high time resolution (4 ms per frame) and over wide fields (40x250 μm^2). The large FOV (hundreds of microns) allows us to map the flow profile in-vitro (100μm channel, see Supporting Information, SI8) and in-vivo (Zebrafish embryo). Finally, we reduce the complexity of the image analysis by deriving a simplified description of the cross-correlation functions.

We developed therefore a numerical and analytical analysis of the cross-correlation function for the SPIM setup and describe a data analysis method which is tested thoroughly on rigid fluorescent micro-spheres and on labeled Giant Unilamellar Vesicles (GUV), a system that mimics the biological cell. In these in-vitro experiments the programmed values of speeds are retrieved with high accuracy over a wide range of values. Finally we applied SPIM CCF measurements to characterize in-vivo the artery blood flow in Zebrafish embryos.

- THEORY

We follow the fluorescence signal arising from tracers, of size *r* and diffusion coefficient D, in a suspension. The tracer dynamics due to its diffusion, to a drift or even to chemical reactions, produces tiny fluorescence fluctuations that cannot be easily measured. The auto-correlation method brings these fluctuations into evidence by evaluating the self-similarity of the signal in time averaged over a long observation time. From the time evolution of two signals, $I_1(t)$, $I_2(t)$, collected from different Regions of Interests (ROIs) of the system we compute the Cross-Correlation Function CCF, $G^{(1,2)}(\tau) = \langle \delta I_1(t+\tau)\delta I_2(t)\rangle_t / \langle I_1(t)\rangle_t \langle I_2(t)\rangle_t = \langle I_1(t+\tau) I_2(t)\rangle_t / \langle I_1(t)\rangle_t \langle I_2(t)\rangle_t - 1$. The dependence of $G^{(1,2)}(\tau)$ on the lag time τ provides the time of flight of the tracers between the two ROIs (ROI_1 and ROI_2), chosen at the origin and at $\vec{S} = (S_x, S_y, S_z)$, respectively. From this measurement and an appropriate model of the dynamics we can extract the flow speed $\vec{v} = (v_x, v_y, v_z)$. Cross-correlation methods applied on discrete observation volumes or on a set of ROIs on images allow to map the flow field. The analysis of the CCF is however quite involved and it is critically affected by the excitation and collection modes. We couple here CCF methods to a single plane illumination setup in which the light sheet has the width ≅ 6 μm along the collection optical axis and a Rayleigh length (extension perpendicular to the collection optical axis) z_R ≅ 460 μm (see **SI2**). The complexity of the CCF analysis in this setup arises primarily from the need to integrate the signal over the size of the (typically) square ROI of linear size *a*. Our major effort is here to simplify the analysis of the CCFs in order to allow a fast screening of the flow field over extended regions of the sample.

The shape of the Cross-Correlation Function (CCF) measured on a SPIM setup has been derived previously[28,29] and it depends on the flow velocity and the diffusion coefficient of the tracer particles. In many in-vivo studies the tracer diffusion is masked by a number of additional processes: the elasticity of the vessels (for blood circulation) and the finite size of

the tracers (e.g. Red Blood Cells).[2] Here we restrict ourselves to a situation in which drag motions dominate the dynamics (diffusion coefficients ~0.1-0.01 μm²/s, Peclet numbers ~10^3-10^4) and determine the presence of well-defined peaks in the cross-correlation function. We want to focus on systems undergoing laminar flow and to assess to what extent the CCF of the collected signal can be approximated by a simple Gaussian analytical form and this can be used for the analysis of flows with multiple speed regimes.

For SPIM optics, the analytical form of the CCF must take into account the integration of the signal over the (square) ROI on the pixelated detector[30] and over the width of the illumination sheet:

$$\begin{cases} G^{(1,2)}_{SPIM}(\tau) & \propto & G_{z,SPIM}(\tau; v_z, w_z, S_z) G_{xy,SPIM}(\tau; v_x, a, w_{xy}, S_x) G_{xy,SPIM}(\tau; v_y, a, w_{xy}, S_y) \\ G_{xy,SPIM}(\tau; v_k, a, w_{xy}, S) & = & F(a+S-v_k\tau,\tau) - 2F(v_k\tau - S,\tau) + F(a-S+v_k\tau,\tau) \\ F(s-v\tau,\tau) & = & (s-v\tau)Erf\left[(s-v\tau)/M_{xy}(\tau)\right] + \frac{M_{xy}(\tau)}{\sqrt{\pi}} \exp\left[-(s-v_x\tau)^2/M_{xy}(\tau)\right] \\ G_{z,SPIM}(\tau; v_z, w_z, S_z) & = & \frac{\exp\left[-|v_z\tau - S_z|^2/M_z^2(\tau)\right]}{M_z(\tau)} \\ M_z^2(\tau) & = & \left(4D\tau + w_z^2\right) \\ M_{xy}^2(\tau) & = & \left(4D\tau + w_{xy}^2\right) \end{cases} \quad (1)$$

In **Eq. 1** $v_k = v_x$ or v_y, w_{xy} and w_z are the size of the Point Spread Function in the collection path. The $Erf()$ function is the Error Function. Despite the complexity of the analytical form in **Eq.1**, the correlation function $G^{(1,2)}(\tau) = \langle \delta I_1(t+\tau)\delta I_2(t)\rangle_t$ for combined diffusive and drift motion is dominated[2] by the presence of a maximum at a lag time $\tau \cong |\vec{S}_{xy}|/|v_{xy}|$, where $\vec{S}_{xy}$ are the relative position of ROI_2 with respect to ROI_1 and $\vec{v}_{xy}$ is the flow speed on the illumination plane (formally given by $\vec{v}_{xy} = \vec{v} - \vec{v}_z$, assumed to be collinear with $\vec{S}_{xy}$. If we additionally

choose the SPIM plane as the flow plane (or we assume that $|v_{xy}| >> v_z$), we can approximate the CCF in SPIM collection mode with a much simpler 2D effective model:

$$\begin{cases} G_{2D}^{(1,2)}(\tau) \propto M_D^{-1}(\tau)\exp\left[-\dfrac{\left(\tau-\dfrac{|\vec{S}_{xy}|}{|\vec{v}_{xy}|}\right)^2}{\left(\dfrac{a_{eff}}{|\vec{v}_{xy}|}\right)^2 M_D(\tau)}\right] \\ M_D(\tau) = \left(1+\dfrac{\tau}{\tau_a}\right) \end{cases} \quad (2)$$

In **Eq.2** τ_a is the mean diffusion time, $\tau_a = a_{eff}^2/(4D)$, that is related to the tracer's diffusion coefficient and the effective ROI area, $a_{eff}^2 = w_{xy}^2 + a^2 + r^2$, given by the sum of the ROI linear size (a), the optical resolution (w_{xy}) and the tracer size (r).

As shown in the Supporting Information (SI3) the underestimation of the position of the CCF maximum obtained by employing **Eq.2** instead of **Eq.1** is less than 3% for $|\vec{v}_{xy}| \geq 100$ μm/s in the range 0.1 ≤ D ≤ 10 μm²/s and 5 ≤ $|\vec{S}_{xy}|$ ≤ 60 μm. It rises to 20% only for fast diffusing tracers ($D \cong 10\mu m^2/s$) at small $|\vec{S}_{xy}| \cong$ 10 μm and very low flow speeds, $|\vec{v}_{xy}| \cong$ 10 μm/s (see **Fig.S1-E1**). The agreement between **Eq.1** and **Eq.2** covers also the effective (e^{-1}) width, $\delta\tau_{eff}$, measured on the simulated CCFs as detailed in **Eq. S2**. The effective width measured on the full model $\delta\tau_{eff,SPIM}$ agrees within 25 % with the 2D model, $\delta\tau_{eff,2D}$, for $|\vec{v}_{xy}|$ > 200 μm/s in the range 5 ≤ $|\vec{S}_{xy}|$ ≤ 60 μm and 0.1 ≤ D ≤ 10 μm²/s (**Fig.S1**). The discrepancy increases to 75% for

$\left|\vec{v}_{xy}\right|$ = 100 μm/s and fast diffusing species, D=10 μm²/s (**Fig.S1D**), or for very low speeds, $\left|\vec{v}_{xy}\right|$ = 10 μm/s (**Fig.S1E**). Therefore in the limit of slow diffusion and drift velocities larger than 100 μm/s in the SPIM plane, we can approximate the full analytical form of **Eq.1** by a Gaussian CCF in which the maximum lag time scales as and the width scales as $\delta\tau_{eff} \cong \frac{a_{eff}}{\left|\vec{v}_{xy}\right|}$:

$$\tau_{\max} \cong \left|\vec{s}_{xy}\right| / \left|\vec{v}_{xy}\right| \; \tilde{G}^{(1,2)}\left(\tau; A, \vec{v}_{xy}\right) = A \exp\left[-\frac{\left(\tau - \left|\vec{s}_{xy}\right| / \left|\vec{v}_{xy}\right|\right)^2}{\delta\tau_{eff}^2} \right] \tag{3}$$

We can then reduce the complexity of the analysis for flow regimes with N velocity components by employing **Eq.3**, generalized to:

$$G^{(1,2)}(\tau) = \sum_{i=1}^{N} \tilde{G}^{(1,2)}\left(\tau; A_i, v_{xy,i}\right) \tag{4}$$

As we will prove in the experimental section this approach allows us to investigate time dependent multicomponent flows with speeds as high as $|v_{xy}| \approx 2000$ μm/s and with reduced computational effort with respect to the data analysis based on the full model (**Eq.1**). Apart from the processing time gain, we notice that the higher is the flow speed the less points are available on the CCFs. In this case the use of **Eq. 1** as trial fitting function is critical, unless higher frame rates are used. The maximum measurable speed depends (see **SI, Eq.S1.3**) linearly on the CCD frame rate, here 125 s^{-1}, and on the size of the ROI. The latter, ≅ 6 μm, could not be further increased since it should match the size of the cells to be followed in the blood flow. The frame rate can instead be increased at the expense of the detected signal per pixel, thereby limiting its applicability to heavily stained cells. However, the range of the speeds that can be measured with our setup and its uncertainty ≅ 65 μm/s (see

Supplementary Information SI1) are well suited to characterize the physiological hemodynamics in small animal models.[31]

The EMCCD noise affects mainly the amplitude of the CCFs that scales as $G^{(1,2)}(\tau=0)\cong\left(1+\left\langle B^2\right\rangle/\left\langle S^2\right\rangle\right)$, where $\left\langle B^2\right\rangle$ and $\left\langle S^2\right\rangle$ are the averages of the squared background and signal levels respectively. The typical values are $\sqrt{\left\langle B^2\right\rangle}\cong 5.5$ and $\sqrt{\left\langle S^2\right\rangle}\cong 65$, for the experimental conditions and the samples used here. The correction to the amplitude of the CCFs is typically of the order of 1% or less.

- **EXPERIMENTAL SECTION.**

SPIM setup. The SPIM setup[32] employs an Argon-Krypton laser (Melles Griot), expanded 1:4 and focused into the back aperture of an illumination objective (Olympus 4X, 0.1 N.A.) by a cylindrical lens (f = 50mm). The illumination objective produces a light sheet in the (x, y) focal plane of the detection objective (Olympus, 4X, 0.95 N.A.), mounted at 90° with respect to the illumination objective (see **Fig. 1**). The fluorescence, selected by a band-pass filter, is detected by an EMCCD detector (Cascade II, Photometrics, USA). The maximum acquisition rate was 4 ms/frame, on reduced regions of 40x250 μm^2.

Fluidic setup. The piston (1mm diameter = 2R) of a 500 μL Hamilton micro- syringe is coupled to a linear actuator **(Fig.1-c)** (M227- C863 linear actuator, Phyisk Instrumente, D) to generate arbitrary flow regimes as sum of square waves (speed resolution 50 nm/s). At the transition between different speeds we set the actuator to stop for 10 ms.

The input velocities model is based on a composition of square waves (**Fig.1**) corresponding to either two or more velocity values ($v_{xy,i}$) in the same flow direction (modulated speed) or two velocity values in two opposite direction of flow. The duration of the "on" state for a specific speed component is inversely proportional (**Fig.1**) to the speed value for each

component, $t_i^{(on)} = D / v_{xy,i}$, and corresponds to a constant volumetric flow rate or constant number of tracers through the capillary cross-section.

The microcapillaries are connected to the glass syringes (employed as pump and reservoir) by silicone tubes (1x3 mm). The square borosilicate glass microcapillaries have nominal internal lateral size d = 100 or 300 μm (CM Scientific Ltd, UK). For in-vitro reference studies we used a mixture of fluorescent rigid microspheres of various sizes (maximum diameter = 1 μm) and colors (C14837, Invitrogen, NL).

The computation of the maximum expected speed, $V_{capillary}^{(\max)}$, along the central axis of the capillary was done by assuming a constant volumetric rate, that implies a ratio $\langle V \rangle_{capillary} / \langle V \rangle_{syringe} = \pi R^2 / d^2$ between the average speeds in the syringe and the capillary. Since the ratio between the maximum and the average speed in a square capillary is $V_{capillary}^{(\max)} / \langle V \rangle_{capillary} = \frac{\pi^2}{4}$ (see Supporting Information, SI8), the scaling factor between the actuator average speed and the maximum speed in the capillaries is $V_{capillary}^{(\max)} / \langle V \rangle_{syringe} = \frac{\pi^3 R^2}{4 d^2}$.

This corresponds to a scaling factor ≅197 and ≅21.5 for the capillaries with inner size 100 μm and 300 μm, respectively. The actuator nominal precision, 50 nm/s , is taken here as an estimate of the uncertainty on the speeds values.

Giant Unilamellar Vesicles (GUV). The GUVs were prepared by the electro-formation method.[33] We used DOPC (1,2-dioleoyl-sn-glycero-3-phosphocholine) doped with 1 mol % of the fluorescent probe rhodamine (1,2-dipalmitoyl-sn-glycero-3-phosphoethanolamine-N-lissamine rhodamine B sulfonyl; Avanti Polar Lipids). 20μl of lipid solution (2 mg/ml of lipid dissolved in chloroform) was spread on an indium tin oxide (ITO) covered glass slide which was then dried for 30 minutes under vacuum to remove traces of the organic solvent. The two lipid coated surfaces were then spaced (one facing each other) by a teflon spacer (2mm thick),

forming a closed chamber in which a 200 mM glucose solution was gently introduced. An AC electric field was applied to the chamber in two steps: 15 minutes at ΔV = 1.0 V followed by 3.5 – 4.0 hours at ΔV = 1.5 V (10 Hz harmonic signal). The vesicles solution was then gently removed from the chamber and diluted in a 200 mM sucrose solution to reduce buoyancy. The vesicles are spherical, tense and unilamellar, although some of them stuck together in clusters. The GUV Z-average hydrodynamic radius is $R_H \cong 14$ μm (see Supporting Information, SI4).

Zebrafish embryos. In-vivo measurements were done on Zebrafish embryos (4 days post fertilization, d.p.f.) of the transgenic line mitfa$^{w2/w2}$; roy$^{a9/a9}$; *Tg(kdrl*:EGFP)^{S843}; Tg(gata1:dsRed)^{sd2}, carrying green-labeled epithelium (EGFP) and red-labeled (dsRed) red blood cells.[34] The zebrafish embryos were anesthetized[35] with tricaine [40 mg/L tricaine (Ethyl 3-aminobenzene methansulfonate, Sigma-Aldrich Corporation, St. Louis, Missouri)] and positioned in a 2-mm-diam fluorinated ethylene propylene tube (FT2X3, Adtech Polymer Engineering, Frampton Mansell, UK) with 1.5% low melting point agarose and then immersed in a water cell.[36]

- RESULTS AND DISCUSSION

We first collected time lapse stacks of SPIM images of fluorescent probes suspensions flowing in borosilicate glass capillaries. We investigated steady, modulated and alternated flows (**Fig.1C**). The CCF analysis protocol developed on these samples was then applied to in vivo imaging of the blood circulation in Zebrafish embryos.

Carpet Images. A first visual analysis of the flow was based on a synthetic x-t image (carpet image, **Fig.2**) obtained by reporting the same line (250 μm x 2 μm in this case) measured along the flow (x direction) as a function of time (500 frames, see sketch D in **Fig.2**). This

offers a simple way to qualitatively analyze multiple flow components along the same direction with speeds varying in time.

Fig.2 shows the trajectories of the tracers travelling along the selected line that appear as slanted bright stripes over a uniform background. Straight bright lines indicate stretches of uniform motion whose speed is directly related to their slopes in the carpet image. Modulated regimes with speeds alternating between two values, v_1 and v_2, in the same direction and orientation, result in carpet images (**Fig.2A**) in which the two sets of stripes appear with different slopes. Due to the compliance of tubing the actual flow orientation inverts, for alternating regimes, in about 1s during which the bright lines are parallel to the carpet time axis (**Fig. 2B**). An example of this transition is reported in **Fig.2C**, where the compliance of the silicon tubing connections at high flow speed in a small cross-section capillary (300 μm) results in curved bright lines. The carpet images offer therefore a direct visualization of the complexity of the time evolution of the flow but are not easily amenable to an automatic computation of the speed values, particularly in the case of non-uniform motion.

Cross-correlation analysis in vitro. We focus here on the case of a time varying uniaxial flow in which the velocity amplitude changes between two or three values and may invert the direction of motion. We measured the speed for each of the flow components by computing the CCFs between two ROIs selected on the SPIM wide field image. The ROI size was of the order of the tracer object in order to detect the signal fluctuations, as displayed in **Fig.3A** for fluorescent microbeads (≅ 1 μm in size) flowing along the central axis of a 100 μm micro-capillary. The comparison to the expected speed values was done by assuming a conversion factor of $V_{capillary}^{(\max)} / \langle V \rangle_{syringe} \cong 197$ between the actuator speed, $\langle V \rangle_{syringe}$, and the speed measured along the capillary axis.

Correlations between fluorescence burst are evident on the bare fluorescence trace: see for example the couples of bursts at time ≈2.6 s and time ≈ 3.25 s in **Fig.3A**. The signal histogram is

very similar for the two ROIs and the fraction that corresponds to the bursts is negligible (≅ 0.4% of values larger than ≈50 kcounts/4 ms, right inset of **Fig.3A**). Nevertheless the cross-correlation functions of these signals display a clear correlation peak, as plotted in **Fig.3B** for increasing distance between the pixels. Two Gaussian components are observed with constant width (**Eq.3**, notice the logarithmic scale on the lag time axis), $\delta\tau_{eff,1} = 16 \pm 2\,\text{ms}$ and $\delta\tau_{eff,2} = 7 \pm 0.8$ ms, independent of the inter-pixel distance. The ratio of the peak maximum lag times for the two components is also constant $\tau_{\max,2} / \tau_{\max,1} = 0.27 \pm 0.005$, and its value agrees well (10%) with the ratio of the maximum speeds set by the actuator, 1450 ± 5 μm/s and 435 ± 5 μm/s (ratio = $\left(\frac{|\vec{v}_{xy,1}|}{|\vec{v}_{xy,2}|}\right) \cong 0.300 \pm 0.005$). The ratio of the width of the two components, $\left(\frac{a_{eff}}{v_{xy,2}}\right) / \left(\frac{a_{eff}}{v_{xy,1}}\right) = 0.43 \pm 0.2$, is slightly larger than the speed ratio, though within the uncertainty of the measurement.

The difference of the amplitudes of the two components of the CCFs is due to their different sampling. Since the duration of each phase is proportional to $1/|\vec{v}_{xy,i}|$ the number of tracers sampled during each flow phase is the same. The amplitude of the CCF components scales therefore only with the number of frames, f_i, which are needed to sample each tracer flowing through the ROI (for $|\vec{v}_{xy,i}| = 400\mu m/s$ and ROI size 6μm, $f_i \cong 4$). Since this number is proportional again to $1/|\vec{v}_{xy,i}|$, the ratio of the maximum amplitude of the Gaussian components scales as the inverse ratio of the corresponding speeds: $\frac{A_2}{A_1} = 0.25 \pm 0.08 \cong \frac{|\vec{v}_{xy,1}|}{|\vec{v}_{xy,2}|} = 0.300 \pm 0.005$.

The linear fit of the peak lag times, $\tau_{\max,i}$, as a function of the pixel-pixel distance $\left|\vec{S}_{xy}\right|$ (20μm ≤ $\left|\vec{S}_{xy}\right|$ ≤ 120μm) provides a more accurate measurement of the speed for the various components (see **Fig.3C**). We measure in this way the values 1426 ± 5 [$\frac{\mu m}{s}$] and 403 ± 5 [$\frac{\mu m}{s}$]. The good agreement with the nominal values, 1450 ± 5 μm/s and 435 ± 5 μm/s, confirms the good approximation of the SPIM CCF analytical with a simple Gaussian function. The systematic error arising from this approximation, which is at most 10% for $\left|\vec{S}_{xy}\right| > 20\mu m$ even for speeds as low as 200 μm/s, decreases rapidly with increasing values of $\left|\vec{S}_{xy}\right|$ and its effect on the overall linear fit is therefore negligible. It should be noticed that this type of multiple analysis over extended fields of view is made possible by the use of SPIM that provides huge amount of data in parallel at high frame rates.

Figure 3D shows the effect on the CCF of the shape of the ROIs. Two square ROIs composed of a 3x3 pixels and two ROIs chosen as 10 pixels lines perpendicular to the flow direction, are compared to the case of two single pixel ROIs. By increasing the size of the ROI from one pixel (**Fig.3D**, circles) to a 3x3 square ROI (**Fig.3D**, down triangles), the visibility ($\tilde{V} = \left[\left(\tilde{G}^{1,2}\right)_{\max} - \left(\tilde{G}^{1,2}\right)_{\min}\right] / \left[\left(\tilde{G}^{1,2}\right)_{\max} + \left(\tilde{G}^{1,2}\right)_{\min}\right]$) of the two Gaussian components in the CCF changes from $\tilde{V} \cong 1$ to $\tilde{V} = 0.8 \pm 0.09$ for the two cases, respectively. We observe $\tilde{V} \cong 1$and a slight decrease of the amplitude of the Gaussian components for the case of two linear ROIs, that does not affect the accuracy of the measurements (**Fig.3D**, up triangles). These observations agree with the simulations of the CCFs for multiple pixels ROIs reported in the Supporting Information (SI9) and indicate that, though single pixels ROIs offer the best visibility of multiple peaks in the CCFs, other geometries could be used depending on the flow symmetry.

The CCF analysis offers also the possibility to gain direct information on the duration of each speed regime for pulsed flows. If we assume that the flow is periodic with two (or more)

regimes with speed values $\left|\vec{v}_{xy,1}\right|$ and $\left|\vec{v}_{xy,2}\right|$, we can compute CCFs on fixed time windows cut periodically along the data set (windowed-CCFs, see SI5). For pulsed regimes of known number of phases we can retrieve their duration within ≅ 4% (see **Fig.S5**) accuracy by finding the window size that produce a CCF characterized by a single peak. Details on this type of analysis can be found in the Supporting Information (**SI5**).

More complex flow regimes can also be studied by SPIM CCF, as in the case of pulsed flow regimes with three or more values of speeds or in alternating regimes (**Fig. 4**). Also in the case of a pulsed regime with three components we are able, by exploiting the possibility to change the inter-pixels distance on the acquired time stack of data, to retrieve all the speed values with an excellent accuracy, < 5 % (see **Fig.4A,B**).

As for alternate regimes, the two speed components are retrieved separately (**Fig.4C,D**) from the forward, $G^{(1,2)}(\tau)$, and backward, $G^{(2,1)}(\tau)$, CCFs computed between the signals collected from two square ROIs (a = 3x3 pixels = 6x6 μm^2) set along the flow direction at increasing distances. In this case the agreement between the experimental and the measured speed values is very good for the forward component (**Table I**, component 1). For the backward component we measure a value ≅30% lower than the set value. However, as reported at the end of the section **SI.8**, the observed discrepancy can be ascribed to the depression induced by capillary forces while retreating the piston backward. In fact, the accuracy in the measurement of the flow speed, as from the data discussed in **Fig.3**, is at least 10%, and we expect no systematic errors in the evaluation of the speed due to our simplified CCF analysis as can be gained from our numerical analysis reported in **SI3**. This observation is in agreement with previous results[2] obtained by conventional dual spot analysis of the flow in a capillary and account for the accuracy of the analysis method proposed here. We further notice that the amplitude and the width of the CCFs components scale as the corresponding speed values and their inverse, respectively, as expected from **Eq.3.**

In the previous examples we have assumed that the flow was occurring in the illumination sheet plane. If $v_z \neq 0$ an additional Gaussian term $G_{z,SPIM}(\tau) \propto \exp\left(-(\tau/\tau_z)^2\right)$ multiplies the CCF (we assume $S_z = 0$). The relaxation time along the z direction, $\tau_z = w_z / v_z$, may span a wide range depending on the value of v_z and it can fall within the lag time window of the CCFs reported in **Figs. 3** and **4**. For example by assuming that $v_z / |\vec{v}| \cong 0.1$ (the flow occurs at about 6 degrees out of the sheet plane) and $|\vec{v}| \cong 1000 \mu m / s$ we estimate $\tau_z \cong 60 ms$. The presence of this additional Gaussian component would skew the shape to the in-plane Gaussian components, $G_{xy,SPIM}(\tau)$. Such deformation would produce an underestimation of the corresponding peak lag times, which we expect to be more pronounced for short ROI-ROI distances. This would correspond to a non-linear dependence of the peak lag times on the ROI-ROI distances, a trend that it is not observed in our data (**Fig. 3C** and **Fig. 4B,D**) indicating that the flow is indeed occurring in the plane of the illumination sheet.

In moving towards the application to small organisms in-vivo, we mimic the case of cells used as tracers by following the flow of GUVs in a 300 μm capillary. These objects have the size of most cells, from a few to tens of micrometers, are polydisperse in size (z_average size = 13 ± 4 μm (see Supporting Information, SI3) and are deformable. It must be noted that (see image in **Fig.5A**) the GUVs are labeled on the lipid membrane and appear rarely as a uniform fluorescent circle due to in-homogenous staining of the membrane (see image in **Fig.5A**). The data reported as an example in **Fig.5** correspond to the case of a flow with two modulated components for which the CCFs were analyzed as a sum of two Gaussian functions (see **Eq.3**). For this sample, the width of the CCFs components is affected by the size of the tracers which is larger than the ROI size (see image in **Fig.5**). Accordingly, we were able to retrieve correctly the flow speeds and the widths from the fit of the CCFs to the simplified **Eq.3** (see **Table I**) by assuming an effective ROI size $a_{eff} \cong r \cong 14$ μm, which is about the average size of the GUVs

(see **Table I** and Supporting Information, SI4). We additionally notice that the existence of a Gaussian component in a single CCF is not a direct hint for a real flow component. In fact the component at lag time $\tau_{max} \approx 100$ μs (for $\left|\vec{s}_{xy}\right|$ = 30 μm; **Fig.5A**, vertical arrow) does not corresponds to a real flow component since it is not retrieved for other values of $\left|\vec{s}_{xy}\right|$ (**Fig.5B**, filled triangle). The origin of this spurious component must be searched in the statistical properties of the signal composed by very few (≅1 bursts/s) and very bright (signal/noise ≅ 30) bursts (**Fig.3A**). With such low counting it is possible that two independent tracers pass through the two ROIs at a distance in time that happen to be close to time of flight between the ROIs. Such a single occurrence may have a substantial weight on the total CCF, and appears as an additional (low amplitude) component. We can single out this occurrence by performing different measurements at increasing ROI-ROI distances, as done here or, alternatively, compute CCFs on subsets of the original data.

Cross-correlation analysis in-vivo. We have applied wide field of view SPIM-CCF analysis to in vivo samples. Time lapse stacks of SPIM images of a Zebrafish embryo (4 d.p.f.) were acquired by following the fluorescent signal from red blood cells expressing DsRed.

The CCFs computed along the artery (see **Fig.6**) show a single wide peak with a substructure that becomes a clear double peaked function as the distance between the ROIs (3x3 pixels) increases. The two speeds correspond to the two phases of the heart pulsation, the systolic and diastolic phases[30] as also found in the literature. The diastolic and systolic speeds are in our experiment 180 ± 9 μm/s and 330 ± 15 μm/s, respectively. These values are in agreement with previously reported ones.[2,37] Again in this case, as for the GUV experiments, the width of the Gaussian components of the CCFs agrees with a tracer size of about 10 μm, close to the size of the red blood cells.[2]

The amplitude of the CCF components are remarkably different (≈ 70%; see **Table I**) for the diastolic and systolic phases. If we assume a rigid vessel, the amplitudes of the CCF components is related to the vessel section *A*, the speed of the tracers, $\left|\vec{v}_{xy}\right|$, the duration Δt of the blood pulsation phase and the average number of frames per tracer passage through the ROI for each phase, f_i:

$$G\left(\tau_{peak,i}\right) \propto A f_i \left|\vec{v}_{xy,i}\right| \Delta t_i \qquad (5)$$

However the number of sampling frames per tracer scales as $1/\left|\vec{v}_{xy,i}\right|$. Therefore the relative change in the amplitude of the CCF components for the systolic, $G(\tau_{syst})$, and diastolic, $G(\tau_{diast})$, phases should be related only to the ratio of the corresponding phase durations:

$$\left(\Delta t_{syst} / \Delta t_{diast}\right) = \left(G\left(\tau_{syst}\right) / G\left(\tau_{diast}\right)\right) \qquad (6)$$

The ratio $\left(\Delta t_{syst} / \Delta t_{diast}\right) = 3 \pm 1$ measured here (see **Table I**) for the embryos at 4 d.p.f. implies that the duration of the systolic phase is three times larger than the diastolic one in embryos. A qualitative confirmation of this conclusion can be gained from the carpet image analysis (see Supporting Information, SI6) of the blood dynamics in the Zebrafish embryo. Two phases are clearly visible in the carpet image reported in **Fig.S6**. Although the discrimination of the two phases is not easy and cannot be drawn quantitatively on this plot, the systolic phase, characterized by less steep stripes in the carpet image, lasts at least 1.5 times more than the diastolic one.

- **CONCLUSIONS**

The characterization performed on model systems in-vitro and applied to animal models in-vivo, indicates that time varying multi-component flows in capillaries and in vessels in animal models can be reliably studied by image cross-correlation spectroscopy coupled to Single Plane Illumination Microscopy with a simplified analysis approach. The use of the simple Gaussian approximation of the CCFs does not limit the application of combined SPIM-CCF methods to the fast screening of complex time dependent flows in microstructures at least for high Peclet numbers. The method tested here allows to accurately determine the number of flow components and their speed values by computing the CCFs at different inter-ROIs distances over an extended field of view. The sensitivity of the CCF methods allows us to compute the CCF over reduced stretches of times and to retrieve the duration of each speed phase for periodic motions and the number of the flowing tracers in each phase. We have applied these measurement and analysis protocols to the characterization heart pulsation (systolic and diastolic phases) in Zebrafish embryos.

- **ACKNOWLEDGMENTS:**

C.A.M. acknowledges the financial support of the Brasilian CNPq (Conselho Nacional de Desenvolvimento Científico e Tecnológico) for her research at the University of Milano-Bicocca. GC acknowledges the funding “Innovation Grant 2014” from Università di Milano-Bicocca. We gratefully acknowledge the help of Matteo Cattaneo in the measurements on Zebrafish embryos.

Supporting Information. The supporting information reports the analysis of resolution of the speed measurements, the SPIM light sheet characterization, the numerical simulation of the SPIM CCFs, the GUV size characterization, the windowed-CCFs analysis, the systolic and

diastolic characterization in Zebrafish embryos, the Python codes description, the microcapillaries flow profile, the effect of the ROI shape on the CCFs and the accuracy of speed measurement from CCF maxima.

TABLES.

Table I: comparison between expected values and best fit parameters for the analysis of the CCFs according to Eq.3.

	Three components, pulsed (6x6 μm² ROI, **Fig.4B**, microbeads)				
	Velocity [μm/s]		Width [ms]		Amplitude
	Measured	Expected	Measured	Expected	
1	273 ± 1	268 ±5	28 ± 1.5	28§	1
2	854 ± 8	860 ±5	8 ± 1	7§	0.12 ± 0.04
3	1462 ± 4	1450 ±5	5.6 ± 1	4.1§	0.09 ± 0.02
	Two components, alternate (6x6 μm² ROI, **Fig.4D**, microbeads)				
1	296 ± 5	300 ±5	35 ± 3	21± 2	0.79± 0.07
2	205 ± 8	300 ±5	46 ± 4	30± 2	1
	Two components, pulsed (2x2 μm² ROI, **Fig.5**, GUV)				
	Velocity [μm/s]		Width [ms]		Amplitude
	Measured	Expected	Measured	Expected	
1	182 ± 24	215 ±5	76 ± 4	74*	1
2	526 ± 4	538 ±5	24 ± 10	25*	0.16 ± 0.07
	Zebrafish embryos (3x3 pixels = 6x6 μm² ROI, **Fig.6**)				
	Velocity [μm/s]		Width [ms]		Amplitude
	Measured		Measured	Expected	$G(\tau_{diast})/G(\tau_{syst})$
1	180 ± 9	--	46 ± 4	55$	1
2	330 ± 15	--	35 ± 3	31$	0.3 ± 0.1

Table I. Best fit parameters obtained from the fitting of the experimental CCFs to **Eq.3**.
*: w_0 = 14 μm is assumed in this theoretical evaluation;
§: w_0 = 6 μm is assumed in this theoretical evaluation;
$: w_0 = 10 μm is assumed in this theoretical evaluation.

- **REFERENCES.**

1. Devore G.R., Falkensammer P., Skanlansky M. S., Platt L. D. *Ultrasound Obstet Gynecol,* **2003**, 22, 380-387.
2. Pozzi P., Sironi L., D'Alfonso L., Bouzin M., Collini M., Chirico G., Pallavicini P., Cotelli F., Foglia E.A. *J. Biomed. Opt.* **2014**,19(6), 067007.
3. White R.M., Sessa A., Burke C., Bowman T., et al. *Cell Stem Cell.* 2008 Feb 7; 2(2): 183–189.
4. Fieramonti L., Foglia E., Malavasi S., D'Andrea C., Valentini G., Cotelli F., Bassi A., **J. Biophot.**, 8 (1-2), 52-57 (2015)
5. Carmeliet, P. *Nat. Med.* **2003**, 9, 653–660
6. Sironi, L., M., Inverso D., D'Alfonso L., Pozzi P., Cotelli F., Guidotti L.G.,Iannacone M., Collini M., Chirico G. *Scientific reports*, **2014**, 4, 7341.
7. Calamante, F., Thomas, D. L., Pell, G. S., Wiersma, J. & Turner R. *J. Cerebr. Blood F. Met.* **1999**, 19, 701–735.
8. Srinivasan, V.J., Sakadžić, S., Gorczynska, I., Ruvinskaya, S., Wu, W., Fujimoto, J.G., Boas, D.A. Opt. Expr. **2010**, 18, 2477–2494.
9. Briers, J. D. *Physiol. Meas.* **2001**, 22, R35–R66.
10. Macé, E., Montaldo, G., Cohen, I., Baulac, M., Fink, M., Tanter, M. *Nat. Methods* **2011**, 8, 662–664.
11. Santisakultarm, T.P., Cornelius, N.R., Nishimura, N., Schafer, A.I., Silver, R.T., Doerschuk, P.C., Olbricht, W.L., Schaffer, C.B. *Am. J. Physiol. Heart. Circ. Physiol.* **2012**, 302, H1367–H1377.
12. Shih, A. Y. Driscoll, J.D., Drew, P.J., Nishimura, N., Schaffer, C.B., Kleinfeld. D.Two-photon microscopy as a tool to study blood flow and neurovascular coupling in the rodent brain. *J. Cerebr. Blood F. Met.* **2012**, 32, 1277–1309.
13. Kim, S. A., Heinze, K. G., Schwille P. *Nat. Meth.* **2007**, 4(11), 963–973.
14. Digman, M. A., Gratton, E. *Ann. Rev. Phys. Chem.* **2011**, 62, 645–668.
15. Elson, E. L. *Biophys. J.* **2011**, 101(12), 2855-2870.
16. Magde, D. , Webb, W. W. , Elson, E.L. *Biopolymers,* **1978,** 17, 361-376.
17. Widengren, J., Rigler, R. *Cell Mol Biol.* **1998**, 44(5), 857-79.
18. Brister, P.C., Kuricheti, K. K., Buschmann, V., Weston, K. D. Lab Chip **2005**, 5 , 785-791.
19. Brinkmeier, K., Doerre, J.S., Eigen, M. *Anal. Chem.* **1999**, 71(3), 609–616.
20. Dertinger T., Pacheco, V, von der Hocht, I., Hartmann, R., Gregor, I., Enderlein, J. *Chem. Phys. Chem.*, **2007**, 8(3), 433–443.
21. Haustein, E., Schwille, P. *Annu. Rev. Biophys. Biomol. Struct.* **2007**, 36:151–69.
22. Sankaran, J., Manna, M., Guo, L., Kraut, R., Wohland, T. *Biophys. J.* **2009**, 97(9), 2630–2639.
23. Kolin, D.L.; Wiseman, P. W. *Cell Biochem. Biophys.* **2007**, 49, 141-164.
24. Hebert, B.; Costantino, S.; Wiseman, P.W. *Biophys. J.* **2005**, 88, 3601-14.
25. Rossow, M.J. , Sasaki, J. M. , Digman, M. A., Gratton, E. *Nature Prot.* **2010**, 5(11), 1761-1774.
26. Travagliati, M., Girardo, S., Pisignano, D., Beltram, F., Cecchini, M. *Anal. Chem.* **2013**, 85 (17), 8080–8084
27. Reynaud, E.G.,Peychl, J., Huisken, J.,Tomancak, P. *Nature Meth.* **2015**, 12:30–34
28. Sankaran, J., Shi, X., Ho, L-Y., Stelzer, E. H. K. , Wohland, T. *Opt. Express*. **2010** 18(25) 25468.
29. Burkhardt, M., Schwille, P. *Opt. Expr.* **2006**, 14(12), 5013-20.

30. Krieger, J.W., Singh, A.P., Bag, N., Garbe, C.S., , T.E., Langowski, J., Wohland, T. *Nat. Prot.* **2015**, 10, 1948–1974.
31. Thiriet, M. ,Parker, K.H. in *Cardiovascular Mathematics*; *Formaggia, L.*, Perktold, K., Quarteroni, A. Springer Verlag: Milano (I), 2009; pp. 1-45.
32. Pitrone, P.G., Schindelin, J., Stuyvenberg, L., Preibisch, S., Weber, M. Eliceiri, K.W., Huisken, J.P. *Nat. Methods* **2013**, 10, 598–599.
33. Angelova, M.I., Dimitrov, D.S., *Faraday Discuss. Chem. Soc*. **1986**, 81, 303-311.
34. Lawson, N. D., Weinstein, B. M. *Dev. Biol.* **2002**, 248(2), 307–318.
35. Akimenko M. A., Johnson, S.L., Westerfield, M., Ekker, M. *Development* **1995**, 121(2), 347–357.
36. Bassi, A., Fieramonti, L., D'Andrea, C., Mione, M., Valentini, G. *J. Biomed. Opt.* **2011**, 16(10): 100502.
37. Denvir, M.A., Tucker, C.S., Mullins, J.J. *BMC Biotechnology* **2008**, 8:21

Figures.

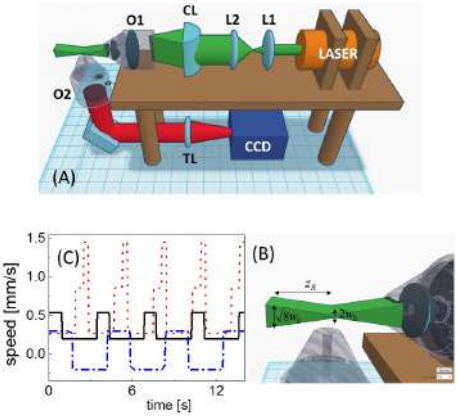

Figure 1. Panel A. SPIM setup. The expanded laser beam (beam expander, L1 and L2 lenses) is focused at the entrance pupil of the objective (O1) by a cylindrical lens (CL). The light is collected at right angle by a second objective (O2) and focused on the CCD camera by the tube lens (TL). Panel B: Schematics of the excitation profile defining the sheet width $w_z \cong 6$ μm and the Rayleigh range, $z_R \simeq 460$μm, which is approximately one half of the maximum extent of the FOV (≈ 250μm) of the CCD chip. Panel C. Typical speed profile acted on the microfluidic setup. The three cases correspond to the cases of a two (black solid line) or a three speeds (red dotted line) modulated regime and of an alternate (blue dot-dashed line) flow regime.

320

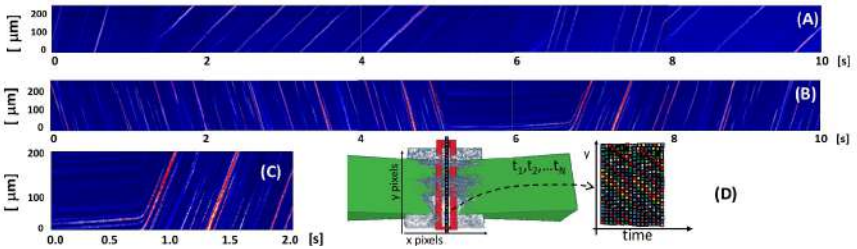

Figure 2: Carpet images for pulsed and alternate flow regimes for fluorescent microbeads in a 300µm capillary. **Panel A.** pulsed time profile with speed values $v_1 \cong 330$ µm/s and $v_2 \cong 1450$ µm/s. **Panel B.** Alternate time profile, $v_1 \cong$ -940 µm/s (backward) and $v_2 \cong +1350$ µm/s (forward). **Panel C**: Blow-up of the transition, lasting approximately 1 s between positive and negative velocity. **Panel D**: carpet image building up. The image is shown in gray embedded in the laser sheet (green). A line of interest is chosen along the blood flow in a vessel (in red). This line is collected for increasing times (t_1, t_2, ..t_N) and used to synthesize an y-t carpet image.

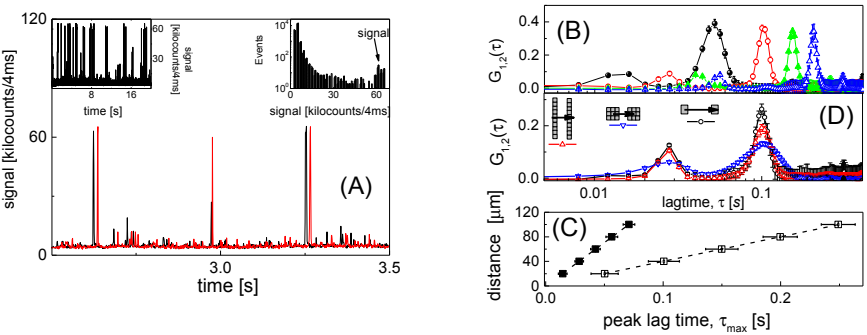

Figure 3: Analysis of two components pulsed flows: rigid fluorescent microspheres flowing in a straight 100µm glass square capillary. Panel A: excerpt of the time trace of the signal collected from to 2 single pixels along the flow (black and red lines refer to up-stream and down-stream pixel, respectively). The speeds were $v_1 \approx 1416$ and $v_2 \approx 425$ µm/s. Left inset: full trace for the up-stream pixel. Right inset: histogram of the fluorescence signal (down-stream pixel). Panel B: CCFs between two single pixels for increasing distances, $\left|\vec{S}_{xy}\right|$= 20 (black circles), 40 (open red circles), 60 (green up triangles) and 80 µm (blue empty up triangles). Panel C: peak lag time, $\tau_{\max}$, corresponding to the CCF maxima as a function of the ROI-ROI distance $\left|\vec{S}_{xy}\right|$. The dashed lines are the best linear fit ($\left|\vec{v}_{xy,i}\right| = \left|\vec{S}_{xy}\right| / \tau_{\max,i}$) to the data as measured in panel B. The best fit slopes (speed values) are $v_1 = 400 \pm 3$µm/s and $v_2 = 1410 \pm 10$µm/s. Panel D: CCFs computed on ROIs with different shapes and sizes, single pixels (black circles), 3x3 rectangles (blue down triangles) and lines (red up triangles).

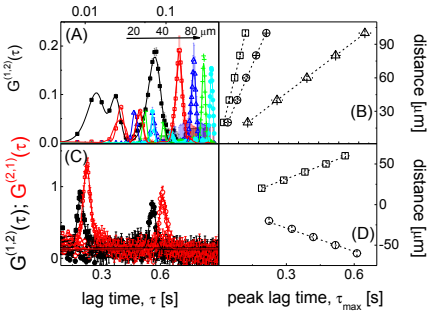

Figure 4. Complex time regimes. Panel A: CCFs measured for the case of a three components modulated flow (microbeads in a 300 µm capillary, single pixel ROIs). Panel B: peak lag times of the components retrieved by best fitting to **Eq.3** the CCFs reported in panel A. Panel C: forward, $G^{(1,2)}(\tau)$ (black filled symbols) and backward, $G^{(2,1)}(\tau)$ (red open symbols) CCFs computed for micro-beads undergoing an alternate flow in a 100 µm capillary ($\left|\vec{S}_{xy}\right|$=20µm, squares; $\left|\vec{S}_{xy}\right|$= 60µm, circles). Panel D: peak lag times of the components retrieved by best fitting the measured CCFs to **Eq.3**, plotted as a function of the $\left|\vec{S}_{xy}\right|$ distance. The best linear fit (dashed lines) of the data reported in panels B and D provide the flow speeds.

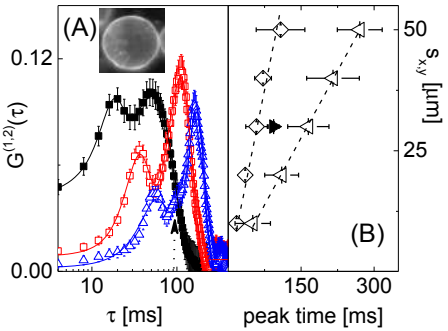

Figure 5. CCFs measured from a suspension of GUV in a 300 μm capillary. Panel A: example CCFs measured at inter-pixel distances $\left|\vec{S}_{xy}\right|$ = 10(black squares), 20 (red open circles)and 30 μm (blue up triangles). The solid line are the best fit to **Eq. 2** with 2 ($\left|\vec{S}_{xy}\right|$=10, 30 μm) or 3 ($\left|\vec{S}_{xy}\right|$=30μm, see vertical arrow) components. The image shown in the inset is the fluorescence emission collected in SPIM configuration from a GUV. The full field size is 25 μm. Panel B: linear trend of the best fit peak lag times as a function of the inter-pixel distance. The dashed line are the best fit lines to the data. The solid symbol refer to a third component retrieved by the fit at $\left|\vec{S}_{xy}\right|$=30 μm.

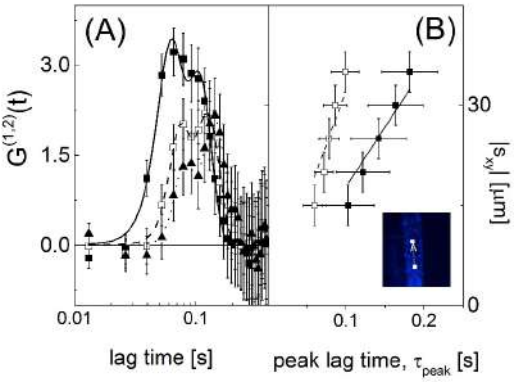

Figure 6. CCFs acquire on Zebrafish embryo arthery. Panel A reports the CCFs measured between rectangular ROIs (3x3 pixels = 6x6 μm²) at distances $\left|\vec{S}_{xy}\right|$ = 20, 25 and 30 μm. Panel B: the inset image shows a field of view (linear size = 6 μm) of the Zebrafish embryo with an outline of the ROIs and an arrow that indicates the average flow direction. The symbols in the main panel B are the best fit peak lag-times of the Gaussian analysis of the CCFs. The solid lines are the best linear fit to the data leading to the following speed values: v_1 = 180 ± 9 μm/s and v_2 = 330 ± 15 μm/s.

4.1 Spotlight

I want to highlight, as a closure, what I think are important observations, that encompass more subtle points, not extensively discussed in the article, but nonetheless crucial, in my opinion, for the proper validation and efficacy of the method.
First of all, I want to point out how temporal resolution has been extensively studied: it's very important to be able both to measure physiological regimes and to resolve closely spaced velocities.
To this end, it's possible, at first, to consider an upper limit for speed detection, starting from the analysis of Whittaker-Shannon theorem: the *critical sampling interval* is given by half the inverse of the maximum frequency content of the signal. This value should match the CCD frequency band-width that is approximately $BW = \frac{1}{4ms} = 250\,Hz$.
In this way, first consider the Gaussian model for the cross-correlation function:

$$G(\tau) = A\,exp\left[-\frac{(\tau - \frac{s}{v})^2}{\delta\tau^2}\right] \tag{4.1}$$

with $\delta\tau = \frac{a_{eff}^2}{v}$ and effective ROI area defined as $a_{eff} = \omega_0^2 + a^2 + r^2$, given by the sum of optical resolution ω_0, the pixel size a, and tracer size r.[35] Then by taking as band-width

the $\frac{1}{e^2}$ width of the transformed signal, and considering mean values of $a = 6\mu m$ and $r = 10$ $\omega_0 = 0.8\mu m$, this results in the following constraint:

$$v_{max} \leq \frac{BW}{2}\, a_{eff} \leq 1800\,[\frac{\mu m}{s}] \tag{4.2}$$

Once established an upper boundary for the useful application of the method, it's also important, as anticipated, to understand the resolving power of this methods, that is: what is the minimum separation between velocities that we can expect to measure?
To answer this in a fast and clever way, it's better to shift into frequency domain, expressing a function describing two different regimes with it's temporal Fourier Transform:

$$G(\sigma) = e^{i\sigma\frac{s}{v_1}}\; e^{-\frac{\sigma^2}{4}\delta\tau_1^2} + e^{i\sigma\frac{s}{v_2}}\; e^{-\frac{\sigma^2}{4}\delta\tau_2^2} \tag{4.3}$$

It's apparent the beating between two oscillatory components, whose trend is:

$$cos\left[\frac{\sigma}{2}\left(\frac{s}{v_1} - \frac{s}{v_2}\right)\right] \tag{4.4}$$

These can be solved if the corresponding frequency lies within the band width BW = 250 Hz of the detector. It's a fair assumption to describe closely spaced velocities as:

$$v_1 = \langle v\rangle + \delta v; \quad v_2 = \langle v\rangle - \delta v \tag{4.5}$$

So that:

$$\delta v > \frac{\langle v \rangle}{2\, s\, BW} \tag{4.6}$$

Employing the mean values $s = 200\mu m$, $\langle v \rangle = 500\frac{\mu m}{s}$ the minimal regimes separation results to be:

$$\delta v > 2.5\frac{\mu m}{s} \tag{4.7}$$

and it is way lower than the minimun separation expected (or measured) in the biological model employed (Zebrafish embryos).

At last, as briefly stated in the article, it's worth to emphasize that wide field images allow an interesting kind of visualization, called *carpet images*. These are images synthesized by flanking a line (that is the x-axis of the image) acquired on the CCD along the flow over the acquisition time, that is the x-axis in Figure 2 in the article. It's easy to see how it's possible to identify at a glance different trajectories simply by looking at the inclination of the bright lines: this allows a windowed analysis, capable of highlighting the different regimes one by one. As an example, I present in figure 4.1 data from a two velocity regime, inside a square glass channel:

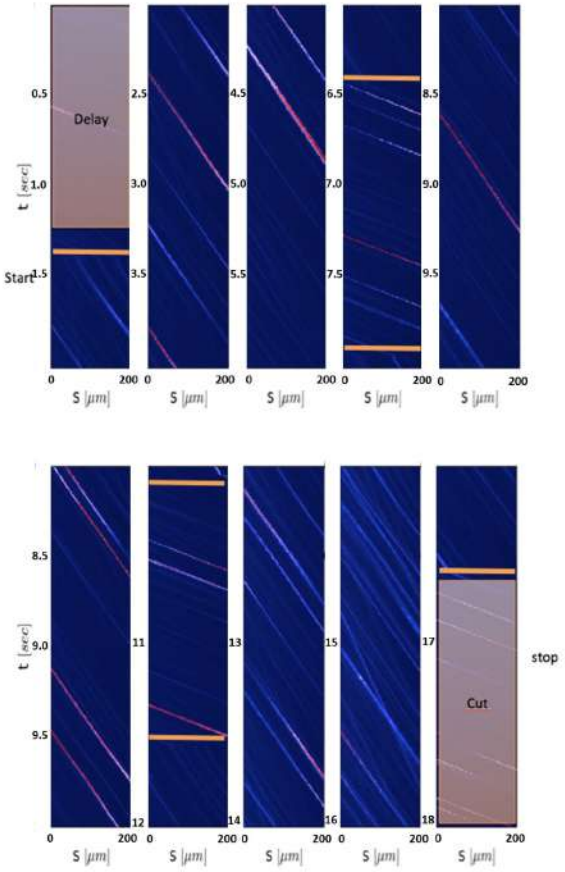

Figure 4.1: Trajectories with different steepness describe different regimes. The period of the pulsation is T = 6.5 s, so that the yellow horizontal bars divide the two regimes with durations $\Delta t_1 = 5s$ and $\Delta t_2 = 1.5s$. First and last bit are taken away, to get rid of fixed delays that would just disturb the CCF computations.

By applying a CCF analysis to each of the windowed signals, each single regime can be isolated and focused, greatly improving $\frac{S}{N}$, as can be seen in figure 4.2:

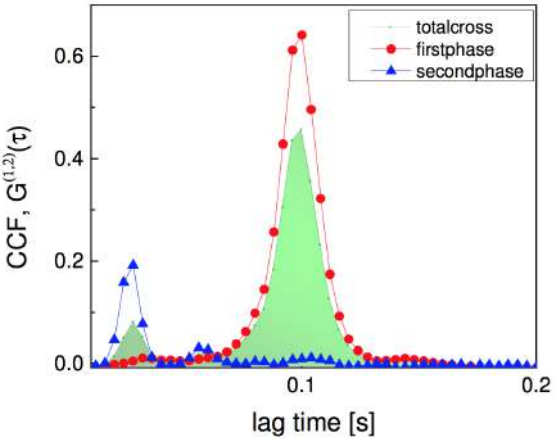

Figure 4.2: CCF computed for single regimes (blue and red curves), compared with the cumulative green plot, full time-signals were employed in the computation

Chapter 5

Spatio-temporal Image Correlation Analysis of blood flow in Branched Vessel Networks of zebrafish embryos

An experiment is a question which science poses to Nature and a measurement is the recording of Nature's answer.

Max Planck

I devoted much time to the improvement of data crunching methods and to the design of new ones, that could be easily employed by an external user in order to map spatially complex flow structures, in particular intersomitic vessels in Zebrafish embryos. I had two concurrent goals in mind: both to obtain fast and efficient algorithms for STICS, and also to test them studying a relevant biological system. The result of my work is represented by efficient algorithms that can extrapolate all the needed information about blood flow (up to a mapping resolution of 10 μm) in matter of few tens of seconds: it can discriminate between multiple flow directions and regimes, allowing the user only to work at high level, e.g. selecting subregion and time interval. All the programs are open source and available in an on-line repository (see Appendix). Here is the article (published on JBO) that presents the relevant achievements.

Spatio-temporal Image Correlation Analysis of blood flow in Branched Vessel Networks of zebrafish embryos.

Nicolo G. Ceffa[1], Ilaria Cesana[1], Maddalena Collini[1,2,3], Laura D'Alfonso[1], Silvia Carra[4], Franco Cotelli,[4] Laura Sironi[1,*] and Giuseppe Chirico.[1,2,3]

1. Dipartimento di Fisica, Università di Milano-Bicocca, Piazza della Scienza 3, 20126, Milano (I);
2. CNR - ISASI, Institute of Applied Sciences & Intelligent Systems, Italy
3. Nanomedicine Center, Università di Milano-Bicocca, Via Cadore, 4820900 – Monza (I).
4. Dipartimento di Biologia Via Celoria 26 Milano, 20133 Italy

Abstract.
Ramification of the blood circulation is relevant in a number of physiological and pathological conditions. The oxygen exchange occurs largely in the capillary bed and the cancer progression is closely linked to the angiogenesis around the tumor mass. Optical microscopy has made impressive improvements in in-vivo imaging and dynamic studies based on correlation analysis of time stacks of images. Here we develop and test advanced methods that allow to map at the resolution of 10-20 micrometers the flow fields in branched vessel networks. The methods, based on the application of Spatio Temporal Image Correlation Spectroscopy and its extension to cross-correlation analysis are applied here to the case of early stage embryos of Zebrafish.

Keywords: Image Correlation; hemodynamics; Single Plane Illumination Microscopy

*: corresponding authors, Laura Sironi, Laura.sironi@mib.infn.it, Giuseppe Chirico, Giuseppe.chirico@unimib.it

1. Introduction.

Flow regulation of the physiological activity is a wide field of life sciences.[1] Both in human beings and in artificial environments, three dimensional structures such as cellular aggregates leading to organelles or bacterial colonies are often immersed in an aqueous fluid in motion and subjected to hydrodynamic forces.[2] The progression of a wide number of diseases is affected directly by the blood circulation. An important example is cancer[3] and its metastases. Some diseases produce an impaired blood supply to organs.[4,5] These different fields of research share a common feature. The fluid circulation presents pulsatile, occasionally irregular, flow with ramifications in evolution and it requires high spatial and time resolution to be studied.

The focus of the field of angiogenesis research has in recent years shifted toward the analysis of network formation mechanisms, also connected to tissue engineering,[6] as well as the study

of vessel maturation and remodeling processes.[7] This has led to the discovery of vascular guidance and networking molecules as well as the identification of vessel maturation-regulating molecules such as the angiopoietins (ANG) and the PDGFs.[8] In this field, medical research is often exploiting small animal models such as Zebrafish embryos[9] and juvenile transparent fishes,[10,11] for pilot in-vivo studies. Besides, the advances of microfluidics are getting large influence on several fields of microbiology, providing new tools to investigate processes developing under flow, such as bacterial biofilm formation.[12]

Our aim is therefore to devise methods to quantitatively map the flow field at the branching point along a vessel network. We describe and test an algorithm able to quantify in a user-independent way the dominant flow in a branched network of sprouting vessels. In order to show real field applications, we apply these algorithms on the Zebrafish embryo model. Our method is based on the use of Spatio Temporal Image Correlation Spectroscopy (STICS) analysis coupled to Single Plane Illumination Microscopy (SPIM).[13] Cross-correlation analysis was already applied on a dual or multi-spot level for the detailed analysis of the flow in straight microfluidic capillaries and to straight vessels in-vivo.[9] STICS analysis was applied to wide field images of blood flow in vessels as a validation for intra-surgical applications.[14] We extend here the original STICS algorithm[13] to the cross-correlation over different fields of view chosen along the flow direction in order to increase the dynamic range for the measurement of the flow speed and use a multicomponent analysis of the correlation maps that allows us to exploit the amplitude of the correlation map to evaluate the flow fractionation at the branching points.

2. Experimental Section.

2.1 SPIM Setup. The SPIM setup[15,16] employs an argon–krypton laser (Melles Griot), expanded 1:4 and focused into the back aperture of an illumination objective (Olympus 4×, 0.1 N.A.). The fluorescence emission is selected by a band-pass filter and is detected by an EMCCD

detector (Cascade II, Photometrics). The maximum acquisition rate was 4 ms/frame, on reduced regions of 40 × 250 μm^2.

2.2 Zebrafish Embryos. The measurements were done on embryos of Zebrafish (3 days post fertilization, d.p.f.). We used the transgenic line mitfa$^{w2/w2}$; roy$^{a9/a9}$; Tg(kdrl:EGFP)^{S843}; Tg-(gata1:dsRed)^{sd2}, carrying green-labeled epithelium (EGFP) and red-labeled (dsRed) red blood cells.[17] The zebrafish embryos were anesthetized[18] with tricaine [40 mg/L tricaine (ethyl 3-aminobenzene methansulfonate, Sigma-Aldrich Corporation, St. Louis, MO)] and positioned in a 2 mm-diameter fluorinated ethylene propylene tube (FT2X3, Adtech Polymer Engineering, Frampton Mansell, U.K.) and then immersed in a water cell.[16,19]

2.3 STICS images analysis. The STICS images were computed on a time stack of M images $S = \{I_j\}_{j=0,..M}$ taken at M times spaced by δt ranging typically from 13 to 19 ms (corresponding to 74 to 52 frame per second of the EMCCD, the fastest rates compatible with the chosen field of view). We take the SPIM plane as the x-y plane. We assume that the flow velocity lies in this plane and is $\vec{v} = (v_x, v_y)$. Each image has a size of X×Y pixels. The image auto-correlation function was computed on the fluctuation matrices, $\delta I_j(x,y) = I_j(x,y) - \langle I_k(x,y) \rangle_k$, by the FFT algorithm:

$$G(\xi,\eta;k\delta t) = \sum_{j=0}^{M-k} FFT^{-1}\left[FFT[\delta I_j]FFT^{*}[\delta I_{j+k}]\right]/(M-k) \qquad (1)$$

Each image of the time stack was padded with zeros up to double its size before performing the FFT.

On each correlation image, corresponding to the lagtime τ, we automatically selected the position (ξ_{max}, η_{max}) of the maximum by fitting the image to a 2D Gaussian profile. The amplitude of the STICS function was derived from the amplitude of the Gaussian fit function, subtracted for the possible background.

Even though the morphological images are available, we do not want to presume any a-priori knowledge on the flow direction. We have then simply computed the STICS image on rectangular ROIs aligned with the axes of the image as it is acquired. In order to evaluate the components of the flow velocity in the SPIM plane, we follow the position of the STICS image with the lagtime over at least 5-10 lagtime points, up to a lagtime τ_{fit}. We have checked that the condition to recover the STICS amplitude is that the ROI size is at least $S_{ROI} \cong 2\ v_{xy}\ \tau_{fit}$. For a flow of the order 400 μm/s and $\tau_{fit} \cong 40$ ms, this corresponds to a size of 16 μm, or at least 20 pixels. This is our spatial limitation in the reconstruction of the field flow.

3. Results and discussion.

3.1 STICS allows to follow the flow along curved vessels. We want to devise methods to map the blood flow in tiny branched capillaries. The flow should be characterized in terms of direction and amplitude of the velocity, and we will need to evaluate the flow branching ratio at the ramifications along the network. The rationale of the methods that we are describing is to auto- and cross-correlate in space and time stacks of images acquired through a wide field Single Plane Illumination Microscope (SPIM). In general, we could also map the velocity field by tracking, and then averaging, many trajectories of individual red blood cells. This is not always feasible for example when the vessel morphology cannot already be singled out from the images (initial angiogenesis) or the heart pulsation affect the flow, such as in veins. Spatio-Temporal Image Correlation Spectroscopy (STICS) offers the advantage to provide directly an average flow map in which the heart pulsation effect is averaged out. With STICS we obtain from a time stack of images a series of autocorrelation maps (**Eq.1**), $G(\xi, \eta; \tau)$, function of the lag time τ. For a uniform drift the map assumes the shape of a 2D quasi-Gaussian[13,16] function whose maximum occurs at the position $\vec{r}_{max} = (\xi_{max}, \eta_{max})$, measured with respect to the origin of the autocorrelation map and it is a function of τ. We want to exploit here the possibility to

follow both the position and the amplitude of the auto-correlation map maximum as a measure of the flow velocity and of the relative amount of cells taking either of the arms of a branching point. We will then extend this concept to cross-correlation of different ROIs in the field of view.

We first assess the problem to reconstruct the flow along a curved vessel independent of possible ramifications. We assume that flow is occurring mainly in the SPIM plane and analyze the time stacks of images according to the STICS algorithm on a Region of Interest (ROI, rectangular in shape) chosen in such a way to encompass a small (40 μm) tract of the vessel. We first evaluate at different positions along the putative vessel axis the STICS image at increasing lagtimes and fix the lagtime at the maximum value, τ_{fit}, for which the maximum $\vec{r}_{\max} = (\xi_{\max}, \eta_{\max})$ of the STICS image lies within the SITCS image by at least 5-6 pixels. The average velocity of the cells is obtained as $\vec{v} = \left(-\xi_{\max} / \tau_{fit}, -\eta_{\max} / \tau_{fit}\right)$.[16,20,21] The speed is computed, by assuming non-constrained motion, as $d_{\max} = \sqrt{\xi_{\max}^2 + \eta_{\max}^2}$.

We need to find a compromise between the finesse of the spatial reconstruction of the flow, the computation time and the spatial resolution on the STICS image. The latter depends on the brightness of the tracers. In our hands, for red blood cells in living embryos the minimum displacement of the STICS maximum for which the corresponding velocity uncertainty is smaller than 15% is $|\vec{r}_{\max}| \cong 4$ pixels (that is 3.2 μm in the sample plane). The lower the signal/noise, the larger the minimum value of $|\vec{r}_{\max}|$ is and the coarser is the reconstructed flow map.

Once the ROI size and the fitting lagtime have been chosen, the algorithm computes sequentially a set of STICS maps, updating at each step the investigation ROI with a rigid translation along the vector $\vec{T} = \alpha(\xi_{\max}, \eta_{\max})$. The choice of small propagation factor $\alpha < 1$ allows to oversample the flow map. We typically adopted $\alpha = 0.5$. A flow line can be built

by assigning each flow velocity vector to the center of the corresponding ROI and by representing it with the Quiver python class.[22] As can be seen from **Fig. 1A**, we can follow the blood flow on a wide field of view (750 × 750 μm^2) with a good resolution, ≅ 5 - 10 μm (**Fig.1C** and **Fig.1D**).

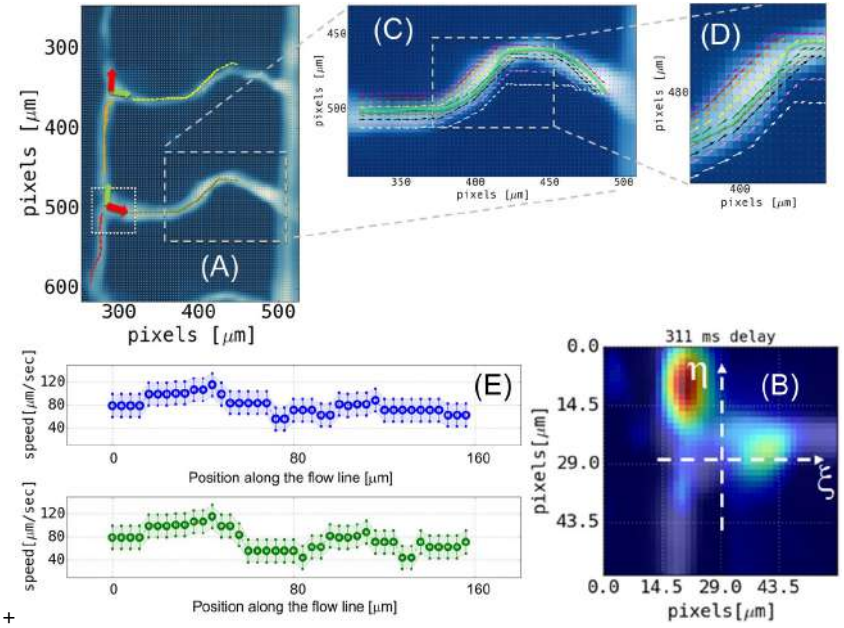

Figure 1. Evaluation of the red blood cells flow in zebrafish embryo (3 dpf) vessels based on STICS maps from ROIs of [14 × 14] pixels (pixel size = 2.9 μm). All the flow analyses have been done with propagation factor α = 0.5. **Panel A** reports a wide field picture (256 × 256 pixels = 742 × 742 μm^2) of the blood circulation in the abdomen of the embryo. The flow field is reported in four linear tracts of the vessel network as thin arrows whose length is proportional to the speed. At two branching points the dominant and marginal flow components are reported as green and red filled arrows, respectively. The **panel B** reports the STICS map for the vessel branching point marked by a dotted white box in **panel A**, at lag time τ = 311 ms. **Panels C** and **D** are zoomed images on one intersomitic vessel in which the trajectories computed from nine different starting points have

been reported together with the average flow curve (see text). **Panel E** reports the flow speed along the reconstructed average flow (green) line and the adjacent (blue) line reported in panel C.

When approaching a branch in the vessel network, the STICS image assumes a double component character (see **Fig.1B**). At each step along the path (i.e. on each ROI) we evaluate the relative amplitude of the two peaks and displace the ROI along the direction that corresponds to the most relevant component (according to the maximum of each component detected in the STICS image). In this way, starting from two different points along the vessel network, we are able to evaluate the flow velocity even at the branching points (**Fig.1A**) and follow it along the individual arms (**Fig.1C** and **Fig.1D**). We observed a dependence of the resulting trajectory on the evolution parameter α. We have found that for values $\alpha \cong 0.5$ of the evolution parameter, the flow trajectories follow closely the vessel axis as can be measured from the morphological image (**Fig.1A**). There is still a dependence on the position of the starting point (the center of the first ROI of the sequence) along the putative cross-section of the vessel, as can be judged from **Fig.1C** and **Fig.1D** (different discontinuous colored lines). However the trajectories coalesce on a common path that we have selected by averaging on each cross-section of the vessel (at steps of 20 μm) the points that correspond to the position of the individual flow lines. The resulting line, reported as a thick semitransparent green line in **Fig.1B** and **Fig.1C**, can be considered as the common flow path in the selected vessel. There is no appreciable dependence of the amplitude of the flow speed on the starting point of the trajectory, as can be judged from the plot of the flow speed along two flow lines reported in **Fig.1E**. This is to be expected since we are tracking here red blood cells that are approximately of the size of the capillary diameter.

3.2 STICS allows to estimate flow branching ratios at the vessel ramifications. The application of the STICS algorithm on a ROI that encompasses a ramification of the vessel

network, such as in the black rectangle of **Fig.2A**, results in correlation images in which two components can be singled out (**Fig.2B**). These components can be ascribed to the cells that take either of the two branches. The rapidity of their displacement from the center of the correlation image, $\vec{r}_{\max}^{(1)} = \left(\xi_{\max}^{(1)}, \eta_{\max}^{(1)}\right)$ and $\vec{r}_{\max}^{(2)} = \left(\xi_{\max}^{(2)}, \eta_{\max}^{(2)}\right)$, as a function of the lag-times is the measure the flow direction and the flow speed for cells flowing in each arms. The direction of the velocity vector follows very well the morphology of the vessel ramification as can be judged from the superposition of the correlation images with the morphological images (**Fig.2B**). To this purpose, the correlation images reported in **Fig.2B** have been inverted by a central symmetry with respect to the center of the correlation space.

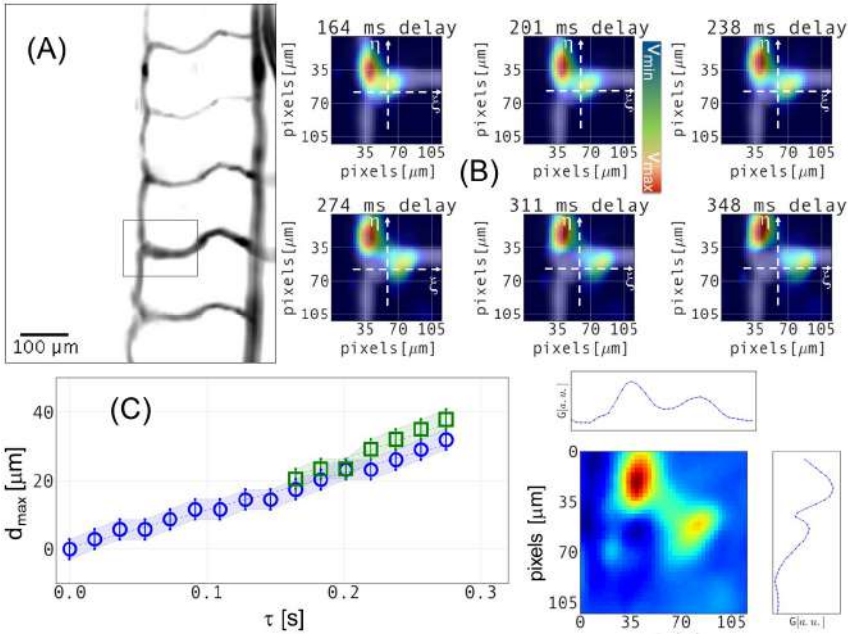

Figure 2. Analysis of the flow ramification at branching points. **Panel A**: morphological image taken on a Zebrafish embryo (3 dpf) obtained as the standard deviation projection the time stack of images used for the STICS analysis. **Panel B**. STICS maps computed on the ROI selected in panel A (black rectangle) for increasing

lag-time, from 164 ms to 348 ms from left to right and from top to bottom (flow speed coded by a "jet" LUT; morphological images superimposed in light blue). **Panel C.** Linear fit of position of the maximum of the STICS images as a function of the lag-time. Open (blue) symbols refer to the prevalent component in each STICS image. Filled (green) symbols refer to the marginal component (visible for lag-times $\tau \geq 170$ ms). The linear fit to the data (dashed lines, same colour code) gives velocities $v_1 = 55 \pm 1.5$ µm/s and $v_2 = 69 \pm 3$ µm/s for the prevalent and the marginal components respectively. **Panel D** reports the Gaussian fitting of the STICS map (lag time = 348 ms) together with the profile plots along the ξ and η axes.

In the correlation maps (**Fig.2B**) one peak was found to be always larger in magnitude irrespective of the lag-time. Moreover, the maximum projection image showed very similar signals on the two arms indicating that the emission of the individual red blood cells passing through the two arms is very similar. We assume therefore that the maximum amplitude of the two correlation components is proportional to the number of red blood cells flowing in one or the other ramification of the vessel branching. In the example discussed in **Fig.2**, the brightest component in the STICS map (**Fig.2D**) corresponds to the red blood cells flowing upwards, amounting to 66 ± 1 % of the overall amplitude. The marginal component represents cells flowing from left to right, amounting to 34 ± 1 % of the overall amplitude. The marginal component can be singled out with reasonable signal/noise ratio (10%) only for lag-times $\tau \geq$ 170 ms. Two values of the flow speed can be computed from the linear fit of the displacements of the maxima of each component as a function of the lag-time, as reported in **Fig.2C**: we measure $v_1 = 55 \pm 1.5$ µm/s and $v_2 = 69 \pm 3$ µm/s for the prevalent and the marginal components respectively. We find then that the marginal component is slightly faster than the prevalent one. This corresponds quite well to the observation that the left-right vessel arm is visibly larger (see **Fig.2A**) than the bottom-up arm and the fact that the vessels are approximately of the size of the red blood cells diameter. It must be noticed that the algorithm for the computation of the flow velocity used here is customized to the case of right-angle crossing between vessels as in

Fig.2A (box). Since the flow is constrained to occur along the vessel axis, the displacement of the maximum of the auto-correlation map may in general be not along a line passing through the centre of the map. In this case we should compute the flow speed along the vessel axis through the incremental algorithm $\left|\vec{r}_{\max}(\tau+\delta\tau)-\vec{r}_{\max}(\tau)\right|=\left|\vec{v}\right|\delta\tau$.

3.3 Spatio-temporal Cross-Correlation analysis enhance mapping features. The possibility to spatially map the flow relies on the choice of a small ROI on which we apply the spatio-temporal correlation algorithm. The space resolution of the reconstructed flow depends on the size of the ROI (half its linear size = $0.5\times S_{ROI}$). However, a second key parameter for obtaining high precision flow speed estimations is the max tracer speed (K) inside the investigation ROI. If we assume that at least 5 lag-time points are needed to linearly fit the relation between the displacement $\left|\vec{r}_{\max}\right|$ and the lagtime, K can be estimated from the ROI size (S_{ROI}) and the CCD frame rate (fps) as $K = S_{ROI}\times$ fps / 5. In the experiments reported in **Fig.1** and **Fig.2**, fps = 74 frames/s and S_{ROI} = 16 µm and we compute K ≅ 240 µm/s. If we had larger speed values, we should increase the ROI size loosing then in spatial resolution of the flow mapping. Moreover, if the flow is not aligned with the ROI axes we would need to increase the ROI size in both the ξ and η directions. This would increase substantially the computation time.

In order to solve these issues, we propose to adopt an approach consisting in two-stage analysis:

1- perform a first STICS on a ROI with small lag-time in order to evaluate the flow direction;

2- rigidly translate the ROI of half the size of the original ROI in the flow direction detected at step 1, and perform a spatio-temporal *cross-correlation* between the original and the translated ROI (see **Fig.3A**).

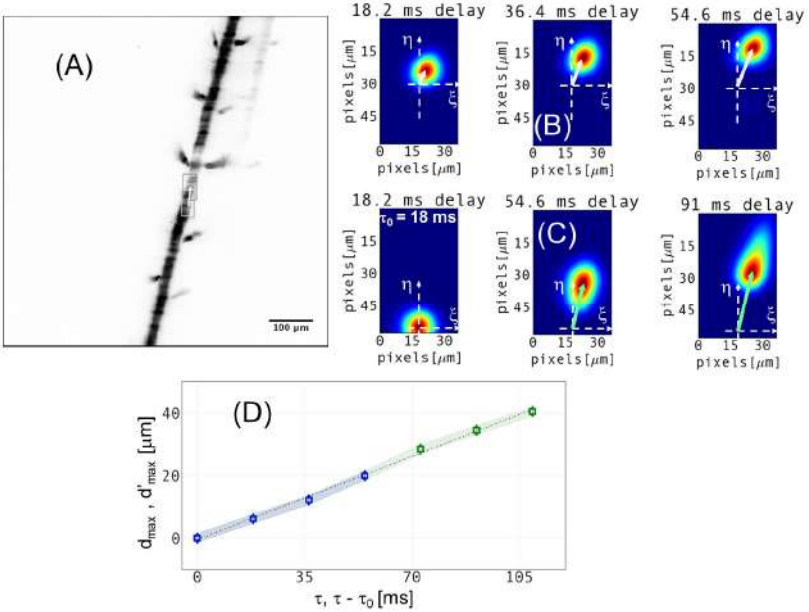

Figure 3. Cross-correlation spatio-temporal analysis. **Panel A** reports the time average of the stack of images. The light and dark gray rectangular boxes are the original and translated ROI, respectively. The white arrow indicates the translation vector. **Panel B** reports three auto-correlation images computed on the original ROI for lagtimes τ = 18.2 ms, 36.4 ms and 54.6 ms. The white arrow indicates in each STICS image the displacement vector $\vec{r}_{max} = (\xi_{max}, \eta_{max})$. **Panel C** shows the spatio-temporal *cross-correlation* maps between the original and translated ROIs for absolute lagtimes τ = 18.2 ms, 54.6 ms and 91 ms. The light green arrow indicates in each cross-correlation image the relative displacement vector $\vec{r}'_{max} = (\xi'_{max}, \eta'_{max})$. **Panel D** reports the plot of the displacement $d_{max} = \sqrt{\xi^2_{max} + \eta^2_{max}}$ as a function of the absolute lagtime τ (blue colour), and $d'_{max} = \sqrt{(\xi'_{max})^2 + (\eta'_{max})^2}$ as a function of the reduced lagtime, $\tau - \tau_0$ (green colour, τ_0 =18 ms). The dashed line is the best linear fit to the data and corresponds to the speed v = 380 ± 9 µm/s.

In this way we can increase the dynamic range of the speeds that can be detected. A flow speed almost 4 times larger than in **Fig. 2** can be measured on the vessel reported in **Fig.3A** with 3% accuracy at 20 μm size resolution (S_{ROI} = 20 μm). At the same time, we are able to keep the computational costs at the same level of the original autocorrelation algorithm. The details of the algorithm can be gained by comparing **Figs.3B** (STICS correlation) to **Fig.3C** (STICCS, cross-correlation). We evaluate the flow velocity on the cross-correlation images by translating the correlation frame of reference (ξ,η)at the position (ξ_0, η_0) at which the cross-correlation peak is first detected and the lag-time τ axis to the corresponding lag time, τ_0 (see **Fig.3C**). The two components of the flow velocity can then be evaluated as the inverse of slope of $\xi - \xi_0$ and of $\eta - \eta_0$ (the corresponding vector is reported as a white arrow in **Fig.3C**) as a function of $\tau - \tau_0$. This estimate is in very close agreement with the one obtained on the autocorrelation images, as can be judged from **Fig.3 D** (open and filled symbols).

4. Conclusions.

We have devised and tested correlation and cross-correlation algorithms, specifically designed for single plane illumination microscopy, that allow to analyse blood flow in branched vessels. These involves the computation of the spatio-temporal correlation (STICS) and cross-correlation (STICCS) images and the analysis of the resulting maps in terms of multiple components. From the relative amplitudes of different components of the STICS map we assign the prevalent flow direction at branching points and we are able to follow the flow at the ramification, also measuring the flow speed. The application of cross-correlation spatio-temporal methods on two different ROIs on the stacks of images allow to enhance the dynamic range of the flow speed measurements and to map with 5 – 10 micrometers resolution the flow in extended vessel networks. An example of the resulting flow map reconstruction on two consecutive branching points can be seen in **Fig.1A**. These algorithms could be a great help in

analysing huge amount of data collected in-vivo in the field of developmental biology or in-vitro in the setup of vascularized micro-incubators for tissue engineering.

Acknowledgments. This work was supported by Academic Funding Unimib 2016 (G.C. and L.S.).

References.

1. D.J. Duncker, R. J. Bache. “Regulation of coronary blood flow during exercise”, *Physiol. Rev.* **88**, 1009-1086 (2008) [doi: 10.1152/physrev.00045.2006].
2. L. Hall-Stoodley, J.W. Costerton, P. Stoodley. “Bacterial biofilms: from the natural environment to infectious diseases”, *Nat. Rev. Microbiol.* **2(2)**, 95-108 (2004) [doi: 10.1038/nrmicro821].
3. S. Alexander, et al. “Dynamic imaging of cancer growth and invasion: a modified skin-fold chamber model”, *Histochem. Cell Biol.* **130**: 1147-1154 (2008) [doi:10.1007/s00418-008-0529-1].
4. P. Carmeliet, “Angiogenesis in health and disease”, *Nat. Med.* **9**, 653–660 (2003) [doi:10.1038/nm0603-653].
5. L. Sironi et al. “In vivo flow mapping in complex vessel networks by single image correlation” *Sci. Rep.* 4, 7341 (2014) [doi: 10.1038/srep07341].
6. B. Zhang et al. “Biodegradable scaffold with built-in vasculature for organ-on-a-chip engineering and direct surgical anastomosis”, *Nat. Mat.* **15(6)**: 669–678 (2016) [doi: 10.1038/nmat4570].
7. D. Ribatti, E. Crivellato. "Sprouting angiogenesis", a reappraisal . Develop. Biol. 372(2): 157-165 (2012) [doi: 10.1016/j.ydbio.2012.09.018].
8. C. Korn, H. G. Augustin, “Mechanisms of Vessel Pruning and Regression”, *Developmental Cell Review*, **34**, 5-17 (2015) [dx.doi.org/10.1016/j.devcel.2015.06.004].
9. P. Pozzi et al. “Electron multiplying charge-coupled device-based fluorescence cross-correlation spectroscopy for blood velocimetry on zebrafish embryos”, *J. Biomed. Opt.* **19 (6)**, 067007 (2014) [doi:10.1117/1.JBO.19.6.067007].
10. R.M. White et al. “Transparent adult zebrafish as a tool for in vivo transplantation analysis”, *Cell Stem Cell.* **2**, 183–189 (2008).
11. L. Fieramonti et al. “Quantitative measurement of blood velocity in zebrafish with optical vector field tomography”, J. Biophoton. **8** (1-2), 52–59 (2015) [doi: 10.1002/jbio.201300162].
12. J. Bruchmann, “Multi-Channel Microfluidic Biosensor Platform Applied for Online Monitoring and Screening of Biofilm Formation and Activity”, *PLOS ONE* **10**, e0117300 (2015) [doi: 10.1371/journal.pone.0117300].

13. B. Hebert et al. “Spatiotemporal Image Correlation Spectroscopy (STICS) Theory, Verification, and Application to Protein Velocity Mapping in Living CHO Cells”, *Biohys. J.* 88 3601–3614 (2005).
14. M. Rossow, W.W. Mantulin, E. Gratton, “Spatiotemporal image correlation spectroscopy measurements of flow demonstrated in microfluidic channels”, J. Biomed. Opt. 14, 024014 (2009) [doi: 10.1117/1.3088203]
15. P.G. Pitrone et al. “OpenSPIM: an open-access light-sheet microscopy platform”. *Nat. Methods* 10, 598– 599 (2013) [doi:10.1038/nmeth.2507].
16. C. A. Marquezin et al. “Image Cross-Correlation Analysis of Time Varying Flows”, *Anal. Chem.* 88, 7115–7122 (2016) [doi: 10.1021/acs.analchem.6b01143]
17. N.D. Lawson; B.M. Weinstein, “In vivo imaging of embryonic vascular development using transgenic zebrafish”, *Dev. Biol.* **248** (2), 307– 318 (2002) [doi:10.1006/dbio.2002.0711].
18. M.A. Akimenko et al. “Differential induction of four msx homeobox genes during fin development and regeneration in zebrafish”, Development **121** (2), 347–357 (1995).
19. A. Bassi et al. “In vivo label-free three-dimensional imaging of zebrafish vasculature with optical projection tomography.”, *J. Biomed. Opt.* **16** (10), 100502 (2011) [doi: 10.1117/1.3640808].
20. J.W. Krieger et al. “Imaging fluorescence (cross-) correlation spectroscopy in live cells and organisms”, *Nature Methods* 10, 1948-1974 (2015) [doi: 10.1038/nprot.2015.100].
21. M. Bouzin et al. “An intermittent-model Fourier-space analysis of the intracellular motion of gold nanostars by scattering image correlation”, *Biophys. J.* **109**: 2246-2258 [doi:10.1016/j.bpj.2015.10.025]
22. John Hunter, Darren Dale, Eric Firing, Michael Droettboom and the Matplotlib development team. The Matplotlib development team, 10 May 2017 (accessed 6 July 2017) [https://matplotlib.org/contents.html]

5.1 Spotlight

The main goal of this chapter consists in the development of *variations* of the conventional STICS analysis method, and to the construction of a toolbox that should be at the same time extremely solid and also user-friendly.

First of all, these methods require almost no a-priori knowledge on the flow: the ROI and the timescale selection is the only step that involves a user decision, and, per se, are very easy to understand in a completely intuitive way. Moreover STICS maps (despite their complex mathematical backbone) are extremely clear and easy to read, both for qualitative and quantitative analysis. In particular, looking at the case of branched vessels, the power of the method shows itself in mapping, even in one single run (from a stack of a minimum of 300-400 frames), high resolution vectorial informations about flow speeds at a ramification point. It informs also on the preferential routes taken by red blood cells. All this is displayed inside a single 2D image.

I dedicated special attention at developing fast algorithms, as fast as I think could be designed without employing parallel computing: introducing STICCS (and Figure 3 stressed exactly this point) allows to measure higher speed values, which would be otherwise unreachable, without employing a faster

detector, or without encompassing a much wider ROI. The first solution would greatly increase setup cost, the latter would require higher computational power, inevitably slowing down the analysis. Instead, by introducing a spatial delay between two ROIs, along the putative flow direction, allows the retrieval of such flow speed with high accuracy, without any increase in hardware requirements nor any sensitive slowing down in the computational process. I am convinced that, from here, the best course of action would be to invest time and effort in translating all the algorithms to heavy parallel computing, both exploiting the power of mutli-core CPU and modern GPU cards.

Chapter 6

3D extension: breaking *the wall*

The good thing about science is that it's true whether or not you believe in it.

Neil deGrasse Tyson

It's fairly clear at this point that there is an intrinsic limitation hidden in the methods proposed so far: the analysis is restricted on a selected *plane*, and even if this can be more than enough when studying microfluidic systems (acting on design one can always engineer them to achieve planar or semi-planar flow fields) it's not often the best situation when investigat-

ing a biological system, where interesting stuff is happening in complex 3D geometries.

I'd like to point out that, in previously presented work, where I studied hemodynamics in Zebrafish microvessels, I assumed *a priori* almost planar geometries and this is completely justified in the specific case, since I took care to image in the same light sheet both the major vessels, so that most of the branching occur in the same (excited) sagittal plane (zfin.org/zf_info/anatomy.html).

In this chapter I want to address directly 3D geometries of flow. A common approach consists in employing scanning systems, in detection and/or excitation, in order to acquire 3D image stacks: this is quite effective and many advances have been recently achieved in order to improve both resolution and, more importantly since this is the real challenge, acquisition speed.[36,37] This solution, even if it consists in *true* 3D inspection, results in costly hardware and it inherently slows down acquisition process. Moreover it increases both operational (in particular system alignment) and information complexity: it gives 4D matrices of data, that require high computational power for manipulation. The solution proposed here shows that it's possible to obtain information on 3D flow fields still focusing on the time evolution of STICS data, taken in a classic (2D) SPIM configuration. The main trick consists in directly

deriving the spatio-temporal correlation fitting function under the hypothesis of 3D arbitrary flow, and then simply looking at the evolution of its shape and position with the lag-time, marginalizing on a subspace, that is the 3D information (2D space coordinates plus one time coordinate, the lag-time) contained in a SPIM video acquisition. To this goal, I think it's useful to dive deeper into the theory presented in Chapter 2.4, where STICS fitting function is presented for 2D diffusion and drift. Let's assume, for now, that investigation volume can be approximated by a 3D Gaussian profile and that, as most general case, both 3D diffusion and drift are present. The basic correlation function can be described as:

$$G(\Delta, \tau) = (W(x) * \delta C(x,t)) \star (W(x) * \delta C(x,t)) \qquad (6.1)$$

where:

- "$*$" indicates convolution, while "$\star$" defines a correlation operation;
- $W(x) = gaus\left(\frac{x}{\sqrt{\frac{\pi}{2}}\omega}\right)$ is a 3D Gaussian profile, with x 3D vector and ω = beam waist;
- $\delta C(x,t)$ refers to fluorophores concentration fluctuations;
- Δ and τ specify spatial and temporal delays, respectively.

Writing explicitly convolution and then correlation it's readily found that:

$$G(\Delta,\tau) = \int_{-\infty}^{\infty} W(x-\alpha)\delta C(\alpha,t)d\alpha \star \int_{-\infty}^{\infty} W(x-\beta)\delta C(\beta,t)d\beta \tag{6.2}$$

$$G(\Delta,\tau) = \int_{-\infty}^{\infty} d\gamma \int_{-\infty}^{\infty} dt \int_{-\infty}^{\infty} d\alpha \int_{-\infty}^{\infty} d\beta$$
$$W(\gamma-\alpha)\,\delta C(\alpha,t)\,W^*(\gamma-\Delta-\beta)\,\delta C^*(\beta,t-\tau) \tag{6.3}$$

$$G(\Delta,\tau) = \int_{-\infty}^{\infty} d\gamma \int_{-\infty}^{\infty} d\alpha \int_{-\infty}^{\infty} d\beta\, W(\gamma-\alpha)W^*(\gamma-\Delta-\beta) \int_{-\infty}^{\infty} dt\, \delta C(\alpha,t)\,\delta C^*(\beta,t-\tau) \tag{6.4}$$

The last equality serves as a guideline for performing successive integrations: first the time dependence is resolved following almost exactly the same steps performed in standard FCS derivation, that is solving Fick's diffusion (+ drift) law to recover an explicit expression for $\delta C(x,t)$; then, inserting the result in the complete expression and employing the fact that Fourier derivation and integration are completely independent linear operations, it's straightforward to recover the final functional form. Here I want to present the derivation in the most compact way, I hope without losing clarity.

For concentration fluctuations, referring to eq. 2.22 and 2.23:

$$\delta C(q,\tau) = \delta C(q,0) e^{(-4\pi^2 D q^2 - 2\pi i v q)\tau} \equiv \delta C(q,0) e^{f(q,\tau)} \quad (6.5)$$

where, as always, q and v are vectorial quantities. In order to insert this result in the general expression, back and forth Fourier Transformations are applied and extracted from the integral. Moreover recalling that, for an ideal solution, the zero lag-time concentration correlation can be evaluated as

$$\delta C(x,0) \star \delta C(y,0) = \langle C \rangle \, \delta(x-y) \quad (6.6)$$

this helps (along with the evaluation of Fourier Transforms of investigation profiles) to contract almost all the integral operations, so that it's readily found:

$$\begin{aligned} G(\Delta,\tau) = & \int_{-\infty}^{\infty} d\gamma \int_{-\infty}^{\infty} d\alpha \int_{-\infty}^{\infty} d\beta \int_{-\infty}^{\infty} dq' \\ & W(\gamma-\alpha) W^*(\gamma-\Delta-\beta) \\ & \left[\delta C(q',0) \star \delta C(\beta,0)\right] e^{f(q',\tau)} e^{2\pi i \alpha q'} \end{aligned} \quad (6.7)$$

$$\begin{aligned} G(\Delta,\tau) = & \int_{-\infty}^{\infty} d\gamma \int_{-\infty}^{\infty} d\alpha \int_{-\infty}^{\infty} d\beta \int_{-\infty}^{\infty} dq' \int_{-\infty}^{\infty} d\beta' \\ & W(\gamma-\alpha) W^*(\gamma-\Delta-\beta) \\ & \langle C \rangle \, \delta(\beta-\beta') \, e^{f(q',\tau)} e^{2\pi i \alpha q'} e^{-2\pi i \beta' q} \end{aligned} \quad (6.8)$$

$$G(\Delta,\tau) = \langle C \rangle \int_{-\infty}^{\infty} d\gamma \int_{-\infty}^{\infty} d\alpha \int_{-\infty}^{\infty} d\beta \int_{-\infty}^{\infty} dq' \\ W(\gamma-\alpha)W^*(\gamma-\Delta-\beta) \\ e^{f(q',\tau)} e^{2\pi i \alpha q'} e^{-2\pi i \beta q} \tag{6.9}$$

$$G(\Delta,\tau) = \langle C \rangle \int_{-\infty}^{\infty} d\gamma \int_{-\infty}^{\infty} dq' \\ W(q')W^*(q) e^{f(q,\tau)} e^{2\pi i q' \gamma} e^{-2\pi i q \gamma} e^{2\pi i q \Delta} \tag{6.10}$$

$$G(\Delta,\tau) = \langle C \rangle \int_{-\infty}^{\infty} \delta(q-q')\, dq' \\ W(q')W^*(q) e^{f(q',\tau)} e^{2\pi i q \Delta} \tag{6.11}$$

$$G(\Delta,\tau) = \langle C \rangle \int_{-\infty}^{\infty} |\hat{W}(q)|^2 e^{f(q,\tau)} e^{2\pi i q \Delta} dq \tag{6.12}$$

This is basically the same expression reported in eq. 2.20, here fully derived in 3D (+ time), without normalization factors. With this tool in hand, it's then just a matter of plugging in the correct expression for W and carry on calculations to obtain a full 3D fitting function. Expliciting the Fourier Transform of the investigation profile, then:

$$\hat{W}(q) = \sqrt{\frac{\pi}{2}}\omega \; gaus\left(\sqrt{\frac{\pi}{2}}\omega q\right) \tag{6.13}$$

$$G(\Delta,\tau) = \langle C \rangle \sqrt{\frac{\pi}{2}}\omega \int_{-\infty}^{\infty} e^{-2\pi^2 i\omega^2 q^2} e^{2\pi i \Delta\, q} e^{(-4\pi^2 D q^2 - 2\pi i v q)\tau}\, dq \tag{6.14}$$

To evaluate the integral, it's sufficient to complete the square in the integrand, to extract meaningful factors and obtain a straightforward 3D Gaussian integral, resulting in:

$$G(\Delta,\tau) = \langle C \rangle \sqrt{\frac{\pi}{2}}\omega \left(\frac{1}{\sqrt{\omega^2 + 4D\tau}}\right)^3 e^{\frac{-(\Delta - v\tau)^2}{\omega^2 + 4D\tau}} \tag{6.15}$$

This final equation, even if under approximations that will be soon further discussed, is perfect to understand how 3D STICS behaves. Here it is a 3D plot, where 3 different lag-times are merged together:

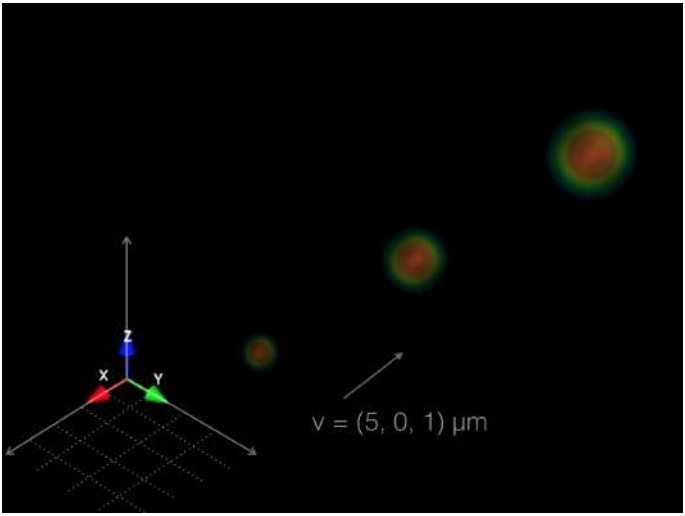

Figure 6.1: Simulation of 3D STICS function, with D = .1 and v = (5,0,1)μm

I choose specific parameters to highlight both diffusion and drift contributions, to observe how the correlation functions evolve in the most general case. Anyway, as already mentioned, this is rarely the case: in all the applications mentioned in this work, drift and diffusion exist on really different timescales (usually there is a diffusion coefficient of the order of $.3\frac{\mu m^2}{s}$ while drift speeds have a magnitude of tens or hundreds of $\frac{\mu m}{s}$), so that widening of the correlation sphere is dramati-

cally reduced in practice.

As last remark, it's quite singular that the same idea can be almost exactly applied in two so different contests: the theoretical, mathematical marginalization, working alongside with the effective, practical optical sectioning of the sample. In the following figures I performed a marginalization onto 2 different z-planes, both when a v_z is present and when, on the other hand, there is only planar drift in $\{\hat{x}, \hat{y}\}$-plane:

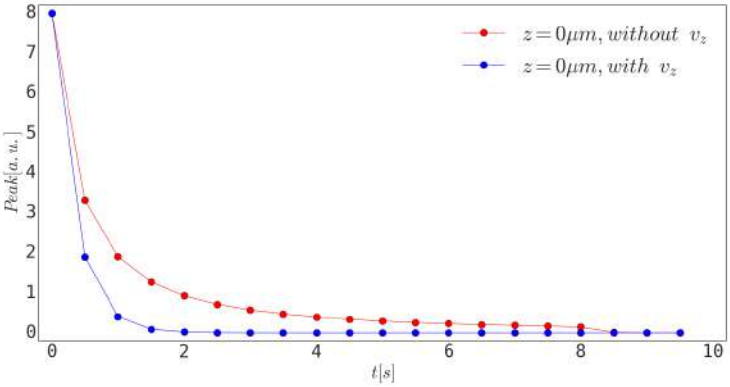

Figure 6.2: Marginalization of the 3D STICS function onto a plane of $0\,\mu m$ spatial delay in the $\hat{z}$ direction, both with and without a $\hat{z}$-component of fluid velocity.

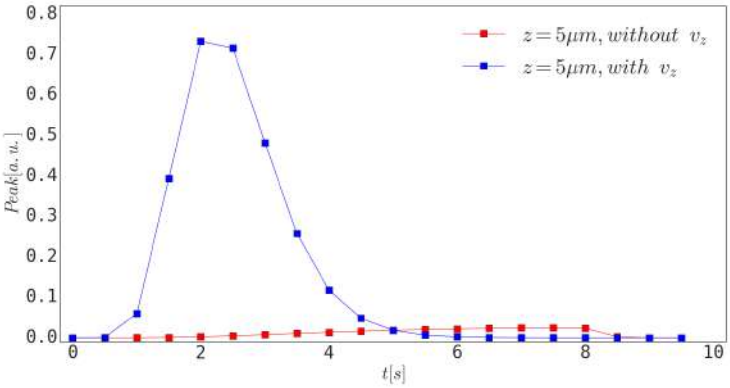

Figure 6.3: Same as before, marginalization of the 3D STICS function onto a plane of $5\,\mu m$ spatial delay in the $\hat{z}$ direction.

Two meaningful observations can be made:

1. in figure 6.2, it's apparent that the effect of a velocity component that leaves the selected plane result in a faster correlation decay: the presence of what could be called a new *decay channel* speeds up similarity loss;

2. looking at 6.3, the difference is even clearer: only in the presence of an out-of-plane velocity it's possible to observe a definite peak, informative of a drift motion.

These thoughts suggest that system simulations should probably be an important tool, since comparison with theoret-

ical data could, at the very least, reveal the possible presence of a *a priori* discarded v-component outside the investigated plane. On the other hand, when a sample clearly presents a three-dimensional $\vec{v}$ field, this method can be readily applied to a desired investigation plane, employing the simple SPIM setup without any modification.

Approximation During the previous derivation I restricted the math to resolve a fairly ideal situation, but this is rarely the case. Supplementary of the following article explains the problem quite accurately and gives a precise derivation in the most general case. Here it's sufficient to highlight that the most important differences regards illumination non-uniformity and idealization of the acquisition system. The first one can be easily included, acting on beam waist, making it different for every direction: $\omega \to \omega_x, \omega_y, \omega_z$.
For what concerns detection, images are obviously collected by a pixelated detector, which defines a last smoothing process onto the PSF. More precisely: a 2D Gaussian profile is smoothed out by a convolution with the pixel finite size a $(rect(\frac{x}{a})\, rect(\frac{y}{b}))$. As mentioned before, this should be completely negligible if pixel size is small enough to allow a sufficient sampling of the PSF peak (fulfilling Nyquist criterion), but since often this is not the case, this operation results in

a broadening of the effective PSF. Detailed derivations can be found in the article supplementary material and as an extension of Krieger et al.[35]

Here is the article (currently under revision) that presents the relevant achievements.

Spatio-temporal Image Correlation Analysis for 3D Flow Field Mapping in Microfluidic Devices.

Nicolo' G. Ceffa[$], Margaux Bouzin[$†], Laura D'Alfonso[$], Laura Sironi[$*], Cassia A. Marquezin[⌘], Ferdinando Auricchio[§], Stefania Marconi[§], Giuseppe Chirico[$#], and Maddalena Collini[$#*].

$ Dipartimento di Fisica, Centro di Nanomedicina, Università degli Studi di Milano-Bicocca, Piazza della Scienza 3, 20126, Milano (I) # CNR-ISASI, Institute of Applied Sciences & Intelligent Systems, Via Campi Flegrei 34, Pozzuoli NA (I) § Dipartimento di Ingegneria Civile e Architettura, Università degli Studi di Pavia, Pavia (I) ⌘ Instituto de Física, Universidade Federal de Goiás, Goiânia, Goiás 74.690-900, Brasil

ABSTRACT: Microfluidic devices reproducing 3D networks are particularly valuable for nanomedicine applications such as tissue engineering and active cell sorting. There is however a gap in the possibility to measure how the flow evolves in such 3D structures. We show here that it is possible to map 3D flows in complex micro-channels networks by combining wide field illumination to image correlation approaches. To this purpose we have derived the spatio-temporal image correlation analysis of time stacks of single plane illumination microscopy images. From the detailed analytical and numerical analysis of the resulting model we developed a fitting method that allows to measure, besides the in-plane velocity, the out-of-plane velocity component down to $v_z \cong 65$ μm/s. We have applied successfully this method to the 3D reconstruction of flows in micro-channel networks with planar and 3D ramifications. These different network architectures have been realized by exploiting the great prototyping ability of a 3D printer, whose precision can reach few tens of micrometers, coupled to poly-di-methyl-siloxane soft printing lithography.

Microfluidics has a large impact in nanomedicine: diagnostic devices[1] for cell screening and separation[2], methods for enhancing cell-tissue interactions[3] or for cell growth in scaffolds for tissue engineering[4], are only a few examples. The combination of microfluidics with molecular and cellular diagnostics reduces the sample volume and the waste of sample, maximizes the information and allows scalability for screening applications and batch sample processing. Microfluidics also allows to study the 3D cellular microenvironment in a controlled manner. The advantage of 3D platforms is well recognized and ranges from tumor in-vitro models[4,1], to tissue engineering or stem cells harvesting[5-6]. These novel microfluidic techniques require the development of analysis methods for flow field mapping in 3D and the possibility to test many different network designs.

μPIV (Particle Image Velocimetry) in 2D and single particle tracking[0a,0b] have been extended to 3D via stereoscopy, defocusing and digital holography[0a]. Starting from a different approach, we couple concepts from image cross-correlation microscopy to wide field Single Plane Illumination Microscopy (SPIM): we map 3D flows by exploiting the amplitude decorrelation measured on 2D time-stack of images. By working on the very same SPIM microscope used for studying morphology of organisms[7,15] or of microchannels[8,10], with no need to exploit aberrations or stereoscopy, we analyze the time-stacks by correlation methods[9-10]. Time autocorrelation methods have been widely applied to the study of the dynamics of biomolecules in-vitro[11] and in cells[12,13-14] and to finely map flows in microfluidic devices also coupled to PIV[0c]. μPIV maps 2D flows[0d] by exploiting cross-correlation between two subsequent imag-

es or within multiple exposure images. Cross-correlation dual–spot approach has been also recently applied to the study of in-plane blood flow[15], and its generalization to multiple spots led to the so called Space Time Image Correlation Spectroscopy (STICS).[16] When a flow is present, the displacement of the position of maximum of the space-time correlation map from the center of the correlation space, provides a measure of the in-plane flow velocity. We measure here the out-of-plane motion by following the loss of the amplitude of the STICS map, due to objects passing through the illumination plane, without resorting to defocus or complex stereoscopy setups.

We have exploited Material Jetting technology[17,18] to test our approach on a variety of 3D microfluidic designs. The advantage of using 3D printers is twofold[19]. The unprecedented ability (1) to fabricate in three dimensions, creating complex geometries than cannot be produced at low cost through standard subtraction technologies and (2) the high resolution (few tens of micrometers in layer thickness) which is already at the limit of the molding fidelity of poly-di-methyl-siloxane (PDMS) soft lithography. 3D printing technology can process many different materials, from photopolymers to metal powders, to biocompatible materials. It can be used for prototyping 3D structures for cellular culturing (tissue engineering) and in-vitro cell models, in alternative to more advanced techniques such as two-photon photopolymerization[4]. Moreover, the ability to rapidly realize a model enables us to adopt a "trial and error" strategy. A simple micro-fluidic microchip can be printed in about 1 hour and then used to mold several PDMS replicas of the network. We test that the surface roughness, due to the thickness of the individual deposited resin layer, induces no dramatic aberrations on the laser sheet of the SPIM setup. The goal of our report is therefore to develop an algorithm to map flow fields in 3D by exploiting STICS analysis of time stacks of SPIM images taken at different depths in the microchannel structures. SPIM methods have been applied to developmental biology on embryos,[20-22] coupled to time correlation methods to study biomolecular dynamics in cells on single[23-24] and dual colors acquisitions.[25] We have recently used SPIM to characterize time varying flows in micro-channels[10]. However, we are not aware of any attempt of its employ to characterize in 3D a flow field. We develop here the formalism for the STICS analysis SPIM images. From the analytical and numerical study of the resulting correlation image we have derived and tested a fitting algorithm that allows us to measure the out-of-plane component of the velocity from the decay of the correlation amplitude as a function of the lagtime. The lower limit of out-of-plane velocity detection for our setup is $v_z \cong 65$ μm. The upper boundary is instead determined by the image sampling frequency and the thickness of the SPIM sheet. We believe that this method, applied here to the 3D mapping of the flow in micro-channels, could also be employed to analyze vessels in vivo.

THEORY

We implement a 3D analysis of the flow that exploits the time evolution of both the position and the amplitude of the maximum of the STICS cross-correlation image. We define the SPIM plane as the x-y plane and allow the flow speed $\vec{v} = (v_x, v_y, v_z)$ to have an out-of-plane component $v_z \neq 0$. In order to compare the in-plane and out-of-plane components we also define $v_{xy} = \sqrt{v_x^2 + v_y^2}$. The dual spot cross-correlation as implemented on a SPIM setup, is based on the analysis of the cross-correlation between two pixels or Regions of Interest (ROI) in the illumination plane as a function of the lagtime[9,15]. As shown in detail in the Supporting Information, section SI.1, the out-of-plane velocity component has an effect on the maximum lagtime (Fig.S1A), on the amplitude (Fig.S1A inset) and on the width of the cross-correlation function (Fig.S1B). However, the effect can be partly mitigated by changing the spot-spot distance, suggesting that the experimental measurement of all the velocity components should be performed on a multiple spot-spot distance basis. This is obviously possible once we have acquired a full time stack of images on the SPIM setup, and suggests us to develop a global spatio-temporal analysis.

The spatio-temporal cross correlation image (STICS image) is defined for a time stack of images:

$$C(\xi,\eta,\tau)=\frac{\langle \delta I(x,y,t)\delta I(x+\xi,y+\eta,t+\tau)\rangle_{x,y,t}}{\langle I(x,y,t)\rangle^2_{x,y,t}} \qquad (1)$$

where (ξ, η) and τ are the spatial and time lags, respectively. In Eq.1 the time stack of images {I(x,y,t)} is acquired over a field of view of size X × Y (typically 200 μm × 600 μm) and for a maximum time T = M δt (M samplings with image sampling time = δt). The fluctuations are computed with respect to the time average on each pixel, $\delta I(x,y,t)=I(x,y,t)-\langle I(x,y,t)\rangle_t$. Following the outline given by Krieger 2015 et al.[9] as described in the Supporting Information (SI.2) for finite size of the tracers,[26] we have derived the expression of the Gaussian-like shaped spatio-temporal cross-correlation function C(ξ,η,τ). The maximum of the function (ξ_{max},η_{max}) displaces from the center of the correlation space linearly with the lagtime according to the in-plane flow velocity (SI.3):

$$\sqrt{\xi_{max}^2+\eta_{max}^2}=\tau\sqrt{v_x^2+v_y^2}=\tau v_{xy} \qquad (2)$$

and its position does not depend on the out-of-plane speed component nor on the pixel size. The width of the correlation function peak can be measured from the second moment of the correlation function as derived in detail in Section SI.3 and can be written as:

$$\omega^2=\frac{\sqrt{\pi}}{2}M(\omega_{xy},D,\tau)\frac{\left[aErf(\beta)+\frac{M(\omega_{xy},D,\tau)}{\sqrt{\pi}}\left(\exp(-\beta^2)-1\right)\right]}{\left[1-\exp(-\beta^2)\right]} \qquad (3)$$

where D is the diffusion coefficient, ω_{xy} is the radial beam waist, $M(\omega_{xy},D,\tau)=\sqrt{\omega_{xy}^2+4D\tau}$ and $\beta=a/M(\omega_{xy},D,\tau)$ is a measure of the pixel size a in terms of the diffusion range. As detailed in the SI.3, a linear trend $\omega^2\cong constant+4D\tau$ is sufficient to analyze the experimental data.

Cross-correlation amplitude. The lagtime dependence of the amplitude of the STICS image contains information on the in-plane diffusion and the out-of-plane drift. For $v_z = 0$ the area of the ξ or η profile of the CCF should be constant and the amplitude should decrease slowly with time as the width increases due to Brownian motion. This occurs over lagtimes of the order of $\tau_{xy}=\omega_{xy}^2/4D \cong 0.12$ - 0.41 s (0.3 μm²/s ≤ D ≤ 1.0 μm²/s) and it is approximately described by a slow hyperbolic decay (see Eq.S19 and Figs. S2 and S7):

$$C_{i,max}(\tau)\big|_{i=x,y}\cong\left(1+\frac{\tau}{\tau_{xy}}\right)^{-1/2} \qquad (4)$$

as expected from the fluorescence correlation spectroscopy theory[12] for a 1D Brownian motion. The dependence on the pixel size appears at the second order in the ratio $\beta_0 = a/\omega_{xy}$ (see Eq. S20), and is negligible unless for very low magnification.

The out-of-plane motion contributes with a Gaussian term (see Eq.S12 and Eq.S22) and altogether we can write the maximum of the STICS image as

$$C(\xi_{max},\eta_{max},\tau)\propto\frac{\omega_z}{M_z}\exp\left[-\left(\frac{v_z\tau}{M_z}\right)^2\right]\left[Erf(\beta)+\frac{\left(\exp(-\beta^2)-1\right)}{\beta\sqrt{\pi}}\right]^2 \qquad (5)$$

where ω_z is the sheet thickness and $M_z=M(\omega_{xy},D,\tau)v_z$. It is also useful to define $\tau_{vz}=M_z/v_z$ and $\tau_z=\omega_z^2/4D$.

From the functional dependence reported in Eq.5 is also evident that we are sensitive only to the absolute value of the out-of-plane drift component of the velocity. As detailed in SI.3, the contribution of the out-of-plane diffusion is negligible when compared to in-plane diffusion and to out-of-plane drift time. On the other hand, the amplitude of the STICS image is largely affected by the out-of-plane flow. In general, the lower is the diffusion coefficient D and the larger is the out-of-plane velocity, the easier is to single out the contribution of the out-of-plane drift. As an extreme case, for out-of-plane drift velocities as small as $v_z \cong 50$ μm/s, and large diffusion coefficient ($\tau_{xy} \cong$ 0.12s) the out-of-plane drift contribution to the STICS amplitude is only 5% when the in-plane diffusion contribution has already dropped at 50%. Both contributions to the amplitude decay must then be accurately fitted to Eq.5 in order to correctly evaluate the out-of-plane drift component.

Limits on the out-of-plane velocity detection. The upper limit for the detection of the out-of-plane drift velocity, v_z, is determined by the image sampling time, $\delta\tau$. The maximum detectable speed is set by requiring that at least four sampling points fall within $\sqrt{2}\tau_w$, leading to the detection limit $v_z \leq (\sqrt{2}/4)(\omega_z/\delta\tau) \cong 320 - 220$ μm/s for $\delta\tau$ = 13 - 19 ms and $\omega_z \cong 12$μm, as employed here (see also SI.3 and SI.6). On the other hand, as v_z decreases, τ_{vz} increases up to match the in-plane diffusion time τ_{xy}. The minimum measurable value of v_z can then be found by requiring that the out-of-plane drift contribution to the amplitude has decreased of at least 50% for a lagtime $\cong \tau_{xy}$, similarly to the in-plane diffusion component. For $\tau_{xy} \cong 0.12$ s (the worst case here) we find in this way a minimum detectable value of $v_z \geq (\ln(2))^{0.5}\omega_z / \tau_{xy} \cong 83$ μm/s and $v_z \geq 65$ μm/s for the most typical value τ_{xy} = 0.15 s.

EXPERIMENTAL SECTION

SPIM setup. The laser source of the SPIM setup[27] was an air-cooled argon−krypton laser (Melles Griot, Carlsbad, CA) adapted from a confocal setup. The proper excitation wavelength was selected by a band-pass filter. The beam was expanded 1:4 and focused into the back aperture of an illumination objective (Olympus 4×, 0.1 N.A.) by means of a cylindrical plano-convex lens (f_{cyl} = 50 mm). The fluorescence emission was detected through a 20x, water immersion Olympus objective (XLUMPlanFl, 0.95 NA) mounted at right angle (along the z-direction) with respect to the illumination plane which lies in the laboratory horizontal plane (x-y plane). The emission was collected by an EMCCD detector (Cascade II, Photometrics, USA) through a tube lens with an effective M=20 magnification on the final image. The typical acquisition rates were 13 - 19 ms/frame, on field of view of hundreds of micrometers in size, typically (Fig.S0A).

Microfluidic Setups. The piston (1 mm diameter) of a 500 μL Hamilton micro- syringe is coupled to a linear actuator (M227-C863 linear actuator, Phyisk Instrumente, D) to generate the flow (speed resolution 50 nm/s). Fluorescent orange amine-modified polystyrene, latex beads, 1 μm diameter, from Sigma (Sigma-Aldrich Chemical Co.) have been used as tracers. The aqueous solution of microbeads was sonicated for 30 minutes before use. The microbeads suspension velocities were kept constant in time and varied according to the piston step rate.

The microfluidic device was built by casting PDMS (Dow, Corning, USA) in 3D printed molds whose 3D sketches are shown in Fig.S0B,C,D. The final virtual model of the three molds was exported as STL (Standard Triangulation Language) file and prototyped (Fig.S0E). 3D printing was performed through an Object 30 Pro (Object-Stratasys) based on Material Jetting technology, using a transparent photopolymer (Veroclear™). The printer features a layer thickness of 16 μm and a in-plane resolution of 600x600 dpi, with an overall accuracy of 0.1mm. The PDMS was poured in the molds and after the polymerization the PDMS layer was peeled off and pressed on a glass slide (170 μm thickness) that becomes the fourth wall of the micro-channels, acting as the observation window and defining the x-y plane (the y direction is the structure symmetry axis). The sealing was ensured by thermal annealing for 60 minutes at 180 degrees. In order to reduce the excitation beam scattering, the PDMS thickness on the excitation side was reduced to a maximum of 2 mm and a glass slide was used as outer surface facing the excitation beam. In this way the entrance PDMS wall for the illumination plane was close to optical flatness. The microchannel shape and cross-sections were reproduced with high fidelity from the mold as shown by fluorescence microscopy imaging of the channels filled with Rhodamine solutions (see Fig.S19, Section SI.7). The PDMS microchannels were connected to the glass syringes (employed as pump and reservoir) by silicone tubes (1 mm × 3 mm).

Three geometries were built. An Y-shaped structure with a constant area square cross-section was used to explore 2D flow patterns. In this way the average flow speed does not change far from Y-shaped junction (Fig.S0B). 3D flow patterns were instead produced in two other structures: a straight microchannel with a telescopic variation of the cross-section (Fig.S0C) at three transition regions. At each of the transitions the cross-section area increases four times, from 200x200 μm^2, to 400x400 μm^2, to 800x800 μm^2. The cross-section was not symmetrically expanded in the x-z plane and we expect that this asymmetry will induce a flow component in the z direction.

In a second straight microchannel we built two separate but consecutive chambers each expand-

ing in either the x or z direction (Fig.S0D). In this structure we expect to observe out-of-plane motion (along the z direction) only for the chamber expanding in the z direction.

STICS images analysis. The STICS images were computed on a time stack of M images $S=\{I_j\}_{j=0,..M}$ taken at M times spaced by δt ranging typically from 13 to 19 ms (corresponding to 74 to 52 frame per second of the EMCCD, the fastest rates compatible with the chosen field of view). Each image has a size of X×Y pixels. The correlation function was computed by the FFT algorithm:

$$G(\xi,\eta;k\cdot\delta t)=(M-k)^{-1}\sum_{j=0}^{M-k}FFT^{-1}\left[FFT(I_j)FFT^{*}(I_{j+k})\right] \quad (6)$$

Each image of the time stack was padded with zeros up to double its size before performing the FFT and each correlation image was then normalized for the lag-space.

On each correlation image, corresponding to the lagtime τ, we automatically selected the position (ξ_{max},η_{max}) of the maximum by fitting the image to a 2D Gaussian profile (see Fig.S3, Section SI.4). The amplitude of the STICS function was derived from the amplitude of the Gaussian fit function, subtracted for the possible background. In order to evaluate the z component of the flow velocity we need to follow the amplitude of the STICS image with the lagtime over at least 5-10 lagtime points, up to a lagtime τ_{fit}. Since we would like to map the flow as finely as possible we have computed the STICS image on rectangular ROIs elongated in the direction of the flow in order to be able to follow the maximum of the STICS image in the whole lagtime range. We have checked that the condition to recover the STICS amplitude is that the ROI size is at least ≅ 2 v_{xy} τ_{fit}. For a flow of the order 400 μm/s and τ_{fit} ≅ 40 ms, this corresponds to a size of 16 μm, or at least 20 pixels (see Section SI.5)

RESULTS AND DISCUSSION

In-plane flow field mapping. We have first characterized the flow field in the Y-shaped structure (see Fig.1A, sketch). In this case, we do not expect any substantial out-of-plane component and we focus on the study of the flow speed in the x, y plane. To this purpose we measure the position $P_{max}=(\xi_{max},\eta_{max})$ of the maximum of the STICS correlation function as a function of the lagtime, τ. The flow speed in the x and y direction, v_x and v_y (see Fig.S4, S5), are then measured from the corresponding slopes of ξ_{max} and η_{max}. As shown in the section SI.3, the measurement of the in-plane velocity is poorly affected by the pixel size (< 4% for a ≤ 3.2μm) or by the out-of-plane speed (< 3% for v_z ≤ 320 μm/s) components (see Fig.S5). As an example, we selected two Fields of View, FOV1 in the secondary arm (Fig.1A, sketch) and FOV6 in the lower half of the junction (Fig.1B, sketch). On each of them a time stack of about 200 images was analyzed (>10 s acquisition time) and the STICS correlation function computed on a 7×7 array of ROIs, fully covering the field of view. The average flow direction can be gained from the maximum projection of the collected time stacks. As can be judged from Fig.1C the direction of the flow is quite uniform on FOV1, which is far from the junction, and smoothly bent downwards in FOV6 (Fig.1D). This qualitative observation is fully consistent with the quantification reported in Fig.1A and Fig.1B. For the case of FOV1, the angle between the flow speed and the x axis is pretty constant when moving along the x and the y directions (Fig.1A, inset), θ = 25.5° ± 0.6°. The change in the |v| along the x axis can be ascribed to the sticky boundary conditions: due to the orientation of the image with respect to the flow, the origin of the x coordinate axis corresponds approximately with the channel axis. Similar results, but with reduced velocity values, are found for the motion along the y axis, due to the angle between the flow and the y-axis of the image. This picture is fully consistent with the microchannel structure as obtained by the 3D printer (θ = 25.6°, see Fig.S0B). The case of FOV6 is more complex. When studying the flow speed along the x axis we measure a negligible v_x component, slowly increasing in amplitude at larger y values. This is in agreement with the projected image (Fig.1D) from which we can see that the flow is predominantly along the y axis unless at very high y values. For the data reported in Fig.1B (right panel, corresponding to the central ROI n.3) an average value of the angle θ ≅ 6 ± 2 ° along y-axis is measured. Along the x-axis the flow direction changes significantly (Fig.1B, left panel, see white, black and gray symbols) as can be judged from the analysis of the

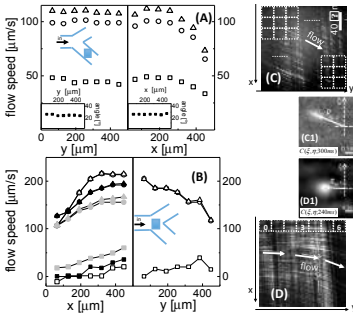

Figure 1. Characterization of the in-plane flow field in the Y-shaped structure. Two relevant FOVs were selected along a secondary arm (FOV n.1, panels A, C) and in the lower half of the Y-junction (FOV n. 6, panel B, D). On each of the two FOVs we computed the STICS correlation function on 49 square, equally-spaced ROIs (7x7 matrix). Panel A and B report the v_x (squares) and v_y (circles) components and the modulus |v| (triangles), as a function of the coordinate along the y or x direction. The insets in panel A reports the angle $\theta = \arctan(v_y/v_x)$ of the flow speed with respect to the x direction. Along each of the axes we selected the middle ROI (ROI = 3) for the analysis but for the left plot in panel B where the result of the analysis performed on three selected ROIs (0, 3, 6) are reported as white ($\theta = 2 \pm 2^o$), black (8 ± 2^o) and gray (14 ± 4^o) squares, respectively. Panels C and D report the maximum signal projection of the FOV n.1 (C) and FOV n.6 (D). Some of the ROIs on which the STICS images were computed are indicated as dotted squares on the images. The gray vectors superimposed to the images indicate the flow direction as measured from the θ angle. Frame rate 74 fps, 512x512 images, time stacks slices = 200. The images in the blow-ups of panels C and D, are the STICS correlation images for the lagtimes 300 ms (C) and 240 ms (D), respectively.

x-profile for 3 ROIs, at the edges and in the middle of the FOV. In this case we measure indeed a systematic change in the flow angle with respect to the x-axis, starting from $\theta \cong 2^o$ at one edge (ROI n.0) of the FOV6 down to 14^o at the opposite edge (ROI n.6). We can conclude that the STICS analysis applied to time stacks of images collected in SPIM mode allows us to quantitatively and fully characterize complex spatial flow patterns in the SPIM plane. Since each sub-ROI can be ≅ 50 µm in size, the velocity fields can be mapped with tens of micrometers resolution. The effect of the number of frames on the evaluation of the 2D flow velocity is analyzed in the SI.5 section.

The STICS amplitude measures the out-of-plane flow velocity. We have investigated the possibility to employ STICS analysis on SPIM images to measure flows in 3D on two different microstructures in which the cross-section changes in the x and z direction or in the z direction alone (the SPIM plane is parallel to the x-y plane). The first case is obtained by means of a telescopic straight structure opening up both in the x and z directions (Fig.S0C). We first studied the flow in the 800 µm cross-section segment of this microchannel (Fig.S0C, region "a"). Here we expect pure 2D flow in the SPIM plane and the amplitude of the STICS correlation function should decay only as an effect of the diffusive motion. This is indeed the case as shown in Fig.2 (open symbols). The 40% decrease measured at lagtimes ≅ 0.45s is compatible with the small diffusion coefficient of the tracers ($D \cong 0.4\ \mu m^2/s$). The dashed line represents the best fit of these data to Eq.5 when setting $v_z = 0$. The value of the diffusion coefficient is confirmed by the linear fit ($\omega^2 \cong$ constant + $4D\tau$) of the STICS peak width as a function of the lagtime (Fig.2, inset open squares) that provides the best fit value $D = 0.42 \pm 0.06\ \mu m^2/s$. In order to investigate the telescopic transition region, we have acquired a central plane in the transition region "b" (see Fig.S0C) between the 800 µm to 400 µm side cross-sections. In the x direction the section widens from -200 µm ≤ x ≤ +200µm to -400 µm ≤ x ≤ 400 µm, symmetrically in the positive and negative directions, whereas along z direction it widens from 0 µm ≤ z ≤ 400 µm to 0 µm ≤ z≤ 800 µm, since we are limited by the bottom glass slide. The STICS correlation function shows a marked decrease (up to 80%) of its amplitude

(filled symbols, Fig.2) whose fit to Eq.5 provides a value $v_z = 120 \pm 3$ μm/s for the out-of-plane velocity component (Fig.2, solid line). The squared width, ω^2, of the STICS function increases linearly with the lagtime similarly to the straight microchannel case (Fig.2, inset). This confirms that this parameter is not sensitive to the flow speed. From a linear fit we obtain $D \cong 0.4 \pm 0.1$ μm^2/s , in very good agreement with the expected value, $D \cong 0.4$ μm^2/s, for 1 μm size microbeads.

In order to test the reliability of the measurement of the out-of-plane component of the velocity from the STICS amplitude decay, we have modified purposely the out-of-plane velocity component by rotating the SPIM plane around the x axis. The SPIM plane was set at the "b" region (Fig.S0C) 400μm - 800μm telescopic transition (300 μm from the bottom glass slide). Time stacks of images were then acquired at two different orientations of the SPIM plane, $\theta_x = +9 \pm 1^o$ and $\theta_x = -9 \pm 1^o$, obtained by rotating the cylindrical lens in the SPIM set-up. An example of the effect of the orientation on the STICS amplitude is reported in Fig. 3, where the rotation of the SPIM plane with respect to the flow velocity is also sketched. As the SPIM plane orientation departs from the flow direction, the out-of-plane component of the velocity increases and the decrease of the STICS amplitude as a function of the lagtime is more pronounced. This case corresponds to the best fit out-of-plane velocity $v_z(\theta_x=0^o) = 157 \pm 7$ μm/s (filled symbols) and $v_z(\theta_x=9^o) = 193 \pm 17$ μm/s (open symbols). The rotation angle of the SPIM plane can be estimated as $\theta_x \cong (v_z^{out} - v_z)/v_y$ and amounts to $\theta_x = 9 \pm 4^o$, in good agreement with the expected 9 ± 1^o.

STICS amplitude-lagtime plot allows to map the out-of-plane flow in 3D. As a second test of the possibility to evaluate the detailed behavior of the out-of-plane velocity component of the flow we have acquired 12 time stacks (each consisting of 150 images, sampling time 19.2 ms) at different heights covering a volume of approximately 819 μm x 410 μm x 120 μm, at the transition between the 800 μm to 400 μm cross-section side.

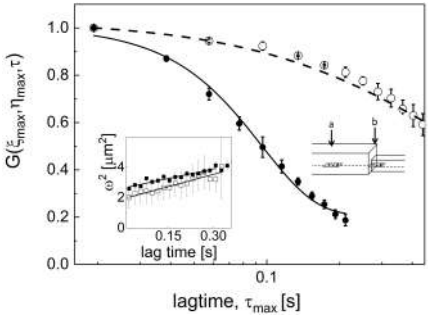

Figure 2. STICS amplitude at the cross-correlation maximum as a function of the lagtime τ_{max}. The open and filled symbols refer respectively to the STICS amplitude computed on time stacks of images of microbeads flowing in the straight 800 μm section (section "a" in Fig.S0C) and at the 400 μm - 800 μm (section "b" in Fig.S0C) transition in the telescopic microchannel (height ≅ 160 μm from the glass slide). The solid lines are the best fit to the data according to Eq.5 with pixel size a = 0.8 μm (in the sample plane), PSF size $\omega_{xy} = 0.6$ μm, SPIM sheet size $\omega_z = 12$ μm. The best fit value of the diffusion coefficient is $D = 0.22 \pm 0.05$ μm^2/s and $v_z = 0$ (open symbols) and $v_z = 120$ +/- 3 μm/s (filled symbols). The inset shows the trend of the width, in μm^2, of the correlation function as a function of the lagtime. The solid line is the best linear fit to $\omega^2 \cong$ constant + $4D\tau$,with best fit values $D = 0.42 \pm 0.06$ μm^2/s (open symbols) and $D = 0.4 \pm 0.1$ μm^2/s (filled symbols).

The bottom of the reconstructed volume (x-y planes with lowest value of z) lies at about 160 μm from the glass slide (see sketch in Fig.4A), which is taken as the origin of the z axis. The STICS correlation functions were computed for a maximum lagtime of 364 ms, therefore allowing a reasonable statistical average. In order to map the flow we have computed the STICS correlation image on ROIs 50x200 pixels (40 μm x 160 μm) in size. Given the average speed, mainly along the y axis ($v_y \cong 150$ μm/s) the maximum of the STICS function displaces of about 54 μm along the y axis, well within the

size of the ROI. We have displaced the ROIs in such a way to cover all the field of view without super-positions (Section SI.5 and SI.6). The first evidence is that the flow occurs out of the SPIM plane. The 3D reconstruction of the flow sampled at four locations in the detected volume (Fig.4A), indicates that the flow occurs also in the z direction at the transition between the small to large cross-sections. At the same time, the speed modulus decreases since the volumetric rate remains constant (Fig.4A, red to blue transition in color codes). The v_z component slightly decreases along the flow (y) axis (Fig.4C): a smooth systematic decrease from $v_z \cong 300$ µm/s at y≅0 µm to $v_z \cong 200$ µm/s at y ≅ 200 µm can be singled out only for x ≅ 450 µm (Fig.4C, filled squares). The v_z component has also a slight dependence on the distance from the bottom glass-slide (Fig.4B): the maximum value of v_z (at x ≅ 380-430 µm) changes from $v_z \cong 350 \pm 30$ µm/s at z ≅ 30 µm to $v_z \cong 400 \pm 30$ µm/s at z ≅ 160 µm.

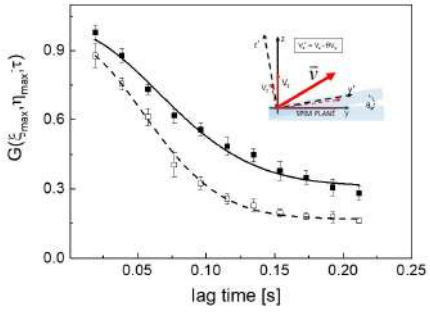

Figure 3. STICS amplitude is sentistive to the out-of-plane velocity component. The data were collected from microbeads flowing at the 400 µm - 800 µm telescopic transition in a telescopic microchannel at the height ≅ 300 µm from the glass slide. The filled and open symbols refer to the control case of the SPIM plane oriented parallel to the glass coverslide ($\theta_x = 0^o$) and to the case of the SPIM plane rotated around the x axis of an angle $\theta_x = +9 \pm 1^o$. The average speed in the SPIM plane (measured at $\theta_x = 0^o$) is $v_{xy} = 225 \pm 23$ µm/s. The STICS amplitude decays are fit to Eq.5 with D=0.4 $\mu m^2/s$, $\omega_z = 12$ µm, $\omega_{xy} = 0.6$ µm and a = 0.8 µm. The best fit relaxation times were $\tau_{vz} = 76 \pm 3$ ms (solid line, $\theta_x = 0^o$) and $\tau_{vz} = 62 \pm 6$ ms (dashed line, $\theta_x = +9^o$). A small amplitude relaxation with long relaxation $\tau_{vz} > 290 \pm 100$ ms was necessary to fit the longest relaxation times. The inset sketches the experimental orientation of the SPIM plane in the two configurations.

The v_y component (Fig.4D) has instead a clear parabolic behavior as a function of the x-direction (perpendicular to the flow direction) with a maximum position that matches that of the v_z maximum (Fig.4B). Moreover, the maximum amplitude of v_y decreases as a function of the distance from the transition region (Fig.4D), as expected due to the increase of the microchannel cross-section. The x component of the velocity, v_x, inverts its sign at positions close to the flow axis (x ≅ 400 µm) for all the y coordinates values (Fig.4E). This is an indication of the fact that the flow opens up in the x direction when passing from the 400 µm to the 800 µm cross-sections. However, we also expect that the v_x component is decreasing in amplitude when approaching the side walls of the microchannel, resulting in a maximum and minimum symmetrically located with respect to the flow axis. The roll-off behavior observed for v_x at x ≅ 600 µm (and presumably at x ≅ 200 µm) in Fig.4E is an indication of such a trend. Since the v_z component (Fig.4B-C) does not show a clear dependence upon the x and y directions,, we have built a capillary with a square cross-section (500µm x 500µm) that undergoes a four-fold transition along the z axis (see Fig.S0D and the sketch in Fig.5A). In this case the flow opens up mainly along the z axis, resulting in a net decrease of the speed modulus (see Fig.5A for a 3D view).

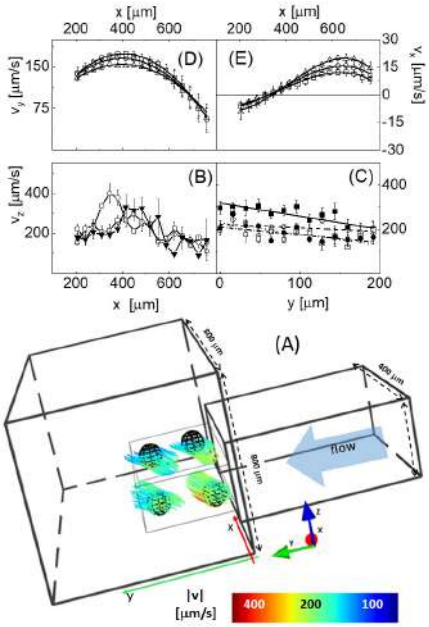

Figure 4. Flow analysis at the 400 μm - 800 μm transition of the telescopic microchannel. Panel A sketches the microchannel (thick black lines) and delineates the 3D volume (thin line box, 12 time stacks 512x1024 pixels each, 150 frames each) in which the flow is reconstructed from the analysis of the STICS maps (ROIs 50x200 pixels in size, lagtime: 12 ms - 265 ms). The field is sampled at four regions (spheres). Panel B shows the trend of the v_z component of the flow along the x axis. The data were averaged on the z ranges 0-60 μm (open squares), 60-120 μm (filled triangles) and 120-180 μm (open circles) and over the first three y positions y = 0, 16 and 32 μm. Panel C reports the v_z component of the flow along the y axis for different position across the channel (averaged on the z range 0-180 μm); x = 215 μm (open circles), x = 455 μm (filled squares), x = 695 μm (open squares) and x = 815 μm (filled circles), together with linear fit to the data. Panels D, E show the v_y (D) and v_x (E) components of the velocity as a function of the x coordinate (a correction for the flow/CCD alignment,φ = +0.1rad, was applied, as in Fig.5D2). The data were averaged on the whole z range 0-180 μm. Symbols code: y = 0 μm (squares), y = 100 μm (circles) and y = 240 μm (triangles). The solid lines are best fit to a parabolic function (D) and cubic function (E) to the data, shown to guide the eye.

Far from the transition downstream (y ≅250 μm, Fig.5B) or moving towards the top of the wider chamber (z ≅ 120 μm, Fig.5B) the speed decreases at values ≅ 150 ± 40 μm/s and 80 ± 35 μm/s, respectively. By comparing these values to the maximum value measured before the transition, |v| = 300± 35 μm/s, we can estimate a decrease of the speed of about 3-4 times, as it is expected from the capillary geometry. It is noteworthy that this value is also close to the maximum speed measured on the x-z plane at y = 0 μm (Fig.5C). Due to the pronounced spatial dependence of the speed, the out-of-plane motion can be better estimated by computing the projection angle of the velocity onto the x-plane, $\theta_z \cong v_z / v_{xy}$. From the contour plots reported in Fig.5B we can estimate a maximum angle θ_z ≅ 70°. On the bottom of the channel the angle θ_z is spatially non uniform, being higher closer to the channel transition and lowering to about 15° at y ≅ 200 μm from the transition. Increasing the distance from the bottom and measuring the velocity at one fifth (z≅80 μm) of the microchannel transition, the in-homogeneity pattern shifts to higher y values and we measure lower θ_z values closer to the transition than at y ≅ 200 μm. By increasing further the distance from the bottom, z ≅ 125 μm we find again an uniform distribution of θ_z, with an average value θ_z = 60° ± 12°.

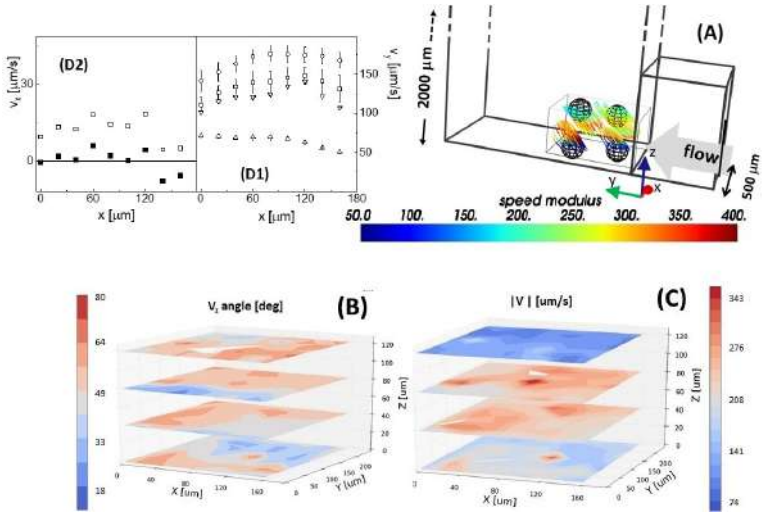

Figure 5. Summary of the 3D analysis of the flow of microbeads at the junction between two rectilinear capillaries with rectangular cross-section (z-x plane) and a four-fold increase of the height (z-axis) of the capillary. Panel A reports a sketch of the capillary and the flow lines sampled at four locations. Panel B reports the contour plots of the out-of-plane angle θ_z computed on four x-y planes. Panel C reports the contour plots of the speed modulus computed on four x-y planes. Panel D1: velocity along the y axis (the direction of the flow) as a function of the position along the perpendicular to the flow direction (x axis), measured at y=5 μm from the cross-section transition along the y axis. The symbols refer to different positions on the z axis, 5-40 μm (circles), 50-90 μm (squares) and 100-120μm (up-triangles). The down-triangles correspond to the v_y component measured at z = 120 μm. The filled down-triangles, almost superimposed to the open symbols, are data corrected for a -0.1 rad rotation of the plane). The position of the microchannel axis is x = 90 μm. The panel D2 shows the trend of the v_x (open squares) as a function of the x coordinate at z = 120 μm. The filled symbols refer to the v_x data corrected for a flow rotation in the x-y plane of about -0.1 rad.

The amplitude of the velocity along the flow axis, v_y, is much less dependent on the x coordinate in this case, as can be judged by comparing Fig.5D1 with Fig.4D. We detect a maximum in v_y at x ≅ 100 μm only for the planes that are closer to the bottom glass slide (z ≅ 20μm, circles in Fig.5D1). Finally, we notice that the x component of the speed does not show an odd symmetry with respect to the capillary axis (Fig.5D2, open symbols), contrary to the symmetric telescopic transition (Fig. 4E). Indeed, the observed trend of v_x as a function of x is due to a slight angular offset between the microchannel axis (or flow direction) and the axes of the CCD image. In fact by rotating the flow ($v_x^{rot} = \cos\varphi v_x - \sin\varphi v_y$; $v_y^{rot} = \cos\varphi v_y + \sin\varphi v_x$; φ = -0.1 rad) we obtain a uniform value v_x ≅ 0 μm/s (Fig.5D2, filled squares).

CONCLUSION

We have coupled time resolved SPIM imaging to STICS analysis in order to accurately map in 3D flow fields. We have derived the full correlation STICS image for a SPIM setup and validated an algorithm to measure the flow velocity

in the three dimensions, identifying the STICS image amplitude as a good indicator of out-of-plane drift velocity component. Our approach exploits the thickness of the SPIM sheet that induces a loss of correlation amplitude due to the tracer objects exiting from the observation volume. The in-plane drift has no effect on the amplitude of the correlation image. The Brownian diffusion and the out-of-plane drift induce instead a measurable decrease of the STICS image amplitude measured at its maximum. By choosing a suitable thickness for the SPIM sheet, we are able to measure the out-of-plane velocity component in a wide range of values ($50\ \mu m/s \leq v_z \leq 400\ \mu m/s$).

We have tested the efficacy of the analysis by mapping the flow velocity in micro-channels built by PDMS molding in templates printed by a photopolymer based 3D printer.

The test of our algorithm was performed on planar, branched or telescopic structures in one or two directions perpendicular to the flow. The possibility offered by the SPIM setup to slightly tilt the illumination sheet has allowed us to further test the reliability of the proposed algorithm. An automated analysis of time stacks of images of a field of view of 1024x512 pixels in terms of ROIs 40x40 pixels in size could be performed, on a python code, in approximately 30 minutes.

SUPPORTING INFORMATION

Cad sketches of the 3D printed microfluidic channels. Limitations of the dual spot analysis in a SPIM microscope. Derivation of the SPIM-STICS correlation functions. Functional analysis of the STICS-SPIM cross-correlation. Numerical simulations of the STICS images. STICS analysis of multiple ROIs. Fluorescence microscopy imaging of the microchannels.

ACKNOWLEDGMENTS

This work was supported by Academic Funding Unimib to M.C. (2016-ATESP-0020) and to G.C. (2017-ATESP-0017).

AUTHOR INFORMATION

Corresponding Author

* E-mail: maddalena.collini@mib.infn.it and laura.sironi@unimib.it

Present Addresses

†Margaux Bouzin present address: Laboratory of Fluorescence Dynamics, University of California, Irvine, CA.

Notes

The authors declare no competing financial interest

REFERENCES

(0a) Cierpka, C.; Kaehler, C. J. *J. Visual.* 2012, 15, 1-31.
(0b) Kim H, Westerweel J, Elsinga GE. *Meas. Sci. Technol.* **2013**, 24, 024007
(0c) Gao F., Kreidermacher A., Fritsch I., Heyes C.D. *Anal. Chem.* **2013**, 85, 4414−4422
(0d) Prasad A.K. *Curr. Sci.* **2000**, 79, 51-60
(1) Sackmann, E.K.; Fulton, A.L.; Beebe, D.J. *Nature* **2014**, 507, 181-189
(2) Espulgar, W.; Aoki, W.; Ikeuchi, T.; Mita, D.; Saito, M.; Leeb, J.K.; Tamiya, E. *Lab Chip* **2015**, 15, 3572-3580.
(3) Lee, S.Y.; Ferrari, M.; Decuzzi, P. *Nanotechnology* **2009**, 20, 495101.
(4) Pavesi, A.; Adriani, G.; Tay, A.; Warkiani, M.E.; Yeap, W.H.; Wong, S.C.; Kamm, R.D. *Scientific Reports* **2016**, 6, 26584.
(5) Nava, M.M.; Raimondi, M.T.; Pietrabissa, R. *Biomech. Model. Mechanobiol* **2013**, 12, 1169-1179.
(6) Tunesi, M.; Fusco, F.; Fiordaliso, F.; Corbelli, A.; Biella, G.; Raimondi, M.T. *Frontiers in aging neuroscience* **2016**, 8, 146.
(7) Ahrens, M.B.; Orger, M.B.; Robson, D.N.; Li, J.M.; Keller, P.J. *Nature Methods* **2013**, 10, 413-420.
(8) Bruns, T.; Schickinger, S.; Schneckenburger, H. *JOVE-J. Vis. Exp.* **2014**, 90, e51993.
(9) Krieger, J.W.; Singh, A.P.; Bag, N.; Garbe, C.S.; Saunders, T.E.; Langowski, J.; Wohland T. *Nature Methods* **2015**, 10, 1948-1974.
(10) Marquezin, C.A.; Ceffa, N.G.; Cotelli, F.; Collini, M.; Sironi, L.; Chirico, G. *Anal. Chem.* **2016**, 88, 7115-7122
(11) Hess, S.T.; Huang, S.H.; Heikal, A.A.; |Webb, W.W. *Biochemistry* **2002**, 41, 697-705
(12) Schwille, P.; Haupts, U.; Maiti, S.; Webb, W.W. *Biophys. J.* **1999**, 77, 2251-2265.
(13) Magde, D.; Webb, W.W.; Elson, E.L. *Biopolymers* **1978**, 17 361-376.
(14) Elson, E.L. *Biophys. J.* **2011**, 101, 2855-2870.
(15) Pozzi, P.; Sironi, L.; D'Alfonso, L.; Bouzin, M.; Collini, M.; Chirico, G.; Pallavicini, P.; Cotelli, F.; Foglia E. *J Biomed Opt.* **2014**, 19, 067007.
(16) Hebert, B.; Costantino, S.; Wiseman, P.W. *Biophys. J.* **2005**, 88, 3601-3614.
(17) Waheed, S.; Cabot, J.M.; Macdonald, N.P.; Lewis, T.; Guijt, R.M.; Paullab, B.; Breadmore, M.C. *Lab Chip* **2016**, 16, 1993-2013.
(18) Gibson, I.; Rosen, D.W.; Stucker, B. In Additive Manufacturing Technologies. I. Gibson, D.W. Rosen and B. Stucker editors. Springer Edition, 2010, pp. 175-203.
(19) Bhattacharjee, N.; Urrios, A.; Kanga, S.; Folch, A. *Lab Chip* **2016**, 16 1720-1742.
(20) Struntz, P.; Weiss, M. *J. Phys. D: Appl. Phys.* **2016**, 49, 044002.
(21) Huisken, J.; Stainier, D.Y.R. *Development* **2009**, 136, 1963-1975.

(22) Fu, Q.; Martin, B.L.; Matus D.Q.; Gao, L. *Nature Commun.* **2016**, 7, 11088.
(23) Hedde, P.N.; Stakic, M.; Gratton, E. *Scientific Reports* **2014**, 4, 7048.
(24) Pernus, A.; Langowski, J. *PLOS ONE* **2015**, 10, e0123070.
(25) Krieger, J.W.; Singh, A.P.; Garbe, C.S.; Wohland T.; Langowski, J. *Opt. Exp.* **2014,** 22, 2358-2375.
(26) Wu, B.; Chen, Y.; Mueller, J.D. *Biophys. J.* **2008**, 94, 2800-2808.
(27) Pitrone, P.G.; Schindelin, J.; Stuyvenberg, L.; Preibisch, S.; |Weber, M.; Eliceiri, K.W.; Huisken, J.P. *Nat. Methods* **2013**, 10, 598-599.

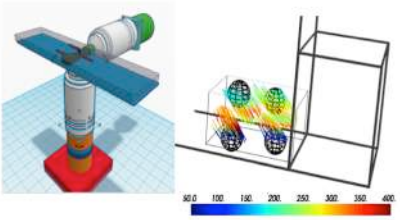

6.1 Robustness of the method

I hope that at this point it is quite convincing that all the methods presented here work perfectly fine and allow to obtain meaningful data even in complex biological samples. Nonetheless it is reasonable to raise a simple question: why all the effort? Aren't there easier or faster ways to recover the same informations that you want, e.g. blood flow fields? Well the answer is yes, there are other methods, but the one presented here is the most effective. It's useful to demonstrate this by confronting it with the other gold standard commonly employed studying velocity fields, that is particle image velocimetry[38] (PIV).

In the most emblematic realization, it can be described as a double-pulsed laser technique that generates images to measure instantaneous velocity distribution in a plane of flow, based on image correlation. Briefly, a sample containing seeding particles is illuminated and particles positions are recorded. After a short delay, a second image can be collected, and, in principle, each particle displacement could be employed to measure velocity.

PIV algorithm is often simply referred to as *particle tracking*, and it's also indicative of the first reason why ICS methods are better: trying to follow each single particle movement imposes

restriction both density and homogeneity to avoid confusion. In fact, mistaking a particle for another between two images would generate spurious velocity vectors: there is a vast literature that deals with solving this issue.[39,40] Instead, when employing ICS methods presented here, these are issues that don't even come to mind: tracers can be small particles, GUV, or red blood cells (as demonstrated in Chapter 4), and their concentration has never represented a problem (everything run remarkably smoothly even when approaching biological samples). The main reason is that there is no need to follow any single particle movement, but it's the overall behaviour inside the analysed temporal window that builds up the final result. The requirements that should be matched to obtain useful data (as already discussed in 4.1 and 5.1) don't impose any strong restriction, since high resolution is maintained along a much wider range of flow regimes than the ones expected in biological samples. Moreover the method is extremely robust with respect to $\frac{S}{N}$: once fluctuations are stronger than dark noise oscillations, then spatio-temporal similarities between signals arise naturally to create meaningful correlation plots: this is easy to see just remembering that any point in every cross-correlation based model employed is generated from an integral over a large temporal window.

For what concerns 3D extension, there are other solutions that

stem from PIV planar analysis, but for now have been proved only for macroscopic geometries. At last, it's worth mentioning a recent interesting approach, that is 4D holographic microscopy. Holography is a technique capable of retrieving 3D informations from a 2D image, thanks to interference between sample and a reference wave:[41] interference fringes can, in fact, encode three-dimensional information, and employing back propagation algorithms allows to select a specific plane to reconstruct, along the optical axis. It has been demonstrated[42] that it's possible to recover 3D positions of red blood cells for each recorded frame, but this comes with a great computational effort (more than 1hr for single sample data analysis, even employing top-end GPU units), and also abandons the specificity given by fluorescence.

Chapter 7

Conclusions

By all means let's be open-minded, but not so open-minded that our brains drop out.

Richard Dawkins

The aim of this Thesis was to develop and test correlation methods for flow mapping both in microfluidic structures and in biological samples: strong requirements have been reliability, easy data manipulation, and high speed analysis. To demonstrate this, core results are presented in the three articles:

- the first article shows how SPIM-based ICS methods can be applied both to in-vitro and in-vivo samples,

and focuses on time-series analysis: this can be considered a first step, since it's 1D, and proves that temporal resolution is high enough to sample any expected flow speed, being also extremely tolerant on trackers shape/dimensions and on $\frac{S}{N}$;

- the second article focuses on the algorithmic aspect of the research, creating a comprehensive framework, easy accessible, for performing spatio-temporal studies on biological samples, even in complex (branched vessels) geometries;

- the last article demonstrates a 3D extension of STICS analysis: it is possible to retrieve out-of-plane information even without costly setup modification, just by clever inspection of correlation functions.

The first future development that comes to mind is, of course, the application to biological samples of the last presented 3D extension. From there, two different paths could open up in my opinion: the first one consists in developing an actual 3D SPIM setup (probably introducing scanning galvanometric mirrors) to retrieve *real* 3D data, being then able to apply full three-dimensional spatio-temporal cross-correlation methods to the sample; the second direction focuses on the

study of the evolution of a specific pathology. Employing Zebrafish embryos as biological model, preliminary results show that it is in fact possible to monitor both flow speed and vessels elasticity: in particular, arterial walls thickening and loss of elasticity could result in arteriosclerosis, that could be a very serious disease. Drug testing both with a reliable biological model and with a strong, easy to use platform would represent an effective, readily useful application.

Chapter 8

Appendix

This chapter is intended as a reference for the notation and to briefly describe the building blocks employed in all the derivations. Starting from Fresnel propagation integral, I will show the basic functions and formulas that are employed in the text: the aim is to settle a common ground, since it's my experience that often the same formulas are developed with a slightly different notation, which can confuse a little bit. I found that following Gaskill[13] and Bracewell[43] is the best way to obtain a synthetic and clear exposition of paraxial wave optics. Also, at the end will be reported supplementary informations for the articles presented in the text.

Fresnel propagation

Propagation of optical fields, under the domain of scalar diffraction theory (as employed here), can be described starting from the Rayleigh-Sommerfield integral:

$$u_2(x,y) = \iint_{-\infty}^{+\infty} u_1(\alpha,\beta) \left(\frac{1}{kr_{12} - i} \right) \frac{z_{12}}{\lambda r_{12}^2} e^{ikr_{12}} \, d\alpha \, d\beta \qquad (8.1)$$

where:

1. $u_i(x,y)$ is the spatial field distibution at plane i;
2. $k = \frac{2\pi}{\lambda} n$;
3. r_{12} is the vectorial distance travelled by a single point source between the planes 1 and 2;
4. z_{12} is the distance between the two planes, projected along the propagation direction $\hat{z}$;

This integral can be simply regarded as a rigorous mathematical formulation of the Huygens principle, but it's actually pretty complicated to manipulate as it is, and often only computed solutions are obtainable. In order to simplify the model and get something more manageable, usually we put ourselves in *paraxial approximation*, that is we restrict our description

only to the propagation of fields near the optical axis, or, in practice, for little x, y values. The limit precise quantitative limits the should be respected are expressed as two *Fresnel conditions*:

- $|z_{12}| >> L_1 + L_2$, where L_i is the maximum extent of input and output signals;
- $|z_{12}|^3 >> \frac{\pi(L_1+L_2)^4}{4\lambda}$

If these conditions are met, as are throughout the work done in this thesis, then we can employ Fresnel formalism: propagation of optical fields is obtained convolving the field distribution with a propagation function, $h_{12}(x, y)$:

$$h_{12}(x, y) = B_{12}\, q\left(x, y; \frac{1}{\lambda z_{12}}\right) \tag{8.2}$$

where

- $B_{12} = \frac{e^{ikz_{12}}}{i\lambda z_{12}}$;
- $q\left(x, y; \frac{1}{\lambda z_{12}}\right) = e^{\pi i \frac{x^2+y^2}{\lambda z_{12}}}$ is the *quadratic phase signal* function.

This is the core notation carried out in this work. The following paragraphs will present examples of applications of these concepts, like lens model, 2-f, and 4-f systems.

Lens model

A lens can be simply described by its focal length, and there is a very useful and easy model to account for a lens through an optical path: via a multiplication with a (complex conjugate) quadratic phase signal. The transmission function of a lens is defined as:

$$t_l = B_l \, p_l(x, y) \, q^*(x, y; \frac{1}{\lambda f}) \tag{8.3}$$

where

- f = the effective focal length;
- B_l = optical thickness = physical thickness $\times$ refractive index (assumed constant at first approximation);
- $p(x, y)$ = aperture function that limits the extent of the transmitted wave-field.

2-f system We can then consider a particular arrangement, looking at the field propagation step-by-step.

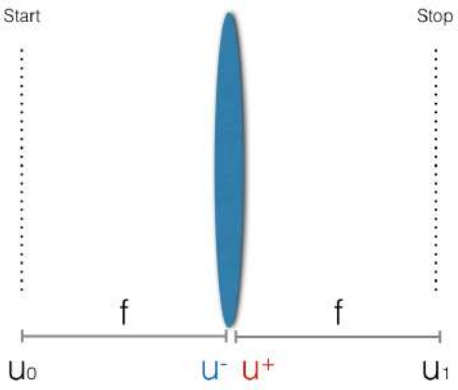

Figure 8.1: Schematic of a 2-f (single lens) system

The field $u_0(x, y)$ is propagated from the front focal plane to the lens ()convolving with a suitable propagator), than the lens impact is accounted for multiplying by the lens transmission function, and finally the result is again propagated to the rear focal plane. The mathematical steps are reported below:

$$u^{-}(x, y) = u_0 * * h_{0-}(x, y) \tag{8.4}$$

$$u^{+} = u^{-} \cdot B_l \, p_l(x, y) \, q^{*}\left(x, y; \frac{1}{\lambda f}\right) \tag{8.5}$$

$$u_1 = \left\{ [u_0 * * h_{0-}] \cdot q^{*}\left(x, y; \frac{1}{\lambda f}\right) \right\} * * h_{+2} \tag{8.6}$$

where $**$ indicates 2D convolution. Carrying out all calcula-

tions leads to:

$$u_1(x,y) = \frac{e^{2ikf}}{i\lambda f} U_0(\xi,\eta)|_{\xi=\frac{x}{\lambda f},\eta=\frac{y}{\lambda f}} \tag{8.7}$$

After all, since we are only interested in the intensity of our field (we can record only the intensity with a CCD) we can drop the constant terms in front of the integral and obtain a scaled Fourier Transform:

$$u_1 \propto U_0(\xi,\eta) = U_0\left(\frac{x}{\lambda f}, \frac{y}{\lambda f}\right) \tag{8.8}$$

8.1 Python programs

The Python programs and mathematical libraries that I wrote both for simulations and data analysis can be found in: https://goo.gl/Vmhzgm

Bibliography

[1] M. Adams, A. Loftus, S. Dunn, M. Joens, and J. Fitzpatrick. Light sheet fluorescence microscopy. *NAH*, 2015.

[2] P. A. Santi. Light sheet fluorescence microscopy. *JHC*, 2011.

[3] S. Alexander et al. Dynamic imaging of cancer growth and invasion: a modified skin-fold chamber model. *Histochem. Cell Biol*, 2008.

[4] N. O. Petersen, P. L. Hoddelius, P. W. Wiseman, O. Seger, and K. E. Magnusson. Quantitation of membrane receptor distributions by image correlation spectroscopy: concept and application. *Biophys. J.*, 1993.

[5] I. Cesana. Characterization of a compact spim microscope for flow mapping in hemodynamics, 2016.

[6] D. Magde, E. Elson, and W. Webb. Thermodynamic fluctuations in a reacting system - measurement by fluorescence correlation spectroscopy. *Physical Review Letters*, 1972.

[7] J. Mertz. *Introduction to Optical Microscopy*. 2009.

[8] M. Jemielita, M. Taormina, A. DeLaurier, C. Kimmel, and R. Parthasarathy. Comparing phototoxicity during the development of a zebrafish craniofacial bone using confocal and light sheet fluorescence microscopy techniques. *Journal of biophotonics*, 2013.

[9] C. W. McCutchen. Generalized aperture and the three-dimensional diffraction image. *OSA 54*, 1964.

[10] D. Wilding, P. Pozzi, O. Soloviev, G. Vdovinand, and M. Verhaegen. Light-sheet optimization for microscopy. *Adaptive Optics and Wavefront Control for Biological Systems II - Conference Paper*, 2016.

[11] W. Singer, M. Totzeck, and H. Gross. *Physical Image Formation*. 2005.

[12] S. Tyo. *Linear Systems and Fourier Optics Lessons*. 2010.

[13] J. D. Gaskill. *Linear systems, Fourier Transform and Optics*. 1978.

[14] R. H. Webb. Confocal optical microscopy. *Rep. Prog. Phys. 59*, 1995.

[15] M. Abramowitz, K. R. Spring1, H. E. Keller, and M. W. Davidson. Basic principles of microscope objectives. *BioTechniques*, 2002.

[16] L. Gao. Optimization of the excitation light sheet in selective plane illumination microscopy. *Biomed Opt Express*, 2015.

[17] P. Pozzi, L. Sironi, L. D,ÄôAlfonso, M. Bouzin, M. Collini, G. Chirico, P. Pallavicini, F. Cotelli, and E. A. Foglia. Electron multiplying charge-coupled device-based fluorescence cross-correlation spectroscopy for blood velocimetry on zebrafish embryos. *JBO*, 2014.

[18] M. Bouzin. *Image Correlation Methods to Follow Dynamic Processes in Biological Systems.* PhD thesis, Unimib, 2015.

[19] M. Bouzin. *Multiphoton Multifocal methods for Neuroscience and Hemodynamics.* PhD thesis, Unimib, 2014.

[20] O. Krichevsky and G. Bonnet. Fluorescence correlation spectroscopy: the technique and its applications. *Rep. Prog. Phys.*, 2002.

[21] J. Cooley and J. Tukey. An algorithm for the machine calculation of complex fourier series. *Math. Comput. 19*, 1965.

[22] H Bruss. *Microfluidics Lectures*. 2006.

[23] M. Ramakrishna. *Elements of Computational Fluid Dynamics*. 2011.

[24] S. O. Isikmana, W. Bisharaa, S. Mavandadia, F. W. Yu, S. Feng, R. Laua, and A. Ozcan. Lens-free optical tomographic microscope with a large imaging volume on a chip. *PNAS*, 2011.

[25] P. Ihalainen, M. Pesonen, P. Sund, T. Viitala, A. Maattanen, J. Sarfraz, C. Wilen, R. Osterbacka, and J. Peltonen. Printed biotin-functionalised polythiophene films as biorecognition layers in the development of paper-based biosensors. *Applied Surface Science*, 2016.

[26] Y. Tan, K. Hettiarachchi, M. Siu, Y. Pan, and A. Phillip Lee. Controlled microfluidic encapsulation of cells, proteins, and microbeads in lipid vesicles. *Jacs Comm.*, 2005.

[27] T. R. Kline, W. F. Paxton, Y. Wang, D. Velegol, T. E. Mallouk, and A. Sen. Catalytic micropumps: Microscopic

convective fluid flow and pattern formation. *Jacs Comm.*, 2005.

[28] T. Fujii. Pdms-based microfluidic devices for biomedical applications. *Applied Surface Science*, 2002.

[29] H. Wu, B. Huang, and R. N. Zare. Construction of microfluidic chips using polydimethylsiloxane for adhesive bonding. *Lab on a Chip*, 2005.

[30] Y. Tan, K. Hettiarachchi, M. Siu, Y. Pan, and A. P. Lee. Controlled microfluidic encapsulation of cells, proteins, and microbeads in lipid vesicles. *Jacs Comm.*, 2005.

[31] I. Budin and N. K. Devaraj. Membrane assembly driven by a biomimetic coupling reaction. *J. Am. Chem. Soc.*, 2013.

[32] G. J. Lieschke and P. D. Currie. Animal models of human disease: zebrafish swim into view. *Nat. Rev.*, 2007.

[33] T. Chico, P. Ingham, and D. Crossman. Modeling cardiovascular disease in the zebrafish. *Trends Cardiovasc. Med.*, 2008.

[34] K. Dooley and L. Zon. Zebrafish: a model system for the study oh human disease. 2000.

[35] J. W. Krieger, A. P. Singh, N. Bag, C. S. Garbe, T. E. Saunders, J. Langowski, and T. Wohland.

[36] L. Gao, L. Shao, B. Chen, and E. Betzig. 3d live fluorescece imaging of cellular dynamics usign bessel beam plane illumination microscopy. *Nature Protocols*, 2014.

[37] M. Duocastella, G. Sancataldo, P. Saggau, P. Ramoino, P. Bianchini, and A. Diaspro.

[38] R. J. Adrian and J. Westerweel. *Particle Image Velocimetry*. 2011.

[39] D. Garcia. A fast all-in-one method for automated post-processing of piv data. *PubMed Central Canada*, 2014.

[40] J. Westerweel. Efficient detection of spurious vectors in particle image velocimetry data. *Experiments in Fluids*, 1994.

[41] P. Hariharan. *Optical Holography 2ed: Principles, Techniques and Applications*. 2008.

[42] D. Donnarumma, A. Brodoline, and D. Gross. 4d holographic microscopy of zebrafish larvae microcirculation. *Optics Express*, 2016.

[43] R. N. Bracewell. *Fourier Transform*. 1999.